UNIVERSITÀ DEGLI STUDI DI CATANIA
DIPARTIMENTO DI FISICA E ASTRONOMIA
XXXI CORSO DI DOTTORATO IN FISICA

GIOVANNA FERRARA

Search for neutrino counterparts of the HAWC point-source sky map using 10 years of ANTARES data and KM3NeT first results

Tutor:
Prof. F. Leone
Dott. ssa R. Coniglione
Dott. S. Biagi

ANNO ACCADEMICO 2018/2019

Contents

Introduction

During the last century young generations of telescopes made possible to study the Universe through new cosmic messengers, extending the energy range of detectable radiation up to very high energy. These observations allowed to discover a large variety of ever observed phenomena, like the emission of very high energy γ-rays by astrophysical sources and the presence of cosmic mechanisms able to accelerate charge particles up to ultra high energy. Despite these discoveries represent breakthrough results in the field of astroparticle physics, many open questions about the high energy Universe remained unsolved, as the nature of the acceleration processes and the astrophysical sources where such mechanisms take place. In order to shed light on acceleration sites and acceleration mechanisms, neutrinos produced by the interaction of charge particles has been identified as excellent cosmic messenger. Being electrically neutral and weakly interacting particles, neutrinos can propagate undisturbed through the Universe without losing information about the acceleration process. Furthermore, since cosmic neutrinos and γ-rays are expected from the decays of hadrons produced in the interactions of cosmic rays with the matter surrounding the acceleration sites, the detection of cosmic neutrinos represents the smoking gun of hadronic process in astrophysical sources and can allow to constraint or discover the cosmic ray sources in the Universe.
Already in 1960 Markov proposed a possible way to detect high energy cosmic neutrinos exploiting huge volumes of transparent natural material, such as ice or sea water. Interacting with matter, high energy neutrinos produce relativistic charged particles that emit Cherenkov photons, which can be detected though arrays of photomultipliers. Above few TeV, the relativistic muons produced in charged current interaction of muon neutrinos can travel several kilometres in the medium, resulting almost collinear with the interacting neutrino. Reconstructing the muon trajectory it is then possible to point-back the astrophysical sources.
However, only in the 2010s the era of neutrino astronomy has began with the observation of a diffuse neutrino signal of cosmic origin [1, 2] by the km^3 scale neutrino telescope IceCube [3] at the South Pole. The further detection of the high energy neutrino event *IceCube-170922A* [4, 5], in coincident with the γ-ray emission of the Blazar TXS 0506+056, allows to shed some light on the possible nature of neutrino sources in the Universe, identify Blazars as potential point sources of high energy neutrinos.
Despite these observations represent milestone results in the field of neutrino astronomy, the astrophysical sources responsible for the origin of the diffuse neutrino signal observed

by IceCube are still unknown. By using up-going muons neutrino, telescopes located in the northern hemisphere can point towards the most powerful galactic gamma ray sources, like the Galactic Plane, playing a crucial role for the investigation about the nature of cosmic neutrino fluxes.
During the last decades a growing interest has been pointed toward the ANTARES (Astronomy with a Neutrino Telescope and Abyss environmental RESearch) telescope [6]. Located in the Mediterranean Sea, ANTARES is the largest and more sensitive neutrino telescope in the norther hemisphere enable to extend the neutrino astronomy in a complementary region of the Universe respect that one accessible by IceCube. Several analyses have been performed by the ANTARES collaboration searching for both point-like and extended neutrino sources and sources of diffuse neutrino fluxes. Even though no cosmic neutrino source has been discovered upper limits have been set, proving the great potential of the ANTARES telescope especially in the southern sky.
In order to extend the ANTARES performances and investigate about the nature of the neutrino flux of cosmic origin detected by IceCube, the KM3NeT (km^3-scale Neutrino Telescope) collaboration started to build a new research infrastructure [7] in the norther hemisphere which will drive towards promising breakthrough both in the field of neutrino astronomy and neutrino physics. The KM3NeT research infrastructure will host two neutrino detectors: the ARCA (Astroparticle Research with Cosmics in the Abyss) telescope, optimised to search for high energy neutrino sources in the Universe, and the ORCA (Oscillation Research with Cosmics in the Abyss) telescope, whose main physics goal is the determination of the neutrino mass hierarchy.
In this work a search for the point-like neutrino sources counterpart of the HAWC [8] γ-ray sky has been performed using 10 years of ANTARES data. The HAWC point-source sky map, used by the HAWC collaboration to develop the 2-years HAWC γ-ray point source catalogue, has been considered as reference model to determine a topological and spectral energy distribution of a neutrino emission all over the sky. The ANTARES capability to detect such neutrino emission has been investigated and the first results are presented.
Finally, the strategy adopted to monitor the quality of ARCA raw data and the monitoring software developed to perform this analysis are described. The first results of the monitoring and qualification of KM3NeT/ARCA data are also presented.
The thesis is organised as follow:

- In chapter 1 the connection between cosmic rays, γ-ray and neutrinos in astrophysical accelerators and the neutrino production mechanisms of interest for the neutrino astronomy are described;

- In chapter 2 the detection principle of high energy astrophysical neutrinos and the main background components for the detection of cosmic neutrinos are explained. Some of the main existing neutrino telescopes are also presented.

- Chapter 3 is dedicated to the description of the key elements of the ANTARES and KMeNeT neutrino telescopes. The main results obtained with almost 10 years of

ANTARES data and the sensitivity studies for the search of cosmic neutrinos with the KM3NeT/ARCA telescope are presented.

- In chapter 4 the simulation codes used to perform the Monte Carlo simulations of the incident neutrinos, their interaction in the medium, light generation and propagation in water, as well as the track and shower reconstruction algorithms used in the ANTARES collaboration are outlined.
- Chapter 5 is dedicated to the description of the procedure used to derive the neutrino counterpart of the HAWC γ-ray sky maps using ANTARES data;
- In chapter 6 the research method used to investigate the ANTARES capability to detect a neutrino counterpart of the HAWC γ-ray sky are described and the results of the search are presented.
- In Chapter 7 the strategy adopted to monitor the quality of ARCA raw data and the monitoring software developed to perform this analysis are described. Then, the first results obtained with the KM3NeT/ARCA data taking qualification procedure are also presented;

Chapter 1

Cosmic Ray, Gamma Ray and Neutrino Astronomy

Since the discovery of Cosmic Rays (CRs) by V. Hess in 1912, the attempt to establish the nature of such a cosmic radiation, coming from above the Earth's atmosphere, has been one of the most demanding scientific activities of the last century. The long and complex history of CRs made cosmic ray studies difficult to identify as a field of research in itself. However, the connection of primary cosmic rays with chemical and isotopic compositions of matter in the Universe, the energy spectra of protons and nuclei, their origin and the mechanisms for their accelerations and propagation in the interstellar medium, led to identify CRs as astronomical objects. At the beginning of the 1950s, the study of the their origin, in parallel with the measurement of CR properties, gave birth to the Cosmic Ray Astronomy and the development of observatories aimed to discover the cosmic ray sources in the Universe. As the same time, the discovery of the existence of particles characterized by energies much higher than could be previously imagined revived the interest for mechanisms able to accelerate cosmic rays at such energies. In 1949 E. Fermi proposed for the first time a model for the acceleration mechanism of CRs [9] able to justify the observed CR energy spectrum, but only in the 1978 A. R. Bell [10] identified the shock front of magnetised plasma as the right astrophysical environment in which the acceleration process can accelerate charged particles up to very high energy.
The efforts done to understand the nature of CRs gave also origin to a strict connection between CRs and particle physics, leading to the birth of the present particle physics. If CRs studies allowed to the discovery of new particles, like the positron in 1932, muons in 1937, pions and strange particles (Λ and K) in 1947 and antimatter, on the other hand nuclear and particle physics provided important input to CR physics, like the measurement of the nuclear spallation cross sections with accelerators, fundamental for understanding the propagation of CRs in our galaxy.
Althrough the development of several cosmic ray observatories, with the purpose to discover the sources of the highest energy particles produced in the Universe and understand their properties, CRs do not allow to point astrophysical sources like photons do in traditional astronomy. Being electrically charged particles, cosmic magnetic fields deflect

CR's paths during their propagation in the Universe preventing CRs to point back their sources. The search for new cosmic messengers, strictly related to CR production and acceleration mechanisms in cosmic ray sources, identified in gamma rays and neutrinos the best probes to scan the high energy Universe. In fact, since the middle of the last century it had already known that the decay of mesons, produced in the hadronic interactions of CRs with matter and radiation inside or near the cosmic ray sources, can produce detectable fluxes of high energy gamma-rays and neutrinos which carry unique information on the ultra relativistic Universe. This connection identify the regions of the Universe where cosmic ray interactions take place as possible sources of very high energy gamma-rays and neutrinos. In 1980s the realization of the firsts gamma-ray telescopes and the further development of neutrino observatories opened the way to the era of the multimessenger study of the Universe. Gamma ray astronomy enabled to extend the range of detectable radiation up to tens of TeV, yielding to the discover of new astrophysical objects in the Universe. However, above several tens of TeV the interactions of gamma rays with extragalactic background photon fields, mainly with infrared and microwave backgrounds, severely restrict the distances over which gamma rays can travel. On many aspects, neutrinos seem to be the suitable messengers for astronomy at the highest energies. Like gamma rays, neutrinos travel undeflected by magnetic fields and, being weakly interacting particles, the small cross-section lets them to propagate undisturbed through the Universe, giving the possibility to point back their sources. Up to now Neutrino Astronomy represents the unique observational approach to achieve a deeper knowledge of the high energy Universe.
Despite great deal of effort done in the field of CR, Gamma Ray and Neutrino Astronomies, many fundamental and unsolved questions are still unanswered about the extremely high energy Universe. In this chapter, aimed to underling the strict connection among CRs, gamma rays and neutrinos in astrophysical environments, at first a brief description of the main characteristics and acceleration mechanism of CRs is presented. Then, the gamma rays emission scenarios in cosmic sources and the status of gamma ray detection are discussed. Finally, the neutrino production mechanisms of interest for neutrino astronomy and the candidate neutrino sources in the Universe are described.

1.1 Cosmic rays and cosmic accelerators

The hadronic nature of the cosmic ray flux gives a clear evidence that astrophysical sources in which hadron acceleration takes place exist. Cosmic Rays are composed mainly of protons ($\sim 85\%$), helium nuclei ($\sim 12\%$) and heavier nuclei ($\sim 1\%$), with a minimal fraction of photons, electrons and low energy neutrinos ($\sim 2\%$).
One of the most distinctive features of cosmic rays is their energy spectra. The measurement of the CRs spectra in different energy ranges shows that the cosmic ray flux extends from a few hundreds MeV up to 10^{20} eV, with a decreasing intensity covering more than 30 orders of magnitude, see Fig. 1.1. Above 10 GeV, the energy spectra can be well represented by a power law energy distribution whose spectral index γ assumes

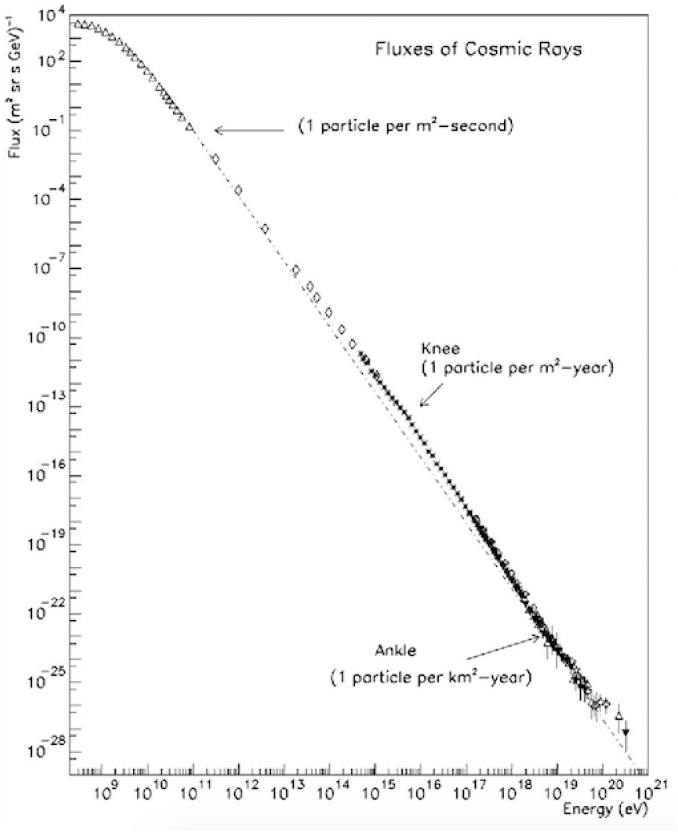

Figure 1.1: Cosmic rays energy spectra: the intensity of cosmic ray flux decreases more than about 30 order of magnitude with the energy [11].

different values in different energy ranges

$$\frac{dN}{dE} \propto E^{-\gamma} \qquad \gamma = \begin{cases} 2.7 & E < 10^{15} \text{ eV} \\ 3 & 5 \cdot 10^{15} \text{ eV} < E < 10^{18} \text{ eV} \\ 2.7 & E > 10^{18} \text{ eV} \end{cases} \tag{1.1}$$

The change of the power law spectral index allows to identify two characteristic features in the cosmic ray spectra at $E \simeq 10^{15}$ eV and $E \simeq 5{\cdot}10^{18}$ eV, named *Knee* and *Ankle* [12] respectively, which divide the spectra in 3 different energy regions:

- the first region is characterised by $E < 10^{15}$ eV, where the cosmic ray flux is of the order of 1 particle/m^2 per sec and the spectral index is about 2.7. For energies lower than about 100 GeV the intensity of primary cosmic rays flux is high enough to be measured directly with instruments on board of balloons and satellites. Even if the sources of cosmic rays are not yet identified, cosmic rays with energy lower than 10^{15} eV can be attributed to protons accelerated by Supernovae Remnants (SNR) or X-Rays Binary Systems.

- the second region is in the energy range between 10^{15} eV $< E < 10^{18}$ eV, where the cosmic rays flux is of the order of 1 particle/m^2 per year. Due to the low intensity of cosmic ray flux in this energy region, the measurement of the cosmic ray flux is done through ground-based detector of large area on the Earth's surface with long exposure time. They detect the atmospheric cascades of secondary particles produced by the interactions of cosmic rays with the particles in the Earth's atmosphere. In this energy region the composition of cosmic rays tends to be dominated by a heavier nuclei component. An explanation to this trend could rely on the value of the particle gyroradius. A particle of energy E and charge Ze has a gyroradius or *Larmor radius* equal to

$$R = \frac{E}{ZeB\beta c} \tag{1.2}$$

  where $\beta = v/c$ is the particle velocity and B is the galactic magnetic field ($\sim 3\mu G$). Therefore particles are confined in the Galaxy if their Larmor radius is smaller than the Galaxy size. At higher energies the gyroradius of protons increases and they are not confined in the Galaxy, justifying the decrease of the cosmic rays flux and a much heavier nuclei composition. The change in chemical composition and spectral index lead to consider the second energy region of cosmic rays spectra as a transition region from a galactic to an extragalactic origin of cosmic rays [13].

- due to the extremely low cosmic ray flux above $5{\cdot}10^{18}$ eV, the third energy region is the most challenging for the observation of cosmic rays. At these energies the cosmic ray flux changes again spectral index, from 3 to 2.7, and the flux composition is probably proton-dominated [13, 14]. The hardening of the cosmic ray spectra may be attributed to an increase of the extragalactic component of cosmic ray. Since galactic sources seem to not being able to accelerate particles to higher energies, the detection of protons with $E > 10^{19}$ eV indicates the existence of extragalactic sources in which the acceleration mechanism takes place. The understanding of the ultra high energy cosmic rays (UHECR) origin is still an open question in the field of astroparticle physics. The candidates sources in the Universe able to accelerate protons up to 10^{20} eV are the Gamma Ray Bursts (GRBs) and Active Galactic Nuclei (AGNs). Ultra high energy CRs represent also the most suitable way to verify the validation of particle physics principles at ultra high energies and to obtain observational evidences of physics beyond the Standard Model.
  In 1966 K. Greisen, G. Zatsepin and V. Kuzmin predicted a suppression of the UHECR spectrum at about 6×10^{19} eV [15]. This effect is known as the *GZK cutoff* and it should be due to the interaction of UHE cosmic ray protons with photons of the cosmic microwave background radiation (CMBR). The energy threshold value of this effect is set by the mass and width of the Δ resonance and by the temperature of the CMBR. Since the exposure time of the current generation of cosmic ray observatory, represented by the Pierre AUGER Observatory [16], is too small to measure the flux of cosmic rays at the cutoff energy, no event above 10^{20} eV has been measured up to now raising questions about the validity of GZK prediction.

1.1.1 Particle acceleration in the Universe

The nature of the mechanism through which charge particles are accelerated up to ultra-relativistic energy, earning a power law energy spectra, is one of the most fascinating but still unknown aspect of high energy astrophysics. The most accepted mechanism for cosmic rays acceleration, able to justify the observational evidence of CR spectrum, is the "Fermi acceleration mechanism" proposed by E. Fermi in 1949. Fermi proposed the first theoretical estimation of this mechanism, describing it as a stochastic mechanism through which particles are accelerated and, if the particles remain within the acceleration regions for enough time, a power law energy spectra is provided.
In the first version of the acceleration mechanism, Fermi describes the energy gain of charged particles through the elastic collision between particles, moving at the speed of light $v \simeq c$, in a molecular cloud, with $V \ll c$, as depicted in Fig. 1.2. In the laboratory frame the charge particles get inside the molecular clouds with a generic collision angle θ_1 ($0 < \theta_1 < \pi$) and energy E_1. After n collisions, which randomize the particle direction, particles escape from the acceleration region with an angle θ_2 and $E_2 > E_1$.

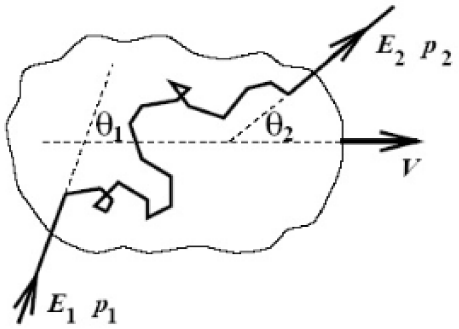

Figure 1.2: Sketch of the collision between a charged particle moving at $v \simeq c$ and a molecular clouds with $V \ll c$. The arrival direction of a charge particle is given by the angle θ_1, after n collisions the particle direction is randomized and it escapes with an angle θ_2.

The relevance of the Fermi process relays on the description of the energy gain of the particle before and after the elastic collision by means the Lorentz transformations between the rest frame (of the particle and the molecular cloud) and the laboratory frame. The average energy gain of the particle per collision become

$$\left\langle \frac{\Delta E}{E} \right\rangle = \frac{4}{3}\beta^2 \tag{1.3}$$

Even if this description allows to obtain a power law energy spectra of the accelerated particles, it does not allow to reach the suited energy gain able to justify the observation of the very high energy cosmic rays detected at the Earth. In this process the energy gain is proportional to the second order of the ratio V/c and for this reason it is knows as the *Second order Fermi acceleration mechanism.*

For a fulfilling description of charge acceleration process in astrophysical environment it has been necessary to wait until the 1978, with the description proposed by A. R. Bell [10]. If Fermi identified the stochastic collision as the main mechanism through which charge particles gain energy, Bell identified the astrophysical shocks as the best sites where the Fermi mechanism can takes place leading to the correct energy gain.
If in shocks, propagating through a medium with a velocity greater than the speed of sound in that medium, there is a mechanism which randomizes the particles directions, particles can gain energy in crossing the shock. A fraction of these particles can re-cross the shock front gaining energy and randomizing their velocity again. Since the shock propagates with a velocity greater than the speed of sound in the medium, it can capture the particles and the process can be repeated several times.
In this process, if N_0 is the number of particles with energy E_0 in the acceleration region and β is the fraction of gained energy for each collision, $E = \beta E_0$ is the average energy of the particle after one collision with the shock front. If P is the probability that the particle remains within the accelerating region, after k collisions there will be $N = N_0 P^k$ particles with energy $E = E_0 \beta^k$ [17]. In order to derive a power law energy spectra of accelerated particles, it is possible to remove the k dependence from the previous quantities considering the ratio

$$\frac{\ln(N/N_0)}{\ln(E/E_0)} = \frac{\ln P}{\ln \beta} \tag{1.4}$$

then

$$\frac{N}{N_0} = \left(\frac{E}{E_0}\right)^{\ln P/\ln \beta} \tag{1.5}$$

obtaining

$$N(E)dE = cost \times E^{-1+(\ln P/\ln \beta)} dE \tag{1.6}$$

From these simple consideration a power law energy spectra is obtained. According to the Bell description, the expressions for β and for the probability P are derived considering the interactions between a strong shock caused, for example, by a supernova explosion propagating through the interstellar medium and a flux of high energy particles presents both in front of and behind the shock front. In such a contest the shock wave moves at a supersonic velocity $U \gg c_s$, with c_s the sound speed in the medium. Considering the high energy particles ahead of the shock, scattering ensures that the particles distribution is isotropic in the frame of reference in which the gas is at rest. The shock advances through the medium at velocity U but the gas behind the shock travels at a velocity $(3/4)U$ relative to the upstream gas. When a high energy particle crosses the shock front, it obtains a small increase in energy, of the order $\Delta E/E \sim U/c$. The same thing occurs if the opposite process it is considered. Evaluating the average increase

in energy of the particle when it crosses the shock front, overall the arrival directions $0 < \theta_1 < \pi/2$, and coming back it is possible to obtain β

$$\beta = \frac{E}{E_0} = 1 + \frac{4}{3}\frac{V}{c} \tag{1.7}$$

To find out the escape probability P the classical kinetic theory can be used and the fraction of particles lost per unit time is U/c. Thus $P = 1-(U/c)$, $\ln P = \ln(1-U/c) = -U/c$, $\ln \beta = \ln(1 + 4V/3c) = 4V/3c = U/c$, hence

$$\frac{\ln P}{\ln \beta} = -1 \tag{1.8}$$

and the differential energy spectra of accelerated particles is

$$N(E)dE \propto E^{-2}dE \tag{1.9}$$

The obtained differential energy spectrum is considered the energy spectra of accelerated particles at source. A further contribution to the cosmic ray spectra must be considered due to the propagation and diffusion of cosmic rays in our Galaxy. It leads to a energy spectra with a steeper spectral index, about $\gamma = 2.7$, which justify the differential energy spectra detected at Earth. In astrophysical shocks the presence of strong magnetic fields, with the strength lines tangled with the shocks itself, force charge particles to be trapped in the acceleration region and cross the shocks several times until they gain enough energy to escape from the acceleration region.
Since its development, this mechanism, known as *First order Fermi acceleration mechanism*, exerted great interest. The existence of strong shock in most astrophysical sources is possible, like in Supernovae Remnants and Active Galactic Nuclei, making them reasonable sources of high energy accelerated particles.

1.1.2 Hillas Plot

A general estimate of the highest energy value that can be reached by a charge particle in astrophysical environment can be obtained using the *Hillas Rule* formulated by A. M. Hillas [18] in 1984. Particles with charge Z which moves in an acceleration region of size L and make irregular loops in a magnetic field of strength B have a gradual acceleration gaining energy. The highest energy values are strictly related to the physical and geometrical parameters that characterise the acceleration region, as expressed by the following formula

$$E_{max} \sim \beta_{shock} \cdot Z \cdot B[\mu G] \cdot L[kpc] \cdot 10^{18} \text{ eV} \tag{1.10}$$

This result represents the Hillas limit and it is summarized in the well-know Hillas

plot, where various astrophysical objects are plotted on a B, L plane as shown in Fig. 1.3. According to this empirical rule, charged particles accelerated by SNRs, in which $B \sim 10^{-4}$ $[G]$ and L is of the order of few parsecs, can gain energy up to the energy of the $Knee$, supporting the idea that cosmic rays with $E < 10^{15}$ eV have a Galactic origin. The acceleration of charged particles up to $E_{max} \sim 10^{18-19}$ eV, the so called UHECRs, implies larger cosmic objects with strong magnetic field. The best candidate as UHECR sources are the AGNs. The extragalactic nature of these astrophysical sources highlights the possibility that CRs are accelerated up to ultra high energies outside our Galaxy.

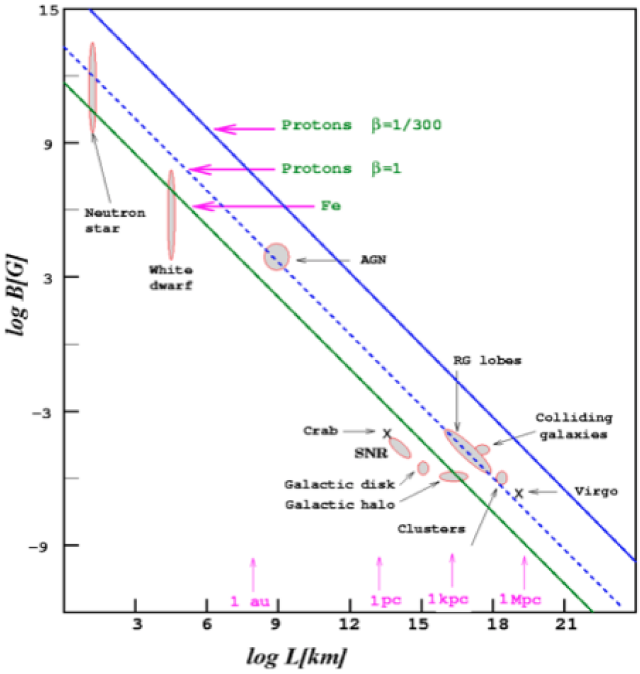

Figure 1.3: Size and magnetic field strength of possible site of particle acceleration [18]. Astrophysical objects below the green line cannot accelerate protons up to 10^{20} eV.

1.2 The Gamma Ray astronomy

Gamma-ray astronomy concerns the study of astrophysical sources using the most energetic part of the electromagnetic spectra, the γ-rays, through which it is possible to observe the Universe in the energy range above ~ 30 GeV. The importance of γ-ray astronomy relies mainly on the strict connection with the study and observation of cosmic rays. In fact, even if γ-rays are produced by a large variety of energetic astrophysical phenomena, γ-ray emission is also the signature of cosmic ray interactions with gas and photons both near the acceleration sites and during their propagation in the Universe. Despite the connection with cosmic ray studies, the development of gamma-ray astron-

omy made also possible to get a deeper understanding of the sources of non-thermal emission in the Universe, allowing to extend the observational window through which to look at these sources and complete their multi-wavelength detection. In fact, several astrophysical objects show a flux density distribution as a function of the energy, the so called Spectral Energy Distribution (SED), which covers all the electromagnetic spectrum from the radio frequency up to the γ-rays, with a characteristic two peaks distribution like in the case of BL Lac objects (see Fig. 1.4) [19]. The low energy component of the SED is mostly due to the synchrotron radiation of electrons at radio wavelength, but the high energy γ-ray emission can come from many physical processes involving both neutral and charged particles, giving rise to two possible scenarios, the so called leptonic and hadronic models. In leptonic models the electromagnetic emission derives

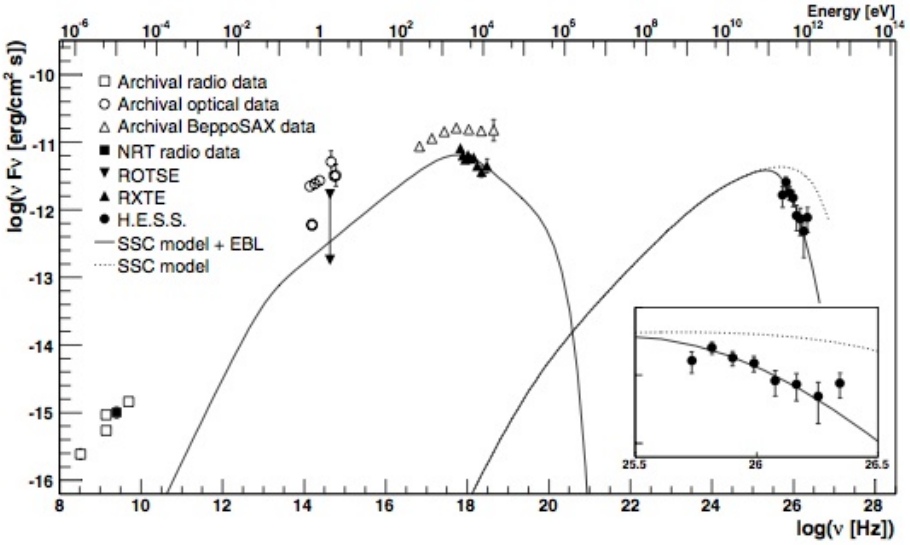

Figure 1.4: Spectral energy distribution of the BL Lac object H 2356-309. Data from NRT, ROTSE-III and RXTE are simultaneous to the HESS observations and shown as filled symbols. The dashed line shows the synchrotron self-Compton (SSC) model without absorption. The inlaid box shows a zoom in the VHE regime [20].

from pure electromagnetic processes, while in the hadronic scenario the decay chain of mesons leads to the emission of high energy gamma rays and neutrinos. Hence, the detection of gamma rays emitted by astrophysical sources makes impossible to distinguish between the leptonic or hadronic nature of the gamma ray emission, but the detection of cosmic neutrinos from the same sources represents a clear evidence of the hadronic origin of such process.

If the detection of cosmic neutrinos allows to verify the existence of hadronic acceleration process in astrophysical sources, it does not exclude the possibility of a leptonic contribution to the gamma ray emission.

1.2.1 The leptonic model

In leptonic models the high energy spectra of astrophysical objects is assumed to be dominated by leptons (electrons and possibly positrons), while protons are not accelerated to sufficiently high energies to contribute significantly to the radiative emission. Synchrotron emission, due to electrons moving in a magnetic field, generates photons with an energy spectrum peaked in the infrared/X-ray range and it constitutes the target for the electron population presents in the same region. If synchrotron photons gain energy through collisions with high-energy electrons in the inverse Compton scattering, the process is called Self-Synchrotron Compton (SSC) mechanism and it can explain the emission of high-energy γ-rays. This process occurs in regions where accelerated electrons and high energy density of soft-photons coexist. Due to collisions, photons increase their energy at the expenses of the kinetic energy of the electrons, with a consequent emission from infrared/X-ray up to GeV-TeV energies. Hence a leptonic scenario prohibits neutrino production in astrophysical sources.

1.2.2 The hadronic model

In astrophysical environments the presence of π^0 is the signature of the existence of accelerated hadrons interacting with the surrounding material or radiation fields via the

$$pp \rightarrow \ \pi^0, \pi^{\pm}, \pi^0, K^{\pm}, K^0, p, n,$$

or

$$p\gamma \rightarrow \Delta^+ \rightarrow \begin{cases} p\pi^0 \\ n\pi^+ \end{cases}$$

interactions, in which almost the same number of π^0 and $\pi^{\pm}$ are produced and whose subsequent decay leads to the emission of high energy neutrinos and γ-rays

$$\begin{aligned} &\pi^+ \rightarrow \mu^+ + \nu_\mu \rightarrow e^+ + \nu_e + \nu_\mu + \bar{\nu}_\mu \\ &\pi^- \rightarrow \mu^- + \bar{\nu}_\mu \rightarrow e^- + \bar{\nu}_e + \nu_\mu + \bar{\nu}_\mu \\ &\pi^0 \rightarrow \gamma + \gamma \end{aligned}$$

In this process the π^0 decays immediately in two γ-rays, while the charged pions decay in $\pi^- \rightarrow \mu^- \ \bar{\nu}_\mu$ followed by the muon decay $\mu^- \rightarrow e^- \ \bar{\nu}_e \ \nu_\mu$ (and the charge-conjugate reaction for the π^+). Therefore in this scenario the hadronic nature of γ-ray emission can be identified by the detection of neutrinos produced in meson's decay.
At GeV energies a typical spectral feature, called *pion-decay bump*, uniquely identifies the presence of γ-rays originated by π^0 decay, giving clear proof that the source accelerates protons. The presence of the pion-decay bump implies that in case of hadronic process the expected photon spectra in the GeV energy range, that is proportional to that of interacting particles $E^{-\Gamma}$, is steeper than the $E^{-(\Gamma+1)/2}$ in the case of leptonic process. The identification of pion-decay may be really difficult because high-energy electrons can also produce a further gamma rays emission via bremsstrahlung and Inverse Compton

(IC) scattering. The presence of the characteristic pion-decay feature in the gamma-ray spectra of two SNRs [21], IC 443 and W44, has been observed with the Fermi Large Area Telescope. Since the measured gamma-ray spectra, in particular the low-energy parts, matches the π^0 decay model (see Fig. 1.5), this detection provides direct evidence that cosmic-ray protons are accelerated in SNRs.

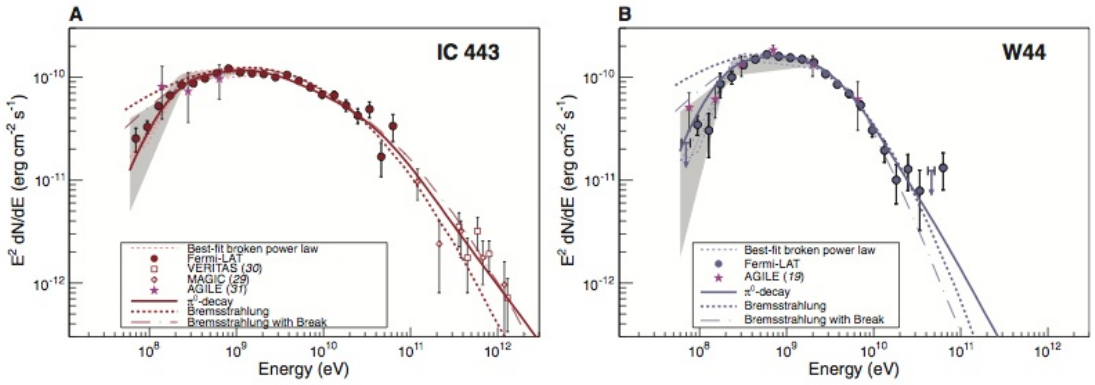

Figure 1.5: Gamma-ray spectra of IC 443 (A) and W44 (B) [21] SNRs as measured with the Fermi LAT. Color-shaded areas bound by dashed lines denote the best-fit broadband smooth broken power law (60 MeV to 2 GeV); gray-shaded bands show systematic errors below 2 GeV due mainly to imperfect modeling of the galactic diffuse emission. At the high-energy end, TeV spectral data points for IC 443 from MAGIC and VERITAS are shown. Solid lines denote the best-fit pion-decay gamma-ray spectra, dashed lines denote the best-fit bremsstrahlung spectra, and dash-dotted lines denote the best-fit bremsstrahlung spectra when including an ad hoc low-energy break at 300 MeV c^{-1} in the electron spectra. These fits were done to the Fermi LAT data alone (not taking the TeV data points into account).

1.3 Detection of high energy γ rays

The multimessenger approach typical of high energy astroparticle physics exploits both charge and neutral particles as cosmic messengers to study the very high energy Universe. The detection of such cosmic radiations takes advantage of the nature of the interaction processes in which cosmic messengers are involved, using detection techniques typical of experimental particle physics.
Due to the decrease of the gamma ray flux at highest energies, the detection of high energy photons is done through different detection techniques according to the energy range in which photons are observed. Usually it is possible to distinguish tree main energy ranges:

- for energies below 30 GeV photons are named *High Energy Gamma Rays* (HEGRs) and, due to the high intensity of the flux, their detection is done trough experiments on board of satellites which allow for the direct measurement of primary gamma ray flux;
- in the energy range between 30 GeV and 30 TeV gamma rays are classified as Very High Energy Gamma Rays (VHEGRs). The detection of VHE γ-rays is limited

due to their low rate and makes impossible their detection with experiments on satellites. Since the Earth's atmosphere is not transparent to high-energy photons, incident γ-photon scatters on atmospheric nucleus resulting in a pair-production, which emits secondary photons via bremsstrahlung. Such photons produce in turn a e^+e^- pair and so on, giving rise to Extensive Air Showers (EAS) of charged particles and photons, as sketched in Fig. 1.6. Therefore, in this energy range Air Cherenkov Telescopes (IACT) are used to detect VHE γ-rays through the detection of the Cherenkov light emitted by secondary relativistic particles produced during the AES development in atmosphere;

- Above 30 TeV cosmic photons are called Ultra High Energy Gamma Rays (UHEGRs). Even through atmosphere shields the Earth from VHE γ-rays, a large number of induced showers may reach the Earth's surface and be detected by ground-based detectors.

The only way to detect primary γ-rays is using detectors placed on satellites out of the atmosphere. The detection of VHE and UHE γ-rays is done through an indirect technique based on the detection of secondary particle produced by the development of electromagnetic shower in atmosphere.

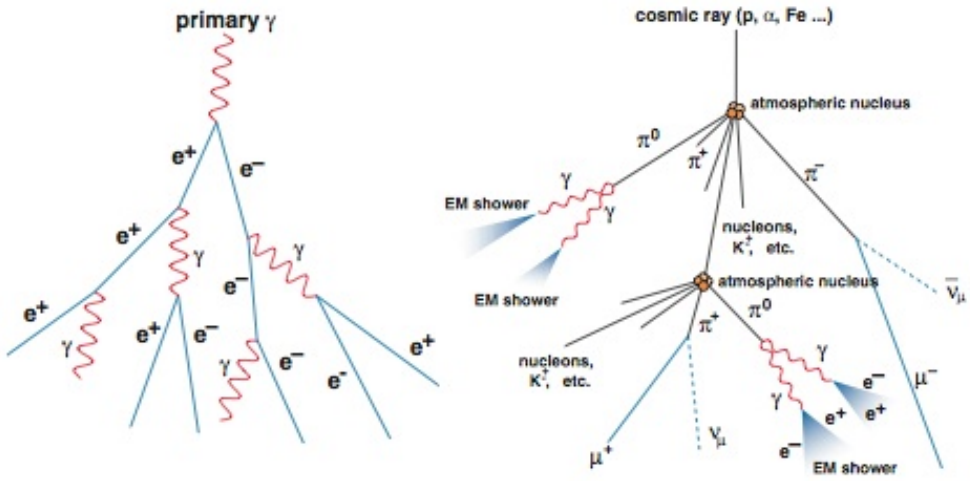

Figure 1.6: Electromagnetic and hadronic shower development in Earth's atmosphere induced by a γ-ray and cosmic ray interaction respectively [22].

The most high-performance γ-rays telescopes on board satellites is the Large Area Telescope (LAT), an imaging high-energy γ-ray telescope covering the energy range from about 20 MeV up to more than 300 GeV on the Fermi Gamma Ray Space Telescope spacecraft. The LAT's field of view covers about 20% of the sky at any time, and it scans continuously the whole sky every three hours. The Fermi-LAT has been surveying the sky since August 2008. Currently 3 main catalogues of sources detected above 10 GeV have been published by Fermi-LaT, with the Third Catalogue of Hard Fermi-

LAT Sources (3FHL) [23] containing 1556 objects detected in the 10 GeV-2 TeV energy range.
Among the most important "first generation" of ground-based telescopes there are: MILAGRO [24], a water Cherenkov radiation telescope situated in New Mexico that stopped taking data in April 2008 after seven years of operation, and ARGO-YJB [25], a extensive air shower detector with Resistive Plate Counters placed in Tibet, taking data from November 2007 to January 2013. The current generation of ground-based telescope is represented by the High Altitude Water Cherenkov Experiment (HAWC) [26] in Mexico and by the future Large High Altitude Air Shower Observatory (LHAASO) [27], whose construction is planned in China.
Whereas, the current generation of IACT telescopes is represented by H.E.S.S. [28], situated in Namibia, MAGIC [29], in La Palma, and VERITAS [30], located in southern Arizona. In the recent years these ground-based telescopes have greatly contributed to the survey of the TeV gamma-ray sky and the discovery of more than 100 TeV sources.

1.4 High energy neutrino astronomy

The existence of the neutrino was postulated for the first time by W. Pauli in 1930 to explain how beta decay could conserve energy, momentum, and angular momentum [31]. A fundamental contribution to the development of the idea that a new particle exists was made by E. Fermi in 1934, who built the first theory of the β-decay of nuclei. The theory was based on the Pauli assumption that in the β-decay a neutral light particle of spin $1/2$ was emitted together with the electron. Fermi proposed to call this particle *neutrino*. In 1942 W. Ganchang first proposed the use of beta capture to experimentally detect neutrinos but only in 1956 C. Cowan and F. Reines confirmed the existence of the antineutrino, the antiparticle of neutrino.
An important challenge in the field of neutrino physics involved the late 1960s, when several experiments found that the number of neutrinos arriving from the Sun was between one third and one half the number predicted by the Solar Standard Model [32]. This discrepancy, which became known as the "solar neutrino problem", remained unsolved for about thirty years until the discovery of neutrino oscillations and a new understanding of neutrino physics. In the Standard Model of particles, for the lepton number conservation, neutrinos are associated with charge leptons leading to the existence of neutrino of three flavors, ν_μ, ν_e, ν_τ. Generally neutrinos are produced in a specific eigenstate of flavor but they can be detected in another one because they can oscillate among the flavors during their propagation through the space. The discovery of neutrino oscillations allowed to explain the lack of neutrinos detected from the Sun. In fact, the use of a specific detection channel for neutrino detection prevented the possibility to reveal all neutrino flavors, making experiments sensitive only to one neutrino flavor.
Neutrino oscillations imply that neutrinos have mass. No direct measurement of any neutrino mass has been made yet but direct limits have been set, defining neutrinos mass many orders of magnitude smaller than masses of charged leptons and quarks. Neutrinos

are the only fundamental fermions which have no electric charge and they can take part only in weak interactions mediated by W and Z bosons.
The main reason of the search for cosmological high-energy neutrinos relies on the fact that the detection of astrophysical neutrinos allows to discover the sources of ultra-high energy cosmic rays in the Universe. In the last decades the development of neutrino telescopes through with look at high energy sky, such as IceCube and ANTARES, opened the way to the neutrino astronomy. This new branch of astroparticle physics allowed to extend the multimessanger observation of cosmic rays sources in the Universe, making possible to verify the existence of hadronic processes in astrophysical objects.
Different processes can lead to neutrino production in astrophysical sources. In general the interaction and decay of hadrons produces, at some point of the decay chain, charged pions that decay into high energy muons and muon neutrinos:

$$\text{hadrons} \rightarrow \pi^+ \rightarrow \mu^+ + \nu_\mu \rightarrow e^+ + \nu_\mu + \bar{\nu}_\mu + \nu_e$$
$$\text{hadrons} \rightarrow \pi^- \rightarrow \mu^- + \bar{\nu}_\mu \rightarrow e^- + \nu_\mu + \bar{\nu}_\mu + \bar{\nu}_e$$

Only the interaction and decay of hadrons can produce muon neutrinos, suggesting to look at this process as the main neutrino production mechanism for neutrino astronomy. The hadronic nature of this process gives hints that astrophysical sources in which hadrons are accelerated up to high energies can be considered the best candidate sources of cosmic neutrinos in the Universe.

1.4.1 Neutrinos from astrophysical accelerators

The most likely scenario for cosmic neutrino production is the so called "astrophysical beam dump", a contest in which accelerated particles interact with matter near the source producing secondary particles. Astrophysical beam dump is similar to a beam dump at a terrestrial accelerator but, in the first case, secondary neutrinos and photons are emitted identifing such astrophysical environments as high energy accelerator. Since some of the candidate cosmic ray sources in the Universe are associated with relatively dense concentration of matter, cosmic ray sources represents the best place in the Universe in which astrophysical beam dump can produce cosmic neutrinos.
Hadron interactions lead also to the emission of neutral pions π^0, which further decay produces high energy photons. For each charged meson's decay three neutrinos are produced, with the ratio $\nu_e : \nu_\mu : \nu_\tau = 1 : 2 : 0$, but due to neutrino oscillations a flavor equipartition is expected at the Earth, $\nu_e : \nu_\mu : \nu_\tau = 1 : 1 : 1$. At high energies, about 20% of the proton energy is transferred to the pion and it is statistically equally distributed among the chain decay products, therefore each neutrino carries $\sim 5\%$ of the interacting proton energy. In Fig. 1.7 the measured and expected neutrino fluxes emitted by different astrophysical sources are reported. The atmospheric neutrino flux, due to the interaction of CRs with the atmosphere, is dominant up to energies of TeV and represents an important component of background for the detection of cosmic neutrino fluxes emitted by GRBs and AGNs.

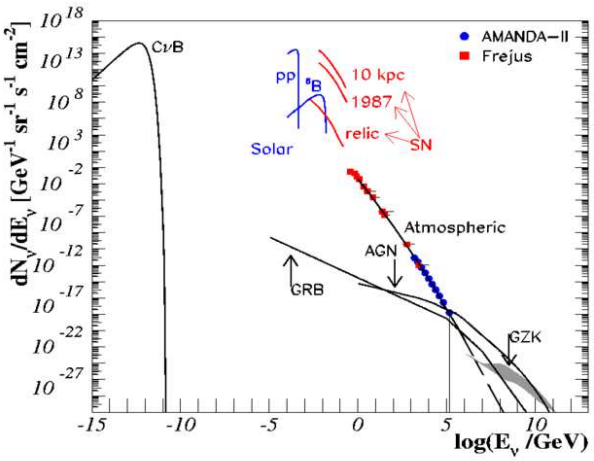

Figure 1.7: The astrophysical neutrino spectra including different source predictions [33]. The fluxes based on predictions are shown as dashed lines. The solid lines represent those fluxes already measured. Point source fluxes are scaled by $1/(4\pi)$ factor to be comparable to diffuse spectra.

Therefore, due to the γ-rays and neutrinos connection in hadronic processes, by identifying the brightest gamma-ray sources it could be possible to identify the most likely neutrino point sources in the Universe.

1.5 Candidate sources of cosmic neutrinos

The IceCube's discovery of neutrino events of cosmic origin in the TeV-PeV energy range stated the beginning of the age of neutrino astronomy. The observational evidence that the composition of cosmic rays spectra between 10^{15} eV and 10^{18} eV [34] tends to be dominated by a heavier nuclei component strengthens the hypothesis of an extragalactic origin of very high energy comic rays. At such energies, also astrophysical neutrinos must be originated by cosmic-ray interactions in extragalactic sources and their detection allows to constrain the sources of very high-energy cosmic rays. Since galactic cosmic ray sources as SNRs, Pulsar Wind Nabulae and Micro Quasars are probably the main sources of high energy cosmic rays, they are also considered the best candidates of high energy cosmic neutrinos. The extragalactic AGNs, like Blazars, and GRBs, the only astrophysical objects able to accelerate cosmic rays up to very high and ultra high energies, are the most suitable sources identified as sources of ultra high energy neutrinos.

1.5.1 Galactic Sources

The galactic sources of cosmic neutrinos are responsible for neutrino production in the GeV-TeV energy range. Among the main galactic neutrino sources there are SNRs, Pulsar wind Nabulae and Micro Quasars.

Super Novae Remnants

A Supernova Remnant (SNR) is the result of a massive star core collapse into a supenova at the end of its life. In fact, a star spends its time in the main sequence balancing its gravitational attraction and the thermodynamic pressure due to the fusion of hydrogen in its core. When the hydrogen decreases significantly inside the core, the fusion region slowly moves outwards and thermodynamic parameters change in such a way that helium fusion starts in the core. Once helium decreases in the center and the helium burning region moves outwards, the star could start an onion-like state with subsequent shells of burning H, He, C, O and Si and an iron core. When iron is completely produced no further fusion process is possible. Depending on its mass, the final state of a supernova can create a neutron star, a pulsar or even a black hole.
The SNR is made of a shell of hot gases ejected into the interstellar medium (ISM) by the supernova explosion, expanding its shell for thousands years. The explosion produces a large flux of low energy neutrinos but the shock front of expanding shell is considered the source of high energy neutrinos. The shell is essentially a magnetized plasma that, if the ambient is dense enough, can store and accelerate hadrons performing the role of a beam dump for a fraction of accelerated hadrons. In this way, high energy neutrinos could be produced.
Different studies on the sensitivity of KM3NeT/ARCA [7] neutrino telescope to the expected neutrino flux emitted by these two SNRs have been performed and the expected neutrino event rates have been estimated through Monte Carlo simulation [35], using the assumption that the γ-ray and the muon neutrino fluxes are related.

Pulsar wind Nabulae

A Pulsar Wind Nebulae (PWN) is a nebula powered by the wind of a pulsar generated by the final state of a Supernova. A Pulsar is a rapidly rotating neutron star rising from the rest of the supernova explosion, while the pulsar wind is the stream of charged particles accelerated to relativistic speed by the strong magnetic field of the spinning pulsar. The pulsar wind streams into the interstellar medium, creating a shock wave where additional particle acceleration can take place. Even if PWNs are generally treated as leptonic sources, some authors explain the TeV γ-ray emission in terms of hadronic interaction [36].

X-ray Binaries and Microquasars

X-ray binary is a class of binary stars that emit X-rays radiation. The X-rays are produced by matter falling from one component, called the *donor* (usually a normal star),

to the other component, called the *accretor*, which can be a compact object like a white dwarf, neutron star or black hole. The compact object emits the energy gained in form of X-rays. X-ray binaries are further subdivided into several subclasses. Among these of particular interest are the microquasars (or radio emitting X-ray binary). Microquasars are characterized by strong and variable radio emission, often associated with structures like radio jets and accretion disk surrounding a compact object which can be either a black hole or a neutron star. The radio and optical emission come from relativistic jets whereas X-ray emission seems to be related to the accretion disk. Upper limits on the E^{-2} muon neutrino flux emitted by various microquasars have been fixed by the IceCube [37] and the ANTARES collaborations [38].

1.5.2 Extragalactic Sources

The brightest extragalactic sources AGNs and GRBs are among the astrophysical objects able to accelerate hadrons up to ultra high energy and, therefore, they are considered the main sources of neutrinos in the TeV-PeV energy range. The study of such sources, through the observation of gamma rays with E > 30 TeV, is limited due to the interaction of high energy photons with the extragalactic background photon field. Since neutrinos do not interact with background radiations, they represent the only cosmic messenger through which look at these sources located at cosmological distances.

Active Galactic Nuclei

In general the term Active Galactic Nuclei (AGN) is used to indicate the existence of energetic phenomena in the central region of galaxies which cannot be attributed directly to stars. AGNs are the brightest persistent objects in the Universe, with a luminosity between $10^{44}-10^{48}$ erg/s, in which a supermassive black hole of $10^6-10^{10}M_\odot$ is accreting matter at high rate. A fraction of gravitational energy of accreted matter is converted in γ radiation, making AGNs the best candidates of CRs and neutrino sources.
Besides the black hole, AGNs are characterized by of an accretion disk of matter, extending perpendicularly to the rotation axis of the galaxy, an obscure torus of dust and gas outside the disc and two relativistic jets with matter outflowing along the rotation axis. Several models predict hadron acceleration in AGN jets. The structure of relativistic jets, where consecutive shock fronts are present, represents the perfect environment in which charged particles can be accelerated via the Fermi mechanism. The high density characterising the inner region of the galaxy identifies also AGN core as hadronic scenarios where the Fermi mechanism can accelerate CRs. Early models [39, 40] postulating the hadronic acceleration in the AGN cores, predicted a production of secondary neutrinos well above the Waxmann and Bachall upper bound [41], and the prediction from some of these models has been experimentally disproved by AMANDA [42].
The AGN emission covers almost the entire electromagnetic spectrum and principally consists of two contributions: a thermal component, the so-called *blue bump* with the maximum at optical-UV frequencies [43], and a non-thermal one extending more than 20 orders of magnitude in frequency. The low energy component of the non-thermal

emission in the radio and soft X-ray regime is assumed due to synchrotron radiation of electrons gyrating in a magnetic field and it is mostly originate in relativistic jets. The origin of the high-energy component can be explained by hadronic or leptonic models and it is highly variable on a wide range of time scales, from less than one hour to months. The hadronic nature of high energy emission from AGNs implies neutrino production at source.
Depending on the observation angle AGNs show a different morphology of the host galaxy and luminosity. AGNs are classified according to an unified model [44], ranging from blazars, if the jet is directly pointed towards the observer, to radio galaxies, including quasar, Seyfert galaxies, BL Lacs. In particular, blazars represent the best neutrino point sources since the jet, where a significant flux enhancement is achieved through Doppler broadening, points towards the Earth.
The recent detection by the IceCube neutrino telescope [4] of a neutrino event in time and space correlation with a γ-ray flare of the TXS 0506+056 Blazar and the measurement of an excess of high energy neutrino events, with respect to the atmospheric background, at the same position between the September 2014 and March 2015, suggests to identify Blazars as sources of very high energy cosmic neutrinos.

Gamma Ray Burst

Gamma-ray bursts (GRBs) are sources of gamma rays associated with extremely energetic explosions observed in distant galaxies. A GRB releases in few seconds an amount of energy almost equal to that emitted by an AGN, with a luminosity $L \sim 10^{51}$ erg/s, characterising such transient phenomena as one of the most violent observed in the Universe.
Despite the large number of detected GRBs, thanks to which the emission features have been studied in details, the nature of these objects is still unknown. A first classification distinguishes "long" from "short" GRBs depending if the duration of the burst is longer or shorter than 2 seconds. The different duration of the burst seems associated with different progenitors: long GRBs are well explained by the core collapse of a massive star, while compact merger of neutron star-neutron star or black hole-neutron star is the proposed scenario for short burst.
The most widely accepted model that describes GRB is the *fireball model* [45]. This model does not give any constraint on the progenitor of the burst but it is a phenomenological description of the actual burst observations. The basic idea is that a large amount of mass is ejected in a short time interval by a central engine, and the plasma is ejected successively in shells. When the outer shells slow down overlapping with inner shells a shock front is built up, named internal shocks, accelerating particles in the plasma up to high energies. Protons can be accelerated up to energies of 10^{21} eV, instead electrons lose their energy through synchrotron radiation, escaping from the shocks as soon as the region becomes optically thin. This component is called *prompt emission* of the GRBs and it is linked with low energy neutrino production. The external shock results from collisions of the shells with the interstellar medium leading to afterglow emission, with γ-rays emission and high energy neutrino production.

The detection of cosmic neutrino from a GRB strongly depends by the burst features, such as its fluence and redshift. In general the GRB neutrino detection seems very promising because, being a transient phenomena, it can be considered background free since the neutrino signal is searched in a time window around the burst.
Thanks the different wavelength radiations characterisimg the GRB emission during its evolution, from X-ray and soft-gamma rays emissions lasting from millisecond to several hundreds of seconds and IR, radio and optical emission during the late afterglow phase, a network of satellites continuously scan the sky searching for GRBs. Despite all these efforts, a neutrino flux from GRBs has never been detected. A GRB analysis presented by IceCube [46] sets an upper limit on the flux of energetic neutrinos associated with GRBs, showing that is at least a factor 3.7 below the predictions. This results could imply that either the proton density in GRB fireball is substantially below the level necessary to produce the highest energy cosmic rays or that physics involved in GRB shocks is different from that one considered by current models.

Chapter 2

Principle of cosmic neutrino detection and Cherenkov neutrino telescopes

The neutrino properties of being a neutral particle with small mass characterise it as a suitable cosmic messenger to investigate astrophysical accelerators. Being neutral and weakly interacting particle, neutrinos can escape from the acceleration regions traveling undisturbed along their path towards the Earth, preserving the directional infromation about the source position. As the same time, the elusive nature of neutrinos makes them difficult to detect and indirect detection techniques are used to identify cosmic neutrinos. Their detection is made even more challenging due to the low intensity of expected flux and the small neutrino cross section. Therefore, huge target masses are required to enhance neutrino interactions, allowing for the production of secondary charge particles which represents the signature for neutrino detection.
An efficient way to obtain a huge volume of target mass as detection medium is to use a large volume of sea-water (or ice), as proposed by Markov and Zheleznykh in 1960 [47]. The sea-water acts as target, shield for atmospheric background and active detection volume simultaneously, where secondary charged particles can be detected exploiting the Cherenkov effect induced in the medium due to their crossing. Therefore, a neutrino telescope can be built arranging several optical sensors, able to detect the Cherenkov light emitted by the secondary charged particles produced in the neutrino interactions with rock and water near the telescope, in a large volume of deep sea water or thick layers of ice.
This chapter is mostly dedicated to the description of the detection principles of cosmic neutrinos. At first, the main neutrino interaction processes of interest for a neutrino telescope are presented. Then the principle of Cherenkov light emission by relativistic charge particles is described, identifying neutrino induced muons as the golden channel for cosmic neutrino detection. After that, the main components of background are discussed and, in conclusion, some of the existing neutrino telescopes and their main results are presented.

2.1 Principles of High Energy Neutrino Detection

High-energy neutrinos can be indirectly detected through the detection of optical photons emitted by secondary charge particles generated in neutrino interactions. Among all the secondary particles muons, produced in charge current muon neutrino interactions, represent the suitable channel for high-energy neutrino telescopes. Being highly penetrating particles and massive enough ($m_\mu \sim 200\, m_e$), at $E_\mu \geq 1$ TeV muons don't lose all their energy via radiative processes and propagate in water or rock for several kilometers. Muons, traveling in water with a velocity greater than the speed of light in the medium, emit Cherenkov radiation (see sec. 2.1.3). The muon tracks can be reconstructed instrumenting a large volume of water with a three dimensional array of optical sensors to detect Cherenkov light. Since at these energies the induced muon is almost collinear with the incident neutrino, it is also possible to infer the arrival direction of the incident high-energy neutrino. A neutrino telescope can also detect, with lower angular accuracy, ν_e and ν_τ through the detection of the Cherenkov light emitted by the electromagnetic cascade in neutral current (NC) and charge current (CC) neutrino interactions (see sec. 2.1.1).

2.1.1 Neutrino interactions

Neutrinos can interact with matter by means of NC interactions, similar for all flavors, or CC interactions. In NC interactions, neutrinos interact with a nucleon and the final state is characterized by a lower energy scattered neutrino and a hadronic shower

$$\nu_l(\bar{\nu}_l) + N \rightarrow \nu_l(\bar{\nu}_l) + X \tag{2.1}$$

while CC interactions produce a relativistic charged lepton, of the same flavor of the incident neutrino, and a hadronic shower

$$\nu_l(\bar{\nu}_l) + N \rightarrow l(\bar{l}) + X \tag{2.2}$$

with $l = \mu, e, \tau$, as shown in Fig. 2.1. Electron-neutrinos interactions produce electrons,

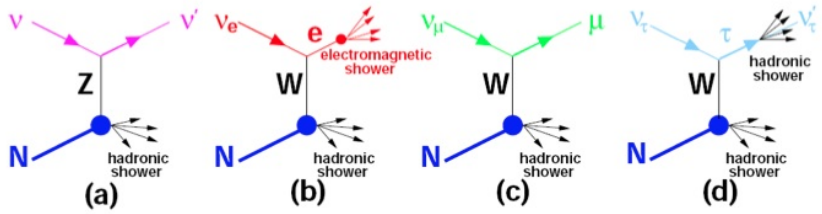

Figure 2.1: Neutrino interactions of interest for neutrino telescopes. (a) Scattered neutrino and a hadronic shower produced by neutral current reaction. (b) Charged current reaction of an electron-neutrino producing an electromagnetic and a hadronic shower; (c) Charged current reaction of a muon neutrino resulting in a muon and a hadronic shower; (d) Double bang event produced by the interaction of a tau-neutrino.

which further decay producing electromagnetic showers, and hadronic showers overlapping with the electromagnetic ones. In high energy tau neutrino interactions a hadronic shower and a τ-lepton are produced. The τ-lepton propagates for relatively shorter distance before decay producing a further hadronic shower. If both these showers are contained inside the detector volume this event shows a characteristic "double bang" feature.
As shown in Fig. 2.2, the three leptons and hadronic or electromagnetic cascades have different path length in water. At E $\geq$ 1 TeV, the long muon range allows the detection of muons produced close to and inside the detector volume, supporting a better muon track reconstruction and becoming the main event signature for neutrino astronomy.

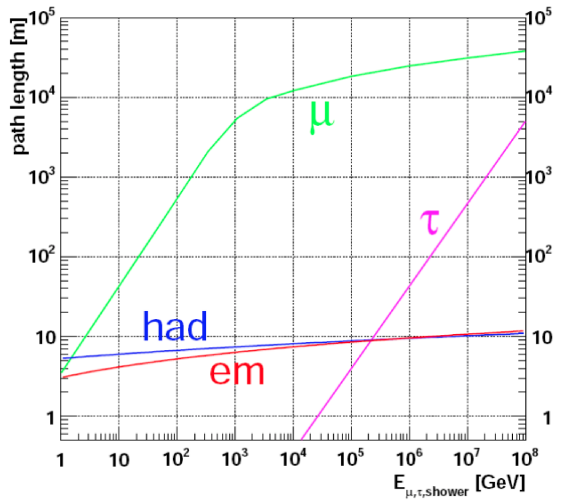

Figure 2.2: Path length of three different leptons, hadronic and electromagnetic showers in water [48].

Neutrino interaction therefore can produce two main different event topologies, the track-like and shower-like events, as shown in Fig. 2.3.
In CC neutrino and anti-neutrino interactions the processes that mainly contribute to the cross section are the quasi-elastic scattering (QE), the resonance production (RES) and the deep inelastic scattering (DIS), that is dominant above $\sim$100 GeV, as shown in Fig. 2.4. At higher energies the cross section for deep-inelastic neutrino-nucleon scattering has been calculated by Gandhi et al. [51] and is shown in Fig. 2.5. For energies below 5-10 TeV the cross section increases linearly with the neutrino energy while for higher energies it is proportional to $E^{0.4}$.
Another important parameter which characterizes the neutrino interactions is the inelasticity y, that represents the fraction of the initial neutrino energy taken by the hadronic shower (see Fig. 2.6). The behavior of neutrino and antineutrino is different below 10^6 GeV. Around 10 GeV the percentage of energy transferred to the shower is about 50% in case of νN interaction and 35% $\bar{\nu}$N [51]. Above 10^6 GeV y is about 0.2 for both neutrinos and antineutrinos.

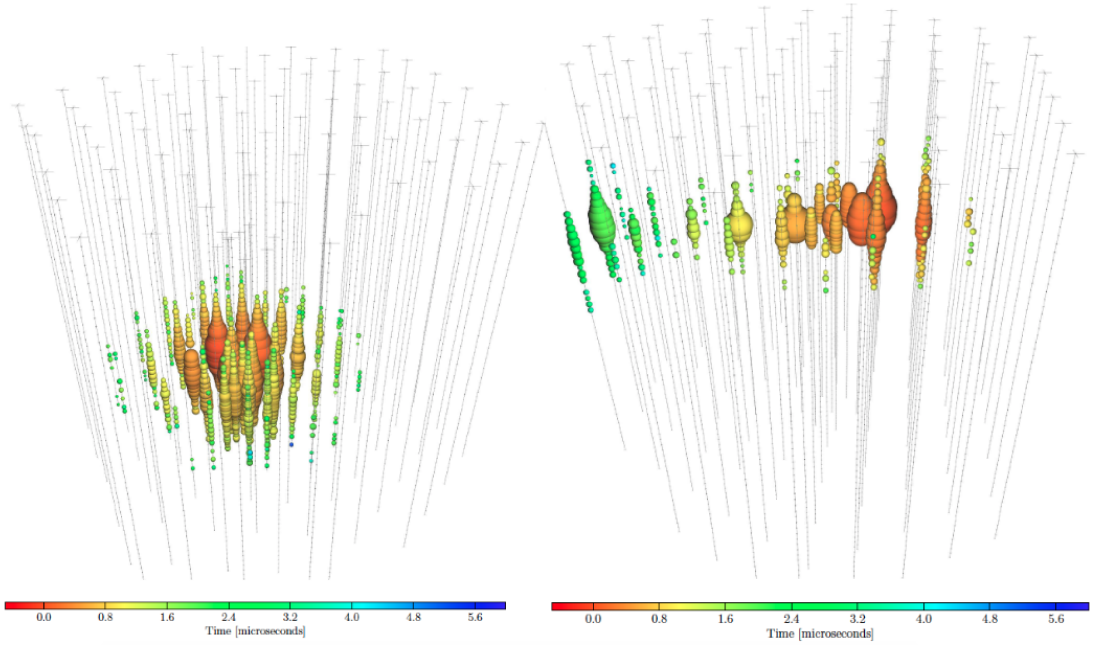

Figure 2.3: Example of a shower-like (left) and a track-like (rigth) event in the IceCube detector obtained through Monte Carlo simulations [49]. The color scale refers to the time evolution of the light deposit.

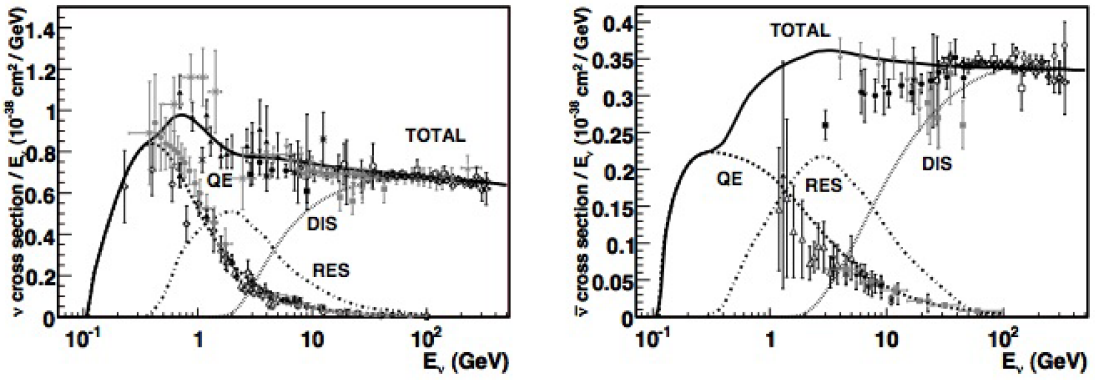

Figure 2.4: Total neutrino (left) and antineutrino (right) charged current per nucleon cross sections divided by neutrino energy and plotted as a function of neutrino energy [50].

By definition the neutrino interaction length is

$$L_{int}(E_\nu) = (\sigma_{\nu N}(E_\nu) < \rho >)^{-1} \tag{2.3}$$

where $< \rho >$ is the medium density. Due to the increase of the νN and $\bar{\nu}$N cross sections the interaction length decreases with E_ν (Fig. 2.7), so that for $E_\nu \geq 40$ TeV it becomes shorter than Earth's diameter and a significant part of the incident neutrinos is absorbed by the Earth.

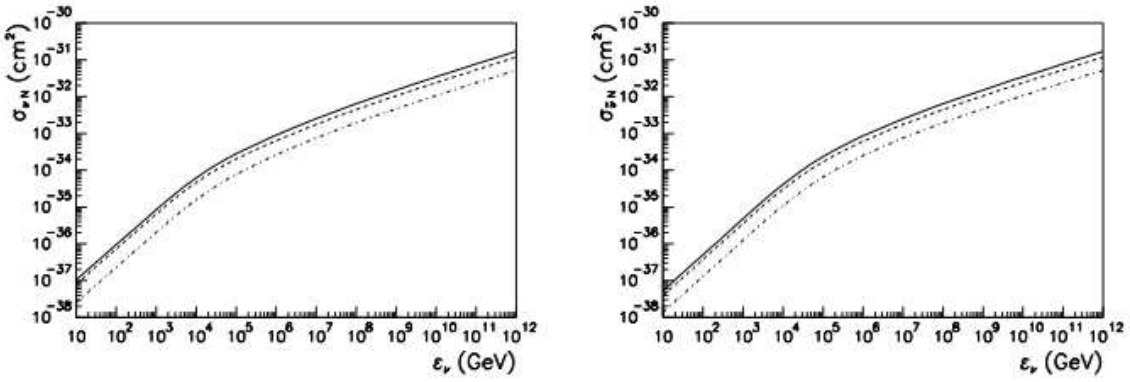

Figure 2.5: The charge current (dashed lines), neutral current (point-dashed lines) and total (solid line) cross section for νN (left) and $\bar{\nu}$N (right) interaction at high energies [51].

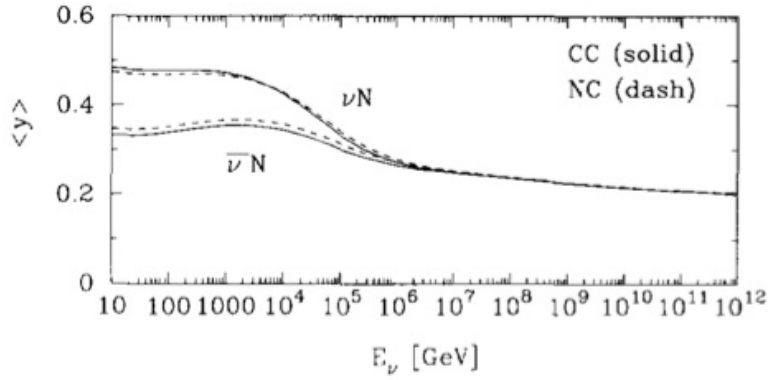

Figure 2.6: The inelasticity parameter y as a function of for charged-current (solid lines) and neutral-current (dashed lines) interactions as a function of the incident neutrino energy [51].

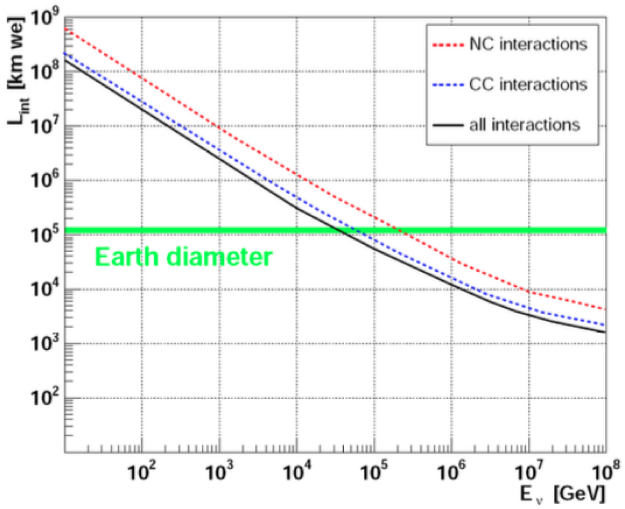

Figure 2.7: Interaction lengths as a function of the neutrino energy for different types of neutrino-nucleon interactions, in km water equivalent [51]

2.1.2 Cherenkov radiation and detection of incoming neutrino

The Cherenkov effect occurs when a charged particle propagates through a dielectric medium of refractive index n at a speed v greater than the phase velocity of light in that medium c/n. The propagating charged particle excites and polarizes atoms or molecules along its path inducing an electric dipole on them. When the charge distribution of molecules comes back to its original configuration, molecules emit a fraction of their excitation energy as polarized light called Cherenkov radiation. As depicted in Fig. 2.8, this radiation is emitted at a characteristic angle θ_C with respect to the direction of motion of the particle and the relation between n and v is given by

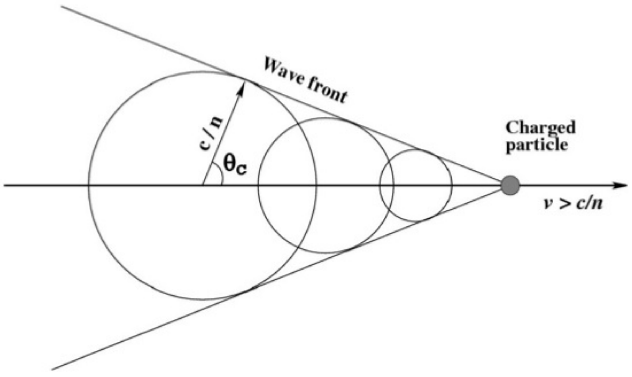

Figure 2.8: Propagation of Cherenkov radiation cone produced by a crossing charged particle moving with velocity greater than the speed of light in the medium.

$$\cos\theta_C = \frac{1}{\beta n} \tag{2.4}$$

with $\beta = v/c$. The number of Cherenkov photons N emitted by a charged particle of charge Ze per unit wavelength interval $d\lambda$ and unit distance dx, is given by

$$\frac{d^2N}{dxd\lambda} = \frac{2\pi\alpha Z^2}{\lambda^2}\left(1 - \frac{1}{\beta^2 n^2(\lambda)}\right) \tag{2.5}$$

where λ is the wavelength of the photon and α is the fine structure constant. In the wavelength range in which water is transparent and the Cherenkov effect has the maximum emission, from 300 to 600 nm, the number of Cherenkov photons emitted per meter of particle track is 3.4×10^4. Being the refractive index of water $n \sim 1.35$, for a highly relativistic particle with $\beta \sim 1$ the Cherenkov angle is $\theta_C \sim 42°$.
The physical process of interest for high-energy neutrino detection is the emission of Cherenkov light by polarized atoms or molecules when high-energy muons propagate in water (or ice) with a velocity greater than the speed of light in the medium. The relation between the incident neutrino direction and muon trajectory is give by

$$\langle\theta_{\nu\mu}\rangle \approx 0.7° \left(\frac{E_\nu}{1\ \text{TeV}}\right)^{-0.7} \tag{2.6}$$

Therefore, at energies of interest for neutrino astronomy the incoming neutrino and the induced muon are almost collinear. Since the Cherenkov angle is known, the reconstruction of the Cherenkov cone through optical sensors allows to reconstruct muon track revealing the incident neutrino arrival direction.

2.1.3 Muon propagation and estimate of neutrino energy

The detection of neutrino induced muons plays a key role for neutrino astronomy. As already seen, at relativistic energies the muon propagation induces the Cherenkov effect in the medium and the detection of Cherenkov radiation allows to reconstruct the arrival direction of incident neutrino. In order to measure neutrino energy, the energy of the muon released inside or near the detector can be considered as a good estimator of the incident neutrino energy.
The muon energy cannot be obtained by direct measurement and it depends on the characteristics of the energy loss of the particle traversing the medium. At all energies, ionization causes a constant and homogeneous energy loss of the muon, while radiative processes like bremsstrahlung, pair production and photonuclear processes become dominant above the muon critical energy of several hundred GeV. In this energy region their contribution to energy loss increases linearly with energy and produce a strongly stochastic fluctuation of the energy losses due to the emission of electromagnetic and hadronic particle cascades along the muon track, where a substantial fraction of the muon energy

is deposited. Therefore, the muon energy loss can only be calculated by statistical approximation of the mean energy loss per unit length. At 1 TeV the total energy loss due to ionization, bremsstrahlung and pair production, can be expressed by the following equation

$$\left\langle \frac{dE}{dx} \right\rangle = -\alpha(E) - \beta(E)E \tag{2.7}$$

where $\alpha(E)$ describes the ionization loss, $\beta(E)$ contains the effect of all radiative processes and can be considered, in a first approximation, as energy independent. From this equation it is possible to derive the muon range R in the medium as

$$R = \frac{1}{\beta} \ln \left(1 + \frac{E_\mu \beta}{\alpha} \right) \tag{2.8}$$

The muon energy losses per unit of path length due to the different processes are shown in Fig. 2.9.

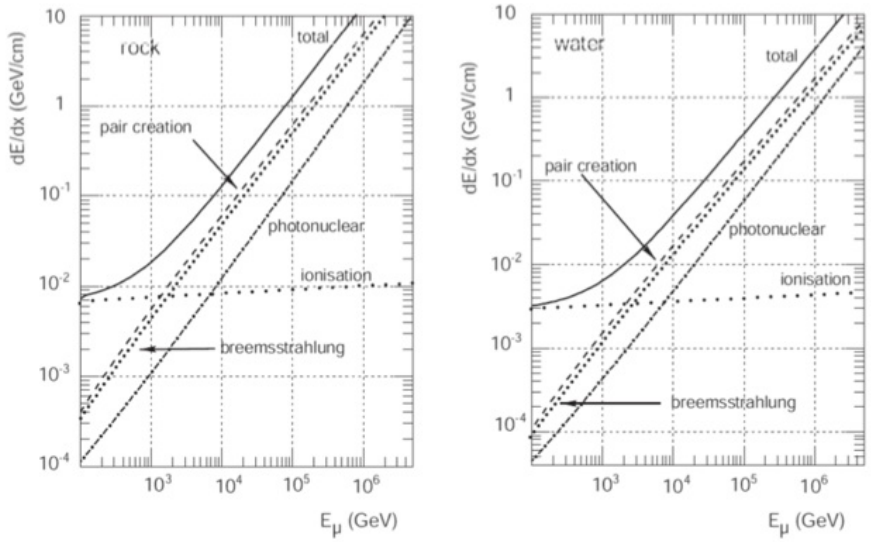

Figure 2.9: Muon energy losses in rock (left) and water (right) as a function of the muon energy [52].

The characteristics of such processes imply two possibilities to reconstruct the muon energy. In the low-energy region (see Fig. 2.9), where ionization dominates the energy loss, the total length of the track can be used to estimate the muon energy if the track ends or is contained within the detector volume. For particles with energies above the muon critical energy, the energy loss in radiative processes can be used to reconstruct particle energy. In fact cascades cause additional photons through Cherenkov emission which arrive at the optical sensors delayed in comparison to direct Cherenkov emission of the muon due to their different emission angle and due to scattering. This delay, called

time residual, and the number of collected photons by optical sensors are therefore the basic observables for muon energy reconstruction in the high energy region. In this region, energy reconstruction has to deal with the highly stochastic nature of muon energy loss, which gives rise to a remarkable uncertainty in the reconstruction of the single muon energy.

2.1.4 Light transmission properties

The attenuation of Cherenkov light in water due to absorption and scattering processes set an upper limit on the maximum distance among the optical sensors in a neutrino telescope. The transparency of sea water as a function of wavelength can be described by the absorption length $\lambda_{abs}(\lambda)$ and the scattering length $\lambda_s(\lambda)$. These quantities represent the paths after which a beam of initial intensity I_0 and wavelength λ is reduced by a factor of $1/e$ due to absorption or scattering. The beam intensity is then described by

$$I_{abs,s(x)} = I_0 exp\left(-\frac{x}{\lambda_{abs,s}}\right) \tag{2.9}$$

where x is the optical path travelled by the beam. The attenuation length $\lambda_{att}(\lambda)$ is defined as

$$1/\lambda_{att}(\lambda) = 1/\lambda_{abs}(\lambda) + 1/\lambda_s(\lambda) \tag{2.10}$$

where $a = 1/\lambda_{abs}(\lambda)$ is the *absorption coefficient*, $b = 1/\lambda_s(\lambda)$ *scattering coefficient* and $c = 1/\lambda_{att}(\lambda)$ *attenuation coefficient* that characterize the light transmission through the matter. In the case of polar ice and clear ocean water the attenuation length is about 100 m [53] and 70 m [54] respectively.
Water is transparent only in a narrow range of wavelengths, 350 nm $\leq \lambda \leq$ 550 nm, as shown in Fig. 2.10. If the distance among the optical sensors is lower than the attenuation length Cherenkov photons can be detected allowing for muon track reconstruction.

2.2 Main background components

The background estimate and its reduction is a crucial and, at the same time, challenging item for most experiments, especially in neutrino astronomy where a statistical excess of events over the expected background is the signature of cosmic neutrino sources. In a neutrino telescope several components of background exist and, in order to improve the detection perfromance, a high capability to identify and reject the different background components respect to the signal events is required.
For a neutrino telescope uncompromising sources of background are the atmospheric muons and the atmospheric neutrinos produced by the interactions of cosmic rays in the Earth's atmosphere. Even though a neutrino telescope is located at huge deep in the sea water or under thick layers of ice to shield it from atmospheric muon flux, atmospheric

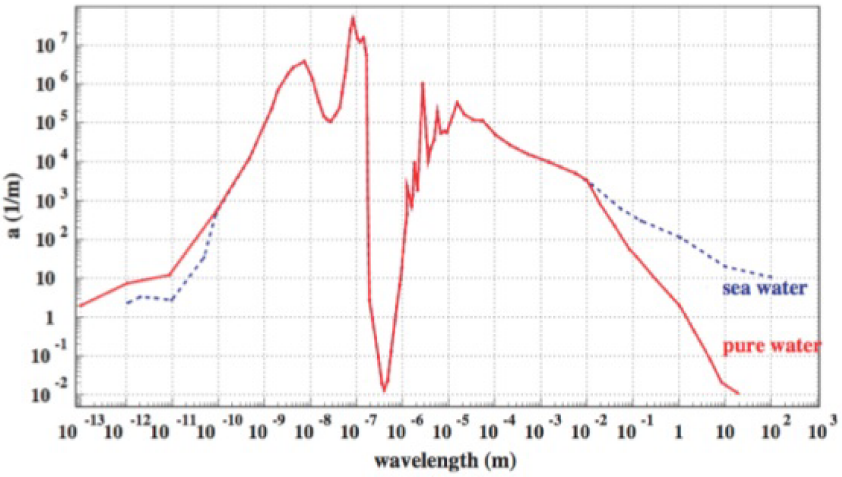

Figure 2.10: Light absorption coefficient as a function of wavelength for pure water (solid line) and sea water (dashed line) [54].

muons and atmospheric neutrinos represent a physical background which produces detectable events that can mimic cosmic neutrinos, as shown in Fig. 2.11.

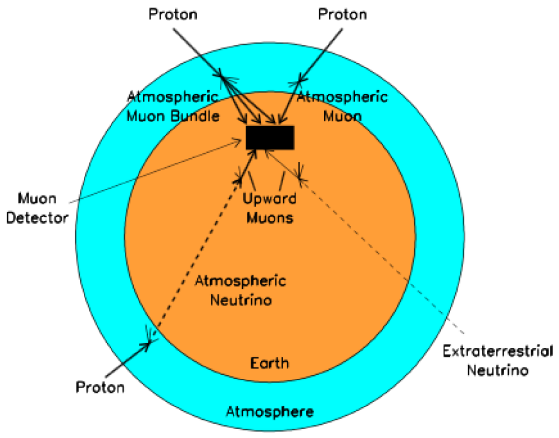

Figure 2.11: Schematic view of the cosmic ray interactions with particles in the Earth's atmosphere responsible for the production of atmospheric muons and neutrinos.

Since only neutrinos can travel through the Earth, atmospheric muons represent the class of down-going events and looking for up-going events is the main strategy to reduce their flux. Due to the fact that atmospheric neutrinos can propagate through the Earth arriving from all over the sky, this approach does not allow to reduce the atmospheric neutrino contribution and further strategies are used in order to discriminate atmospheric from cosmic neutrinos.
In addiction to the physical background, in a water neutrino telescope an other back-

ground component exists, the so called optical background mostly due to the decay of ^{40}K and bioluminescence activity in the sea water. Since the optical background is responsible for uncorrelated signals on optical sensors, the search for time-space correlations among detected photons allows to discriminate the optical background from the Cherenkov radiation emitted by neutrino induce muons.
In the following sections a deeper description of the these background components and of the techniques used to discriminate them from signal events are presented.

2.2.1 Physical background

Atmospheric muons

An important component of background for the detection of astrophysical neutrinos is represented by the atmospheric muons. In fact, the energy of muons produced in the decay of pions and kaons is such that a significant fraction of them can reach and penetrate the surface of the Earth to depths of several kilometers before decaying or being stopped. This downgoing muons produce a measurable signal in the detector, which can be confused with upgoing muons due to cosmic neutrinos. At Earth surface the atmospheric muon flux is about 11 order of magnitude higher than the astrophysical neutrino flux. In order to reduce this component of background, sea water acts as a screen. Even if at depth of $\sim$ 3000 m the atmospheric muon flux is reduced, as shown in Fig. 2.12, it still remains 5 orders of magnitude higher than atmospheric neutrino-induced muon flux.

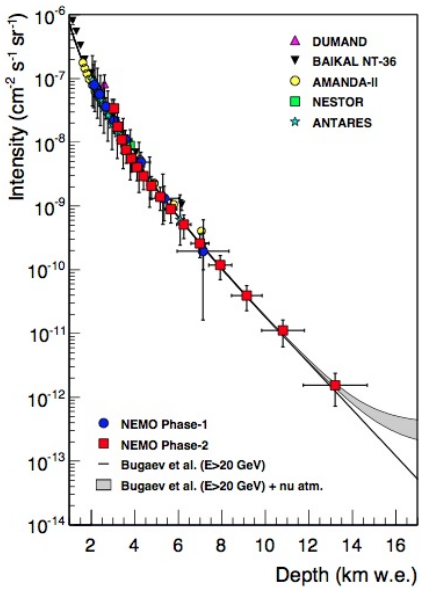

Figure 2.12: Vertical muon intensity versus depth measured using data acquired with the NEMO Phase-2 tower [55]. For comparison, results from other experiments are reported. The solid line is the prediction of Bugaev et al. [56]. The shaded area at large depths includes atmospheric neutrino-induced muons.

The flux of atmospheric muons becomes important with the decrease of the zenith angle. The dependence of the atmospheric muon flux [57] and the muons flux created by atmospheric neutrinos [58], as a function of the zenith angle, is shown in Fig. 2.13.

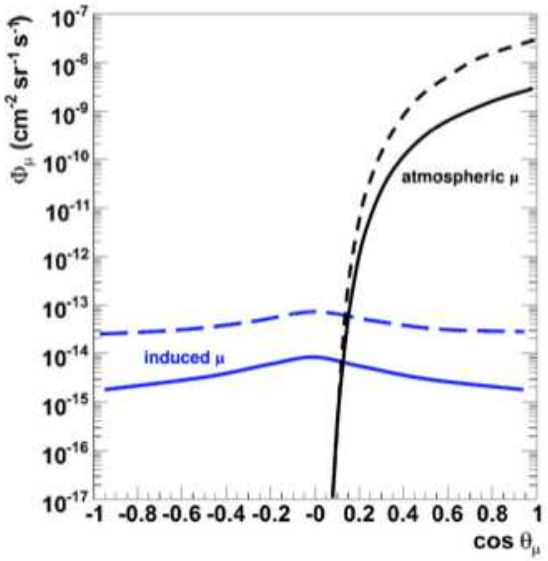

Figure 2.13: Muon background as a function of the zenith angle calculated for 2400 m depth: atmospheric muons (black lines [59]) and muons created by atmospheric neutrino (blue lines [58]). The solid lines represent $E_\mu > 1$ TeV and the dashed lines $E_\mu > 100$ GeV.

Since muons can not traverse the entire Earth diameter ($\sim$ 13000 km), a good strategy to reject atmospheric muons is to discriminate the arrival direction of detected events, considering as signal only up-going muons. Therefore upward-oriented muons events are considered good neutrino candidates.

Atmospheric neutrinos

Another component of background, for the detection of astrophysical neutrino flux, is the atmospheric neutrino flux produced by the interactions of cosmic rays with the particles in the Earth's atmosphere. The products of these interactions are showers of secondaries particles, principally pions and kaons, whose further decay in muons could produce neutrinos. So pions and kaons, decaying in-flight, represent the primary source of atmospheric muon neutrinos, the so called "conventional" atmospheric neutrino flux. Before decay, these mesons lose energy due to the collisions in the atmosphere. The resulting neutrino spectrum has therefore a steeper spectral index than the primary cosmic ray spectrum, equal to ~ 3.7, see Fig. 2.14. Considering γ_p the spectral index of the cosmic ray spectrum, the conventional atmospheric neutrino flux can be expressed as

$$\frac{d\Phi_\nu}{dE_\nu d\Omega}(E_\nu, \theta) = A_\nu E_\nu^{-\gamma_p} \left(\frac{1}{1 + \frac{aE_\nu}{\epsilon_\pi} \cos\theta} + \frac{B}{1 + \frac{bE_\nu}{\epsilon_k} \cos\theta} \right) \tag{2.11}$$

Here all the parameters, the scale factor A_ν, the balance factor B (which depends on the ratio of muons produced by kaons and pions) and the coefficients a and b can be obtained from Monte Carlo computation or from experimental data. The characteristic decay constants are $\epsilon_\pi = 115$ GeV and $\epsilon_k = 850$ GeV respectively, corresponding to the energy at which the hadron interaction and decay lengths are equal.
The uncertainties in the predictions of the conventional atmospheric neutrino flux are dominated by uncertainties in the normalization and spectral distribution of the cosmic ray flux. The atmospheric neutrino flux is not isotropic and shows a dependence on the zenith angle, mainly at higher energies. Additional uncertainties include the ratio of pions to kaons produced by CR interactions which affects the zenith angle distribution perpendicularly near the horizon.

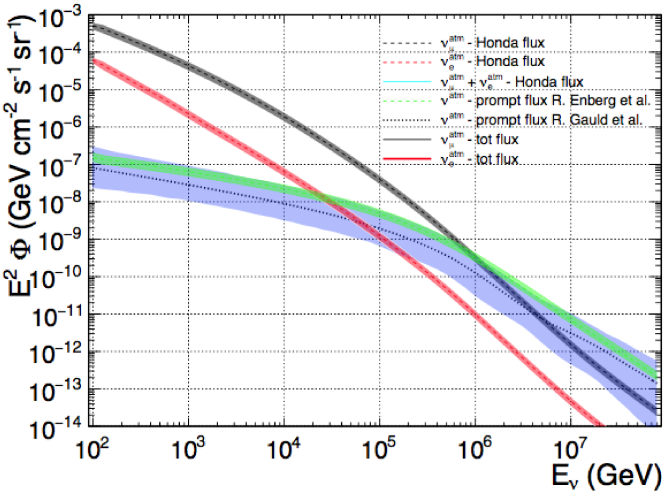

Figure 2.14: Conventional and prompt components of the atmospheric ν_μ and ν_e as a function of the neutrino energy for different models. The bands represent the uncertainties in the conventional (red and black bands) and in the prompt (green and blue bands) components assumed for the analysis carried out in [7].

As the energy increases, the decay lengths of the mesons become longer than their path lengths in the atmosphere suppressing the production of neutrinos, but shorter lived hadrons are also produced. They contribute to the neutrino flux especially from the "prompt" decay of charmed mesons and baryons, producing the so called "prompt" component of atmospheric neutrino flux [60]. The energy dependence of these prompt neutrinos is less steep than the conventional neutrino flux from pion and kaon decays. The energy at which the prompt neutrinos become the dominant atmospheric neutrino component depends on the details of the mechanism for charm production in proton-air collisions at high energies, but it is expected to be important above about 100 TeV. As for the conventional flux, the uncertainties in the normalization and spectral distribution of the cosmic ray flux influence the predictions for the prompt flux. Additional

sources of uncertainty for the prompt flux include charm production cross sections and fragmentation functions, which have not been measured at these energies in accelerator experiments. In [61] the effect of different models of charmed particle production is studied. In Fig. 2.14 the conventional and prompt components of the atmospheric ν_μ and ν_e are shown for different models. As shown in the same figure, in contrast to the models for the conventional neutrino flux, the uncertainty on the prompt neutrino flux is very large. In the simulations performed for both the ANTARES and KM3NeT telescopes the Honda et al. [62] parameterisation for the conventional component, which includes an anisotropy caused by the Earth's magnetic field, and the Enberg et al. [60] model for the prompt component are assumed. In both the Honda and the Enberg model a correction accounting for the presence of the *knee* in the cosmic ray spectrum is applied as prescribed in [63].
Since for energies above the TeV energy range the atmospheric neutrinos have a softer energy spectrum than the astrophysical neutrinos, an energy estimator is exploited to discriminate between them. Then during the analysis, cuts on the values of the energy estimator parameter associated to each event allow to reduce the contribution due to atmospheric neutrino background.

2.2.2 Environmental optical background

Even if the neutrino telescope is installed at great depth to reduce the propagation of atmospheric muons and neutrinos, in sea water another component of background exists, the so called optical background. This background is not related to events misidentified as cosmic neutrinos, like in the previous case, but it is related to the light produced in the water environment. This optical background gives spurious signals on the optical sensors which can be exchanged as photons due to muons. Since muon track reconstruction algorithms look for time-space correlation between detected photons, accordingly to Cherenkov photons emitted along muon track, the optical background makes the muon track reconstruction more complex. The search for local coincidences between optical sensor turned out to be the best strategy to select atmospheric muons over the optical background.

2.2.3 Radioactivity

The main contributions to optical background is the Cherenkov radiation emitted by propagating charged particles originated in the decay of radioactive elements in sea water. The most abundant radioactive element is ^{40}K which has two main decay channels

$$^{40}K \rightarrow {}^{40}Ca + e^- + \bar{\nu_e} \qquad B.R. = 89.3\% \tag{2.12}$$

$$^{40}K + e^- \rightarrow {}^{40}Ar + \nu_e + \gamma \qquad B.R. = 10.7\% \tag{2.13}$$

In the first process the emitted electron has sufficiently energy to induct the Cherenkov effect on surrounding molecules. The photon in the final state of capture process produced

with energy of 1.46 MeV can lead to the production of electrons with energies over the threshold for Cherenkov light emission. Cherenkov light produced by a single ^{40}K decay consists of uncorrelated light pulses that may produce many photons within 1 ns, giving raise to coincidences on neighboring optical sensors.

2.2.4 Bioluminescence

In deep sea water it is possible to identify two components of bioluminescent light with different time scales. One component derives from bacteria [64], with a characteristic time scale varying from hours to days. The rate of detected photons produced by this steady component can be similar to that one produced by ^{40}K decay and it is typically homogeneous over the full detector. The second component is represented by "bursts" of light with durations of the order of seconds. Burst of light can produce rates that are orders of magnitude larger than the ones due to the steady background and involves only a local group of optical modules.
The estimation of both components of optical background is necessary for the evaluation of the site properties and to keep under control their impact on data taking. In the case of the Capo Passero site, the installation site of the KM3NeT/ARCA telescope, water samples picked up at different depth have been analysed searching for the presence of luminescent bacteria cultivable at atmospheric pressure. As shown in Fig. 2.15, the luminescent bacteria are essentially absent at depths beyond 2500 m [65].

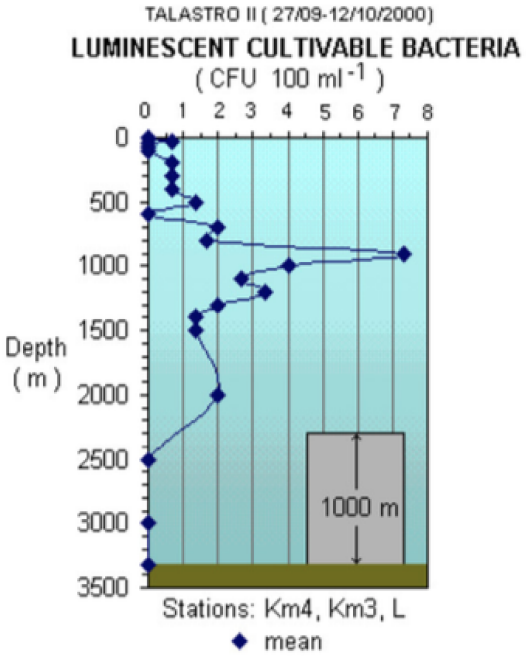

Figure 2.15: Concentration of luminescent bacteria cultivatable at atmospheric pressure as a function of depth [65]. The data have been obtained from water samples taken at the Capo Passero site.

2.3 Cherenkov neutrino telescopes

This section is dedicated to the description of the Baikal telescope and the under ice IceCube neutrino observatory. Since the activity carried out during the PhD involved both the analysis of the ANTARES data sample and the monitoring of the data collected with the first two detection units of the KM3NeT/ARCA infrastructure, the description of the ANTARES and KM3NeT infrastructures and of their main results will be widely presented in chapter 3.

2.3.1 Baikal

After the pioneering work of the DUMAND collaboration off shore of the Hawaii islands, the Baikal experiment played a important role in neutrino astronomy conducting neutrino research below the surface of the siberian Baikal Lake since 1993. The Baikal collaboration built the first neutrino telescope in the northern hemisphere, the Baikal Deep-Underwater Neutrino Telescope [66], located at a distance of 3.5 km from the shore and at a depth of 1100 -1300 m in the south part of the Baikal lake. At first, the detector comprised only three strings carrying 36 optical sensors in total. The actual configuration named $NT200+$, which consists of 192 optical sensors deployed on eight strings, takes data since 2008. The Baikal lake is characterized by a high bioluminescence and a short

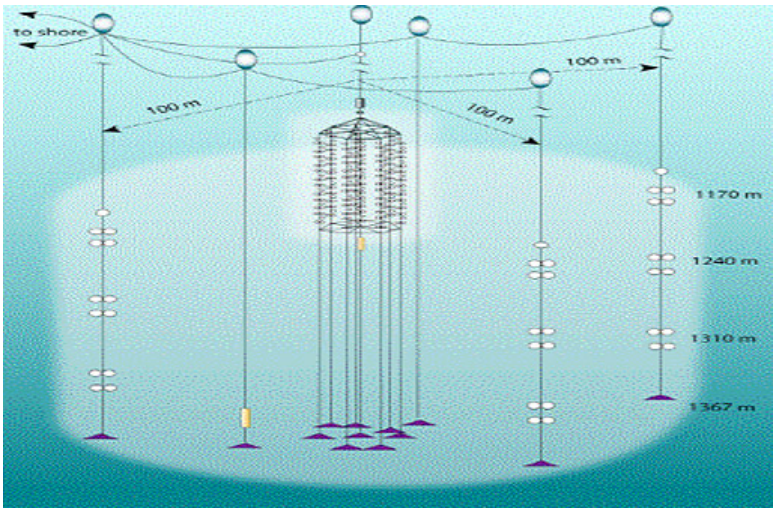

Figure 2.16: Schematic view of Baikal neutrino telescope.

absorption length and, due to its relatively low depth, the Baikal telescope suffers also high atmospheric muon background.
Starting from 2013, Baikal collaboration is working on technologies to build a km^3-size telescope in Lake Baikal. The new configuration, the $NT1000$, will be located in the vicinity of $NT200+$ and will consist of 12 clusters with 8 strings in each cluster [67].

2.3.2 IceCube

IceCube, a neutrino observatory located in the South Pole, is the first and largest operating km^3 neutrino telescope [68] on the Earth. It comes from the work of the AMANDA collaboration [69], which was built in the middle of 1990s, to demonstrate that the Antarctic ice is a suitable target for the detection of energetic neutrinos.
The IceCube detector is located at a depth of about 3500 m and it is covered by a layer of ice almost 2500 m thick, as shown in Fig. 2.17. The detector includes a surface array, IceTop, and a denser inner sub-detector, the DeepCore. The in-ice component of IceCube consists of 5160 digital optical modules (DOM), each with a 10-inch PMT and associated electronics. The DOMs are attached in 86 vertical strings and arranged in a volume of a cubic kilometer from 1450 m to 2450 m depth. The strings are deployed on a

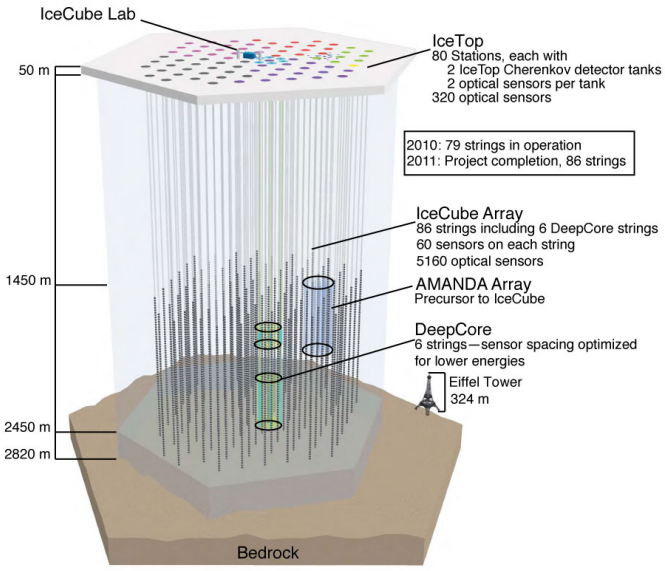

Figure 2.17: Layout of IceCube detector, with IceTop surface array and DeepCore detector [70].

hexagonal grid with 125 meters spacing and hold 60 DOMs each. The vertical separation of the DOMs is about 17 m. The deployment of all 5160 optical sensors was completed in December 2010. During the construction phase the deployed parts of the detector produced already high-quality data.
At the center of the array, six of these strings are deployed more compactly, with a horizontal separation of about 70 m and a vertical DOM spacing of 7 m. This denser configuration forms the DeepCore sub-detector, which lowers the neutrino energy threshold at about 10 GeV. DeepCore was designed to avoid the high dust concentration between 2000 and 2100 m, denoted the “dust layer”, and it is situated at about 2100 m below the surface of the ice. The detector began taking physics data in May 2010 with a partial

configuration. Its location is useful due to the exceptionally clear ice at those depths and allows it to use the surrounding IceCube detector as a highly efficient active veto against the background of downward-going muons produced in cosmic-ray air showers.
IceTop is a km^2 array of particle detectors that is installed above the IceCube neutrino telescope. It is used to detect extended particle showers induced in the Earth's atmosphere by high-energy cosmic rays. It is constituted by 80 stations equipped with a pair of Cherenkov ice tanks distributed on the ice surface with an average distance of 125 m, which allow the observation of cosmic rays with energies between 10^{14} eV and 10^{17} eV.
An all-sky search for high-energy neutrino events interacting within the IceCube neutrino detector, conducted between May 2010 and May 2012, led to the detection of two PeV neutrino events [49]. Further events were observed, substantially more than what expected from atmospheric backgrounds. These events, which include the highest energy neutrinos ever observed, have flavors, directions, and energies inconsistent with those expected from the atmospheric muon and neutrino backgrounds. These properties are consistent with generic predictions for an additional component of extraterrestrial origin, leading to the discovery of a flux of high-energy neutrinos of cosmic origin. Different analyses of multiple years of IceCube data have revealed more than 100 astrophysical neutrino events. The IceCube data are consistent with a spectrum given by $E_\nu^2(dN_\nu/dE_\nu) \simeq 10^{-8}$ $\mathrm{GeVcm^{-2}s^{-1}sr^{-1}}$ up to an energy of $\sim$ 2 PeV, the energy of the so-called "Big Bird" event. No neutrino induced events have been seen above 2 PeV. Several neutrino events above 3 PeV would be expected if the E_ν^{-2} spectrum extended to higher energies. Thus, the lack of neutrinos above 2 PeV energy may be an indication of a possible cutoff in the neutrino spectrum.
Further analyses performed by the IceCube collaboration [1, 2, 71], based on the search for a diffuse neutrino flux of cosmic origin, yielded a measurement of an excess of cosmic neutrino events over the expected background. Assuming an isotropic astrophysical neutrino flux at Earth in flavor equipartition, the all flavor energy spectrum of the measured excess can be fitted by a simple power law $dN_\nu/dE_\nu = \Phi_0 E_\nu^{-\Gamma}$ with a normalization factor at 100 TeV equal to

$$\Phi^{3f}(100\ \mathrm{TeV}) = 6.7^{+1.1}_{-1.2} \times 10^{-18} \quad [\mathrm{GeV\ cm^2\ s\ sr}]^{-1} \tag{2.14}$$

and a spectral index $\Gamma = 2.5 \pm 0.09$. A different analysis, mainly aimed to search for muon neutrinos coming only from the Northern sky, yielded a best-fit single-flavor neutrino spectrum with a different normalization factor at 100 TeV

$$\Phi^{1f}(100\ \mathrm{TeV}) = 0.9^{+3.0}_{-2.7} \times 10^{-18} \quad [\mathrm{GeV\ cm^2\ s\ sr}]^{-1} \tag{2.15}$$

and different spectral index $\Gamma = 2.13 \pm 0.13$ [71]. The tension between the two measurements could be the hint of the presence of a multiple cosmic contributions to the IceCube signal [72]. Since the contribution from the galactic plane and galactic sources is stronger in the Southern hemisphere, where the Galactic Center is located, this result can be an indication that the muon neutrino flux coming from the Northern sky is mostly

of extragalactic origin.
Recently the detection of a high energy neutrino event [4], together with observations in γ-rays and at other wavelengths, led to consider the Blazar TXS 0506+056 as a high energy neutrino source. The neutrino candidate event, *IceCube-170922A*, was detected on 22 September 2017 and classified as an Extremely High Energy (EHE) event. The direction of event was consistent with the location of TXS 0506+056 (located at right ascension 77.3582° and declination +5.69314°) and coincident with a state of enhanced γ-ray emission observed since April 2017 [73] by the Large Area Telescope (LAT) on the Fermi Gamma-ray Space Telescope [74]. Follow-up observations of the same source performed by the MAGIC telescopes [75, 76] allow to detect γ-rays with energies up to 400 GeV. The significance of the spatial and temporal coincidence of the high energy neutrino and the flare of TXS 0506+056 was estimated to be at the 3σ level [77]. Since an excess of high energy neutrino events, with respect to the atmospheric background, was found at the same location in the sky during the period of time between September 2014 and March 2015, this result suggest that the TXS 0506+056 could have emitted high energy neutrinos also before the detection of the IceCube-170922A event classifying such blazar as high energy neutrino source.
Since the modest numbers of cosmic neutrinos measured in a period of data taking which cover almost a decade, the IceCube collaboration proposes to build $IceCube-Gen2$ [78], an expanded array of light-sensing modules that should instrument a 10 km^3 volume for detection of high-energy neutrinos, with the goal to increase the sensitivity to astrophysical neutrinos of all flavors.
With the goal of determining the neutrino mass hierarchy, the IceCube collaboration is also planning to build the Precision IceCube Next Generation Upgrade (PINGU) [79]. Different detector geometries have been considered. The candidate geometries are those that can be deployed in a short period of time with adequate inter-string horizontal spacing and sufficient inter-DOM vertical spacing, satisfing drilling and deployment constraints. PINGU can also extend the search for solar WIMP dark matter.

Chapter 3

Mediterranean underwater neutrino telescopes

With the IceCube observation of a diffuse neutrino signal of cosmic origin [1, 2] the era of neutrino astronomy has began. Furthermore, the recent detection of the high energy neutrino event *IceCube-170922A* [4, 5], in coincidence with the γ-ray emission of the Blazar TXS 0506+056, allows for consideration on blazars as point sources of high energy neutrinos. Despite these observations represent a milestone result in the field of neutrino astronomy, the astrophysical sources responsible for the origin of the observed diffuse neutrino signal are still unknown. In fact, the IceCube location at the South Pole does not allow for a direct observation of the nearest gamma ray sources to the Earth, which could provide important constraints on the origin of the diffuse neutrino signal detected by IceCube. On the contrary, neutrino telescopes located in the opposite hemisphere of the Earth can play a crucial role for the investigation of the nature of such cosmic neutrino flux. By using up-going neutrinos, they can point towards the most powerful galactic gamma ray sources, as the Centre of the Galaxy or the Galactic Plane.
The Mediterranea Sea represents a suitable site to build a neutrino telescope. Thanks to its location it allows to obtained a large coverage of the entire sky, extending the neutrino astronomy in a complementary region of the Universe with respect to that one accessible by the IceCube experiment. Furthermore, the deep sea water properties of the Mediterranean Sea, the very small light scattering that allows to reach a good angular resolution and a natural background easy to handle, characterise it as a suitable site to host a neutrino telescope with high performances.
Above mentioned reasons led to the construction of the ANTARES (Astronomy with a Neutrino Telescope and Abyss environmental RESearch) telescope, which is the largest and more sensitive neutrino telescope in the northern hemisphere, with the main scientific goal to discover astrophysical neutrino sources in the TeV-PeV energy range.
The ANTARES collaboration has made a great deal of effort in the field of neutrino astronomy. Several analyses have been performed searching for both point-like and extended neutrino sources, and sources of diffuse neutrino fluxes as well. Even though no cosmic neutrino source has been discovered, upper limits have been set, proving the

great potential of the ANTARES telescope especially in the southern sky. During the latest years a growing interest has been pointed toward the ANTARES telescope. In fact it could provide valuable information on the study of the neutrino excess observed by the IceCube detector [2, 71, 72], especially in the case of the presence of a Galactic contribution. Exploiting the lower energy threshold, ANTARES can constrain such a contribution, which is expected to be more intense at lower energies with respect to an extragalactic component.
In addition to neutrino astronomy, other fields of research have been investigated using ANTARES data. Major interest has been addressed to real-time follow-up analyses and alert triggering, transient phenomena analysis, multimessenger astrophysics and search for dark matter.
Recently, the search for the neutrino counterparts to the HAWC γ-ray sky using 10 years of ANTARES data has started and represents the main topic of this thesis. A detailed description of the analysis procedure and the results will be presented in Chapter 5 and Chapter 6.
With the main goal to extend the ANTARES performances, the KM3NeT (km^3-scale Neutrino Telescope) collaboration started to build a new multi-km^3 research infrastructure in the Mediterranea Sea which will drive towards promising breakthrough both in the field of neutrino astronomy and neutrino physics. The KM3NeT research infrastructure will host two neutrino telescopes: the ARCA (Astroparticle Research with Cosmics in the Abyss) telescope, for the search of high energy neutrino sources in the Universe, and the ORCA (Oscillation Research with Cosmics in the Abyss) telescope, whose main physics goal is the determination of the neutrino mass hierarchy.
In this chapter a detailed description of the ANTARES and KM3NeT detector components, acquisition systems and calibration procedures is presented. Some of the main ANTARES results will be also illustrated. In the end, to show the high quality performances achievable with the ARCA and ORCA telescopes, the sensitivity studies performed through MC simulations will be discusses in dedicated sections.

3.1 The ANTARES Telescope

The ANTARES telescope is located in the Mediterranean Sea, 40 km offshore of Toulon, France, at a depth of 2500 m and it was completed in May 2008. It is composed by 12 vertical structures, named lines, holding optical sensors designed to detect the Cherenkov light emitted by relativistic charged particles produced in neutrino interactions. The basic detection element of the ANTARES telescope is the Optical Module (OM) housing a photomultiplier tube (PMT). A mechanical structure which supports three OMs, looking downwards at 45°, together with a titanium container, the Local Control Module (LCM) which housing the offshore electronics and embedded processors, constitute the Optical Module Frame (OMF). In each line 25 OMFs are linked trough an Electro-Mechanical Cable (EMC), with an interspace of about 14.5 m, and the deepest OMF is located at $\sim$ 100 m from the sea bed. Each line is anchored on the seabed and it is held vertical by a buoy at the top, as sketched Fig. 3.1. In the nominal configuration 11 lines are equipped

as described above, while the line 12 hosts 20 OMFs and many devices dedicated to acoustic neutrino detection study and the measurement of the environmental parameters for a continuous long term site monitoring.

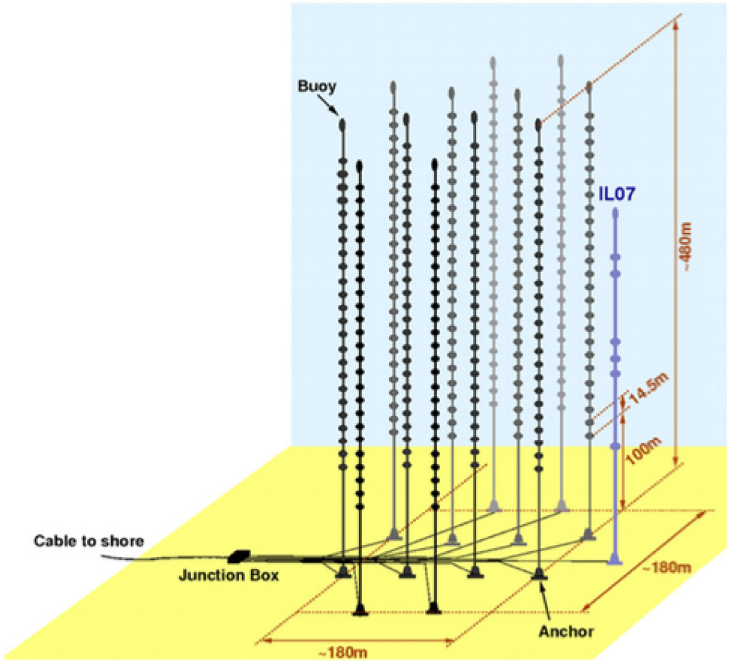

Figure 3.1: Schematic view of the ANTARES detector.

The ANTARES lines are arranged on the seabed in an octagonal configuration, as shown in Fig. 3.2, with a total number of 885 installed OMs. The data communication and the power supply provided to the lines is done through the Inter Link cables (IL), the Junction Box (JB) and the Main Electro-Optical Cable (MEOC). The ANTARES collaboration follows the *all-data to shore* concept. All raw data are sent to on-shore, where the ANTARES control room is situated and the required data processing method can be applied. This approach minimises the loss of physics signal and allows to apply different processing methods depending on the desired physics analyses carried out.

3.2 Positioning system and time calibration system

Since the reconstruction of the tracks of incident neutrinos is based on the measurement of the arrival times of the Cherenkov photons on PMTs, the knowledge of the OM position, with a precision better than 10 cm, is required to achieve an angular resolution of a few tenths of a degree. Due to the flexible nature of the ANTARES lines, weak water currents can move or rotate the lines producing a displacement of the OMs of several metres. In the ANTARES telescope a real time positioning is done using a positioning system [80], which consists of an acoustic system, for distance triangulation, and a compass-tiltmeter

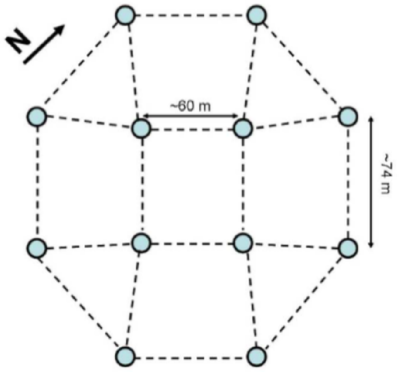

Figure 3.2: Illustration of the ANTARES detector layout. The dots represents the line position in the octagonal configuration of the telescope. The average distance among the lines is also reported.

system, for the measurement of the orientation and inclination of the storeys. The acoustic positioning system consisting of emitters on the sea floor around the detector and at the anchor of each line. Receiving hydrophones are arranged on five storeys of each line. This system measures the position of the storeys by triangulation. While the compass-tiltmeter system installed on each storey allows to measure the orientation and inclination of the storey itself. The information provided by both systems is combined and the shape of each line is reconstructed through a χ^2 fit. The position and orientation of each optical module is then determined from the line shape.
In addiction to the positioning system, a time calibration should be ensured to achieve optimal performance in term of angular resolution. In fact a good angular resolution is obtained if the relative time offsets between the PMTs is measured at the level of about 1 ns. The time calibration procedure is much more complex of the previous one, since the time calibration of several detector component is needed. At first, the time slot between the incident photon on the PMTs and the time stamping of the associated signal must be determined. This is strongly dependent on the front-end electronics response time, the PMT signal transit time and the length of the cable linking the OM to the LCM. Therefore, the intrinsic time offsets of the system must determined and it is done through a dedicated calibration procedure in a dark room before the deployment. These intrinsic time offsets, which should be constant, can slightly change after the deployment due to the temperature changes and the stressing of cables. Moreover, the variation of the high voltage applied to the PMTs could cause modifications in these time offsets. In order to keep under control these time offsets, an optical beacon system is used, ensuring periodically monitoring and time offset re-computation. At the end, to synchronise the whole detector, a master clock system on the shore station delivers a common reference time, derived from GPS, to all the offshore electronics and ending in each LCM. At this point the time calibration of each LCM is done considering the corresponding propagation of half of the round-trip time of the common reference time send to each individual LCM and coming back to the shore station.

3.3 Data acquisition system

The data acquisition system (DAQ) of the ANTARES detector is responsible for the digitisation of the PMT signals, data transport, data filtering, and data storage [81]. The DAQ system is mainly composed by the DAQ software and the off-shore and on-shore hardware. The DAQ software is composed by all those programs, running both in on-shore and off-shore hardware, that take care of the data transfer and communication, control the operation of the detector and data taking.
The off-shore hardware is composed by all the off-shore electronics. Most of these electronics modules, the "sector module", are used to read out the PMT output. These modules house the electronics needed for the digitisation of the analogue signals from the PMTs and the data transport. The sector modules include several analogue ring sampler (ARS) chips, a local clock, a field programmable gate array (FPGA) and a processor with an Ethernet port. During the data taking the ARS chips take care of the digitisation of the timing of each PMT signal and the total charge of the pulse. The setting of each ARS chip parameters can be modified, including the threshold and the integration gate. The voltage threshold is set to eliminate small pulses due to the dark current in the PMT and typically a value corresponding to 0.3 photo-electrons is used. The integration gate is set to integrate most of the PMT signal but, at the same time, to limit the contribution of electronic noise. A local clock is used by the ARS chips to timestamp each PMT signal above threshold.
The combined time and charge information of the PMT signal, within the integration time, represent a single photo-electron hit. At this step of data acquisition the hits are named L0 hits. The data from the ARS chips are buffered by the FPGA into separate frames with a time length between 10 and 100 ms.
The processor in the off-shore electronics modules is the interface between the ARS chips and the online data processing system. The operating system on these processors is used for the data transport.
At the bottom of each line an extra container houses an electronics module, the "string module", used for the slow control of the electrical power system and the calibration systems of the detector line and also for the distribution of the clock signal as well.
For the data transport between the off-shore and on-shore parts of the detector the Dense Wavelength Division Multiplexing (DWDM) technique is used. The DWDM system can be considered as a large fibre-optic network, that uses multiple wavelengths to transmit different streams of data along a single fibre. It is also used for the transmission of the slow control data and the distribution of initialisation and configuration data. Each string is connected with an electro-optical cable to the Junction Box (JB), where the cables from the 12 detector lines end up. Then, the JB is connected to the shore station with a single 40 km long electro-optical cable.
The on-shore DAQ system is located in the shore station and consists of standard PCs, a large Ethernet switch, the DWDM hardware and the master clock system. The software programs running on these PCs are responsible for the control of the detector operation, data transfer and communication, data processing, monitoring, and data storage. These

programs are all part of the DAQ software. All the PCs are connected to the Ethernet switch, to which the off-shore DAQ system of all lines is connected forming a large Ethernet network.
Since the *all-data to shore* concept is used, all the raw data are handled by the on-shore DAQ system. The raw data rate on-shore depends on the background and on the number of active lines, and usually ranging from 0.3 GB/s to 1 GB/s. At this stage of data acquisition a trigger condition is applied in order to reduce the amount of background data. This is done through an online processing of the data by the DataFilter (DF). A first trigger level, Trigger Level L1, allows to select the so called L1 hits, which corresponds either to coincidences of L0 hits on the same OM triplet of a storey within 20 ns, or to a single high amplitude L0. Then the DataFilter looks for a physics event by searching a set of correlated L1 hits on the full detector in a time window of ~ 4 μs applying a second level of trigger, the L2. Only if an event is found all the L0 hits detected by the full detector, during the considered time window, are stored as L2 hits. Further trigger conditions are then applied by a trigger logic algorithm during the analysis of data as described in sec. 4.7.

3.4 ANTARES main results

The ANTARES neutrino telescope has been monitoring the sky for almost a decade, playing an important role in the field of neutrino astronomy. In fact, being the largest operational neutrino telescope ensuring a coverage of the Southern sky with a better angular resolution and lower energy threshold than IceCube, it has been giving an important contribution to the observation of promising high energy neutrino sources in the Southern hemisphere of the Universe. Several physics analyses have been carried out by the ANTARES Collaboration, not only with the purpose to reach important breakthrough in the field of neutrino astronomy but also to use neutrino physics as an alternative approach to investigate physics processes involved in others fields of research. Then, this section is dedicated to the description of some of the main recent analyses performed by the ANTARES collaboration thanks to which very important achievements have been obtained.

3.4.1 Diffuse flux searches

All-sky diffuse flux search

In order to confirm the IceCube observation of a diffuse cosmic neutrino flux [1, 71], a search for an all-flavor diffuse cosmic neutrino flux all over the sky has been recently performed by the ANTARES collaboration [82]. The main reason pushed for this analysis relies on the possibility that the ANTARES telescope can provide important information on the study of the IceCube signal thanks to its lower energy threshold. In fact, the galactic component presents in the diffuse flux observed by IceCube it is expected to be more intense at lower energies with respect to an extragalactic one and it can be easily constrained thanks the ANTARES low energy threshold.

For the first time an all-flavor search has been performed using both track-like and shower-like events collected from 2007 to 2015, with a corresponding equivalent livetime of 2450 days. The analysis follows a blind policy, according to which all cuts are optimized on Monte Carlo simulated events, with only 10% of the data used to check the agreement with simulations.
The search method follows a two-step procedure. At first an event selection chain is used to reduce most of the background due to atmospheric muons, mainly based on cuts on the zenith angle of the reconstructed events. Then, since at high energies a cosmic neutrino flux has a harder energy spectrum than the atmospheric one, to maximizes the sensitivity of the search a further selection is done applying cuts on the energy estimator parameter of the events. In the end, the Model Rejection Factor (MRF) procedure [83] based on the Feldman and Cousins upper limit estimation [84] is applied.
For cosmic neutrinos an isotropic flux all over the sky, equally distributed into the three neutrino flavors and between ν and $\bar{\nu}$, is assumed. This cosmic neutrino flux is modeled by a single power law energy spectrum with two possible spectral indexes, $\Gamma = 2.0$ and $\Gamma = 2.5$, and normalization factor at 100 TeV equal to $\Phi_{1f}(100\ \text{TeV}) = 10^{-18}$ [GeV cm^2 s sr]$^{-1}$ and $\Phi_{1f}(100\ \text{TeV}) = 1.5 \times 10^{-18}$ [GeV cm^2 s sr]$^{-1}$ respectively.
After the unblinding a small excess of events was found in both data samples, with a total of 33 events, 19 tracks and 14 showers, while the expectation from Monte Carlo simulations for the background was of 24 events, 13.5 tracks and 10.5 showers, with an estimated uncertainty of $\pm$ 7 events. The result is translated into a 68% confidence interval (C.I.) and a 90% confidence level (C.L.) upper limit (U.L.), as reported in Tab. 3.1.

Table 3.1: Sensitivity and results after the unblinding of the data. The one-flavor 90% confidence level sensitivity $\Phi_0^{1f,90\%Sens.}$ and upper limit $\Phi_0^{1f,90\%U.L.}$ flux normalization factors at 100 TeV are reported in units of [GeV cm^2 s sr]$^{-1}$. The 68% confidence intervals, under the assumption of a cosmic spectrum proportional to $E^{?2}$ and $E^{?2.5}$, are also reported. Systematic effects are included into these estimations.

	$\Gamma = 2.0$	$\Gamma = 2.5$
${\Phi_0}^{1f,90\%Sens.}(100\ \text{TeV})$	1.2×10^{-18}	2×10^{-18}
${\Phi_0}^{1f,90\%U.L.}(100\ \text{TeV})$	4.0×10^{-18}	$2 \times 6.8 \times 10^{-18}$
${\Phi_0}^{1f,68\%C.I.}(100\ \text{TeV})$	0.29 - 2.9×10^{-18}	2×0.5 - 5.0×10^{-18}

Even though the significance of the observation is not large, the null cosmic flux hypothesis can be excluded at 85% C.L..
Then a maximum-likelihood method is used to evaluate the best-fit energy spectrum of the measured excess. The 2D log-likelihood profile is shown in Fig. 3.3, where the 68% and 90% C.L. contours from this analysis are shown together with the best-fit results from IceCube analyses.
Despite of the 2D log-likelihood profile shows a minimum, it does not allow to constraint significantly the properties of the cosmic signal, excluding only hard spectra or intense fluxes. The best-fit cosmic flux from ANTARES data yields a single-flavor normaliza-

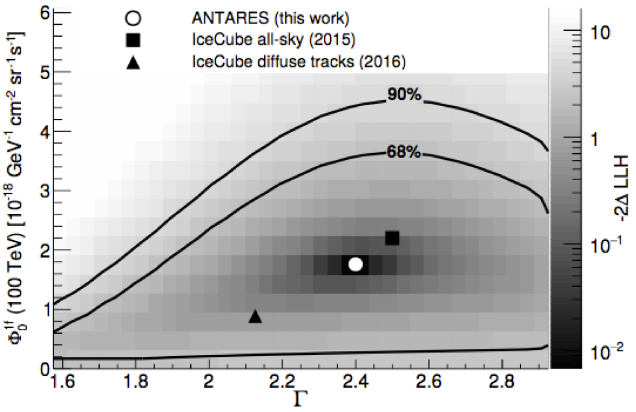

Figure 3.3: The 2D log-likelihood profile of the diffuse cosmic flux normalization and spectral index [82]. The black lines represent the 68% and 90% confidence level. The best-fit point from this analysis is reported as empty circle together with the IceCube best fits from the all-sky combined analysis (full square) and the diffuse flux analysis using tracks (full triangle). The color gradient represents the log-likelihood difference with respect to the best-fit point.

tion factor at 100 TeV of Φ_0^{1f} (100 TeV) $= (1.7 \pm 1.0) \times 10^{-18}$ [GeV cm^2 s sr]$^{-1}$ and a spectral index equal to $\Gamma = 2.4^{+0.5}_{-0.4}$ with a 68% C.L.. This results allows to exclude the hypothesis of a null cosmic flux with a significance of 1.6 σ. Even though this significance is not large, the analysis result is consistent with the observation of a cosmic neutrino flux compatible with the one observed in the IceCube data.

Galactic plane diffuse flux search

The ANTARES collaboration carried out a further analysis [85] focused on the search for a high-energy Galactic diffuse neutrino emission, since it could justify the small anisotropies in the excess of cosmic events observed by IceCube. Up to now, the cosmic neutrino flux of Galactic origin is not determined. It should be produced in our Galaxy by the interaction of accelerated cosmic rays with the interstellar medium and its detection will shed light on acceleration features and gas morphology of our Galaxy. In this analysis the "Gamma model" [86], which account for a radially dependent CR diffusion properties, able to explain both the observed local CR features [87–89] and the diffuse Galactic γ ray emission measured by Fermi-LAT [90], H.E.S.S. [91] and Milagro [92], is assumed as reference model to derive the expected diffuse Galactic neutrino emission. The scenario proposed in this model is able to explain the local cosmic ray measurements as well as the high energy γ ray diffuse Galactic emission. The neutrino flux predicted by the "Gamma model" strictly depends on the assumed primary cosmic ray spectrum cut-off. In this search, the possible neutrino contribution is investigated using 9 years of ANTARES data and considering all flavor neutrino interaction. Two different primary cosmic ray spectrum cut-off are assumed, at 5 PeV and 50 PeV.
The search method is based on a likelihood ratio test adapted for a full sky search and

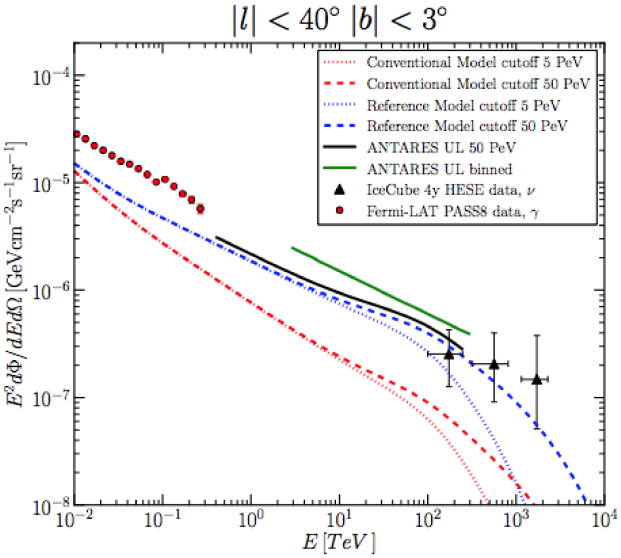

Figure 3.4: In the figure the reference model with a 50 PeV energy cutoff (blue dashed line) and ANTARES upper limit at 90% C.L. on the thee-flavor neutrino flux (solid black line) are reported [85]. The neutrino fluxes according to the reference model with the 5 PeV energy cutoff (blue dotted line), the conventional model with the 50 PeV (red dashed line) and 5 PeV (red dotted line) cutoffs are also shown for all neutrino flavors. The previously published ANTARES upper limit (solid green line) and the four years of HESE reconstructed by IceCube (black triangles) are also presented. These expectations and results concern the inner Galactic plane region (|l| < 40° and |b| <3°).

the maps of signal events are derived from both reference models. Since no excess of events is observed, the analysis result excludes at 90% of confidence level a neutrino flux with a normalization factor which is $1.1 \times \Phi^5_{ref}$ and $1.2 \times \Phi^{50}_{ref}$, being Φ^5_{ref} and Φ^{50}_{ref} the prediction on neutrino flux derived form the "Gamma model" assuming a primary cosmic ray spectrum cut-off at 5 PeV and of 50 PeV respectively. Since neutrinos of all flavors are considered, the larger amount of data leads to an improvement in the sensitivity. The current upper limit is shown in Fig. 3.4. The upper limit on the ANTARES sensitivity for the inner Galactic plane region is shown together with the ANTARES previous result [93], IceCube HESE events [94], the CR conventional scenarios, where a homogeneous CR transport in our Galaxy is assumed, and the reference scenarios for both cut-off conditions. The diffuse gamma-ray spectral energy distribution derived from Fermi-LAT data is also presented [90]. The upper limit provided by this analysis constrains the percentage of cosmic neutrino events of the HESE sample that can originate from diffuse Galactic Cosmic Rays interaction to a maximum of 18%. This result excludes also the possibility that the neutrino flux produced by the Galactic CR interaction with gas can explain the IceCube spectral anomaly.

3.4.2 Search for point-like neutrino source

Since several astrophysical objects have been proposed as production sites of high-energy neutrinos, a search for point-like cosmic neutrino source has been performed by the ANTARES collaboration and presented in [95]. In the point-like source search all flavor neutrino interactions are considered, using the data collected between 2007 and the end of 2015. In fact, in addition to the standard muon track reconstruction, also the shower channel is considered with an improvement of about 23% to all signal events. A generic E^{-2} energy spectrum is used to model cosmic neutrinos flux.
Before performing the analysis a blind procedure, based on pseudo-data sets (pseudo-experiment) of data randomised in time, is followed in order to optimise event selection. The selection criteria have been optimised to minimise the neutrino flux needed for a 5σ discovery of a point-like source in 50% of the pseudo-experiments. Muon events are selected applying cuts on the reconstructed zenith angle, $cos\theta_{tr} >$ -0.1, the estimated angular error, $\beta_{tr} < 1^{\circ}$, and the parameter that describes the quality of the reconstruction $\Lambda >$ -5.2.
Also for shower events only events reconstructed as up-going or coming from close to the horizon, $cos\theta_{sh} >$ -0.1, are considered and with a angular error estimate $\beta_{sh} < 30^{\circ}$. For the shower event the further requirement that the interaction vertex of the event is reconstructed inside or close to the instrumented volume is also required.
Since neutrinos from point-like sources are expected to accumulate in spatial clusters over the atmospheric neutrino background randomly distributed all over the sky, a maximum likelihood ratio approach is used to find these clusters. In the analysis presented here four different approaches are used to search for astrophysical neutrino sources:

1. *Full sky search*: in the first approach the whole sky visible by ANTARES is scanned, using a grid with bins of $1^{\circ} \times 1^{\circ}$ in right ascension and declination, to search for spatial clustering of events with respect to the expected background;

2. *Candidate list search*: in this approach, the directions of a defined list of known astrophysical sources, here considered has candidate neutrino sources, are investigated to look for an excess or, in the case of null observation, to determine an upper limit on their neutrino fluxes;

3. *Galactic Centre region*: in the third case a similar approach to that one considered in the full sky search is used but restricted to a elliptical region centred in the origin of the galactic coordinate system (α, δ) = (266.40°, -28.94°) with a semi-axis of 15° in the direction of the galactic latitude and a semi-axis of 20° in galactic longitude. The reason to focus on this region relies on the number of HESE events observed by IceCube coming form this region;

4. *Sagittarius A**: in the end the location of Sagittarius A* has been tested as extended neutrino source by assuming a Gaussian emission profile with various widths.

For all the approaches no significant excess over background is found. In the full sky search the most signal-like cluster of events is located at (α, δ) = (343.8°,23.5°) with a

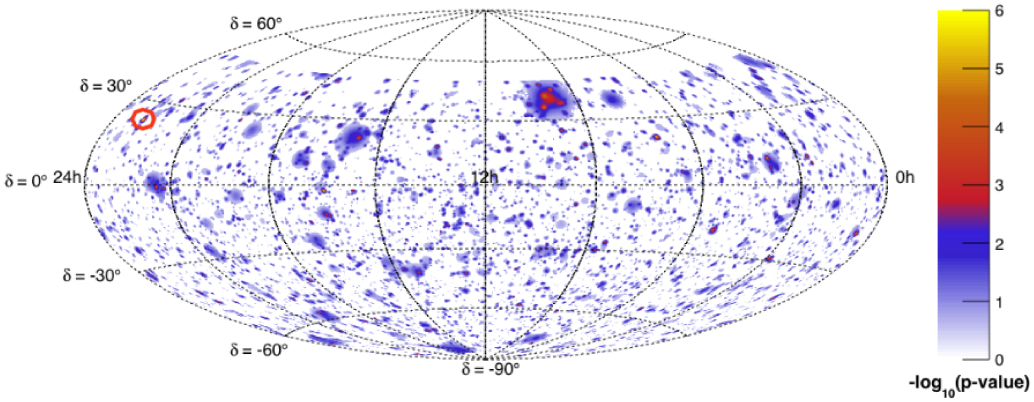

Figure 3.5: Sky map in equatorial coordinates of p-values for a point-like source of the ANTARES visible sky [95]. The most significant cluster found in full sky search is indicated with the red circle.

significance of 1.9σ, as shown in Fig. 3.5. For the candidate list search the neutrino flux sensitivity of the method is about $E^2 d\Phi/dE = 6 \times 10^{-9}$ [GeV cm^2 s]$^{-1}$ for declinations from -90° up to -42°, and below 10^{-8} [GeV cm^2 s]$^{-1}$ for declinations up to 5°, see Fig. 3.6. The directions of 106 source candidates and of 13 muon track events from the IceCube HESE sample are investigated as possible neutrino signal and upper limits on the signal flux are also determined as indicated in Fig. 3.6.

3.4.3 Multimessenger searches

A great deal of effort has been done by the ANTARES Collaboration to share information with other observatories in order to carry on a productive multi-messenger program. This activity involves different telescopes, from radio, optical, X-ray, gamma-rays to cosmic ray and gravitational wave detectors, with the aim to observe transient phenomena through several cosmic messengers. In fact, the transient nature of this phenomena make them difficult to study. Therefore the intrinsically different nature of these cosmic messengers can provide as the same time complementary information on the physics processes involved in these phenomena.
In this multimessenger program the ANTARES telescope is responsible for cosmic neutrino detection. Meanwhile, among all the possible astrophysical sources, transient sources represent a fundamental opportunity for neutrino astronomy thanks to the almost background free search in a well-defined space-time window. Among the activities carried on by the ANTARES Collaboration in the multimessenger context those of particular importance are the real-time follow-up analyses, alert triggering and off-line analyses described below.

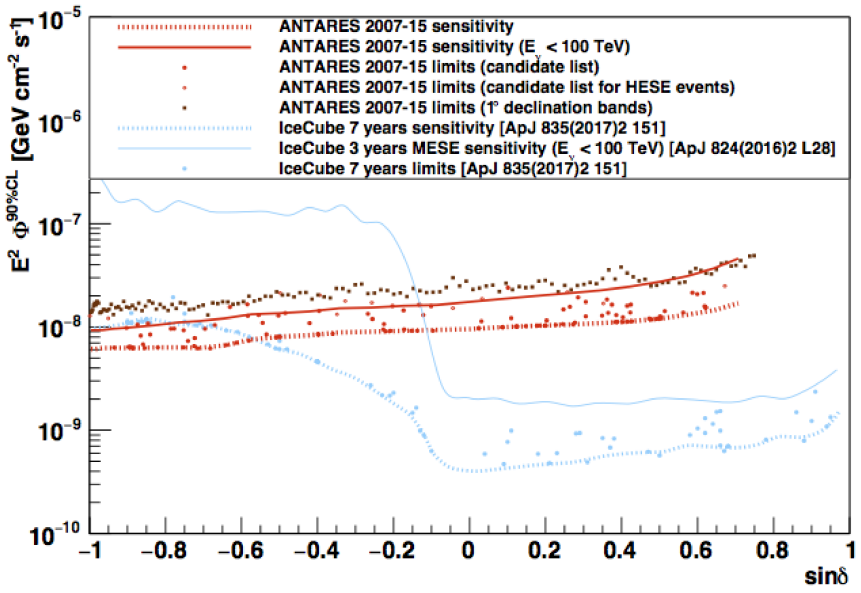

Figure 3.6: Upper limits at a 90 % C.L. on the signal flux from the investigated candidates sources assuming an E^{-2} spectrum (red circles) [95]. The ANTARES sensitivity is indicated by the dashed red line, while the sensitivity of the seven years point-like source analysis by the IceCube is also reported for comparison. The blue dots indicate the upper-limits obtained in this analysis. The sensitivity for neutrino energies under 100 TeV is also shown with a solid red line. The solid blue line indicates the IceCube curve for energies under 100 TeV obtained from the 3 years MESE analysis [96]. The limits of the most significant cluster obtained in bands of 1° in declination are also shown with dark red squares.

Real-time follow-up analyses and alert triggering

Real-time follow-up analyses are performed by the ANTARES Collaboration as a results of the detection of particularly interesting transient events by other observatories, as high-energy neutrino candidates by IceCube, Gamma-Ray Bursts and Gravitational Waves (GW). These on-line analyses, triggered by external alerts, look for the neutrino events or for the neutrino counterpart that these cataclysmic events can exhibit. The main efforts done by the ANTARES Collaboration in the context of real-time follow-up analyses are related to the GW detection. In fact, thanks to the better angular resolution of ANTARES ($\sim 0.4^\circ$ at TeV) compared to the size of the gravitational wave error box (a few hundreds of square degrees on the sky), neutrino detection can also provide important information on the event position.
The high-energy-neutrino follow-up observation of the gravitational wave GW150914, observed by the Advanced LIGO detectors on the 14th September 2015, triggered the first joint analysis performed by the IceCube and the Antares neutrino telescope [97]. In this analysis no neutrino candidates were found in time-space coincidence with the GW event. The detected neutrinos found in a $\pm$ 500 s time window around the GW event by IceCube and Antares were three and zero, respectively. This result is consistent

with the expected atmospheric background and none of the neutrino candidates were directionally coincident with the GW event. The non-detection was used to constrain neutrino emission from the GW event.
The detection of the gravitational wave signal GW170104 [98], originating from the coalescence of two black holes, by the Advanced LIGO detectors on the 4th January 2017 led to an all sky high energy neutrino follow-up search [99] using both the upgoing and the downgoing ANTARES datasets. The analysis looked for ν_μ and $\bar{\nu}_\mu$ track events produced in a time window of $\pm$500 s around the GW signal. The search for a neutrino counterpart within an extended time window of $\pm$ 3 months has been also performed but no neutrino emission associated with the GW170104 event was found in the ANTARES data. The non-detection allowed to set an upper limit on the neutrino emission from the GW170104 event equal to $\sim 1.2\times10^{55}$ erg.
The observation of the GW170817 event, from a binary neutron star inspiral, by the the Advanced LIGO and Advanced Virgo on the 17th August 2017 [100] pushed the second joint analysis performed using the ANTARES, IceCube, and Pierre Auger Observatories data. After the GW event a short gamma-ray burst was also recorded by the Fermi Gamma-ray Burst Monitor (Fermi-GBM) [101–103] and precise location of the event was determined by optical detections of emission following the merger. Also in these case no neutrinos directionally coincident with the GW event were detected within $\pm$500 s window nor in the subsequent 14 days and upper limits on the neutrino fluence were set, as shown in Fig. 3.7. This non-detection is consistent with the expectations from a typical GRB observed off-axis.
In this multimessenger observatory network, also ANTARES can trigger electromagnetic follow-up of interesting neutrino candidates, thanks to the TaToO (Telescopes-ANTARES Target-of- Opportunity) program. In fact, when a neutrino event of potential astrophysical origin is detected, an alert message is generated to trigger robotic optical telescopes (TAROT, MASTER, ZADKO), radio telescopes (MWA), X-ray satellites (Swift-XRT, INTEGRAL), and ground based gamma ray observatories (H.E.S.S., HAWC). Up to now ANTARES has sent more than 300 alerts, but no time-space correlations between detected neutrino events and astrophysical objects has been found.

Off-line analyses

In order to verify the occurrence of hadronic acceleration mechanisms in astrophysical sources, ANTARES performs also off-line analysis to search for neutrino emission of catalogued flaring sources as microquasars, blazars and GRBs. The detection of high energy neutrino in time and space correlation with the flare emission would unambiguously prove the existence of hadronic acceleration mechanisms in these sources. In particular, a recent ANTARES search for neutrino emission during the flares state of 34 Galactic X-ray binaries has been performed [104]. No cosmic neutrino event was detected in time-space correlation with the flare emissions. This result provides the hint that some of the more optimistic models describing hadronic acceleration in these sources can be rejcted at 90% C.L..
A time-correlated analysis with the HESE detected by IceCube is ongoing. In fact two

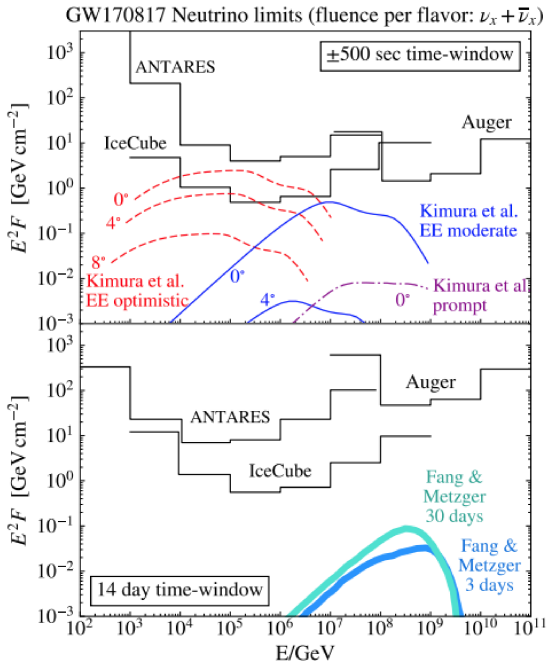

Figure 3.7: Upper limit at 90 % C.L. of ANTARES, IceCube, and Pierre Auger Observatories on the neutrino spectral fluence from GW170817 during a ±500 s window centered on the GW trigger time (top panel), and a 14-day window following the GW trigger (bottom panel) [100]. In the figure the predictions of several model of GRB emission, for different values of the off-axis angle, are also shown.

of the observed HESE occurred 1 day of each other with a p-value of 1.6%. Therefore it could be the signature of the flare emission of an unknown source. In the analysis the ANTARES data has been scanned to look for time and space correlation with 54 IceCube events. Each IceCube event has been treated as a potential transient neutrino source. No ANTARES event was observed in correlation with the selected IceCube HESE, constraining the hypothesis of transient origin of the IceCube events.

3.4.4 Search for neutrinos form TXS 0506+056

After the IceCube observation of a candidate high energy neutrino event [4], IceCube-170922A, detected on the 22th September 2017 at 20:54:30.43 UT and reported on [105], three different analyses have been performed by the ANTARES Collaboration searching for additional neutrinos from the reconstructed event direction. In the first analysis an online follow-up observation of the IceCube alert was performed, the second analysis was focused on the search for point-like neutrino sources using the standard time-integrated method employed by the ANTARES Collaboration, while in the third search the information from the IceCube time-dependent analysis indicating a bursting activity centered on the 13th December 2014 has been used to perform an ANTARES time-dependent analysis.

Since the reported position of the IceCube event was RA = $77.43^{\circ}{}^{+1.30^{\circ}}_{-0.80^{\circ}}$ and $\delta = 5.72^{\circ}{}^{+0.70^{\circ}}_{-0.40^{\circ}}$, corresponding to a direction of 14.2° below the horizon at the location of the ANTARES detector, in the online searches for neutrinos associated to the Extremely High Energy (EHE) track event IceCube-170922A only upgoing event have been considered. The high energy neutrino candidates have been searched in the ANTARES online data stream using a fast algorithm, which selects only upgoing neutrino track candidates [106]. However, no upgoing muon neutrino candidate events have been found within a ±1 h time-window centered on the event time and in a search cone of 3° centered on the IceCube event coordinates. The non detection of neutrino events has been used to set a preliminary constraint on the neutrino fluence as described in [107]. In such a computation a neutrino point source with a power law energy spectrum $dN/dE \propto E^{-\gamma}$ has been assumed. For a flux with a spectral index $\gamma = 2.0$ the 90% C.L. fluence upper limit has been set to 15 GeV cm $^{-2}$ integrated over the energy range [3.3 TeV, 3.4 PeV], while for a flux with $\gamma = 2.5$ the 90% C.L. fluence upper limit has been set to 34 GeV cm^{-2}, integrated in the [450 GeV, 280 TeV] energy range.
After the Fermi-LAT Collaboration announcement [73] that the Blazar TXS 0506+056, located at 6 arcmin from the estimated direction of IC170922A, showed enhanced γ ray emission during the week of the alert (Atel #10791), a time-integrated search for neutrinos from TXS 0506+056 using the ANTARES data has been performed. Since also the MAGIC Collaboration observed this source with a 5σ detection above 100 GeV (ATel #10817), the potential association between IceCube-170922A event and the Blazar TXS 0506+056 let to scrutinize this location of the sky using the ANTARES standard point-source method. In this approach, the directions of a predefined list of 106 candidate neutrino sources, not including TXS 0506+056, have been investigated to search for an excess of events using the ANTARES data collected from January 29, 2007, to December 31, 2015. The neutrino event selection has been optimized following a blinding procedure on pseudo data sets randomised in time before performing the analysis. A maximum likelihood ratio approach has been followed to find clusters of neutrinos from cosmic sources. In the search for cosmic neutrino signal both the shower-like and track-like events have been included and the results have been published in [95]. The Blazar TXS 0506+056 has been added to the list of the 106 already studied sources. A number of signal events equal to $\mu_{sig} = 1.03$ was found as the number of signal events which fits the likelihood signal function for this source, with a pre-trial p-value of 2.6% to be compatible with the background-only hypothesis. Fully calibrated data collected by the ANTARES detector during 2016 and 2017 have been unblinded using the same predefined conditions used for the 2007-2015 period. An analysis limited to the TXS 0506+056 source has been performed considering only this additional data sample and two new tracks within 5° from the TXS 0506+056 position have been found. Considering the full period of data taking the number of fitted signal events, μ_{sig}, remains 1.03 and the associated p-value rose from 2.6% to 3.4%. Using the total livetime of 3136 days, the corresponding 90% C.L. upper limits on the flux normalization factor at 100 TeV, $\Phi^{90\%}_{100\mathrm{TeV}}$, assuming a steady neutrino source and spectral index $\gamma = 2.0$, has been set to 1.6×10^{-18} GeV^{-1} cm^{-2}s^{-1} in the 5%-95% energy range [2 TeV,4 PeV].

For the search for neutrinos in the bursting periods of TXS 0506+056, defined by the two profiles provided by the IceCube Collaboration [4], a time-dependent analysis similar to that one reported in [108] has been performed. In the IceCube time-dependent analysis the first burst period has been modeled by a Gaussian signal, called *Gaussian flare*, centered on MJD 57004 and with standard deviation $\sigma = 55.0$ days. In the ANTARES analysis for this flaring period a $\pm 5\sigma$ wide window has been considered, corresponding to 550 flaring days. For the second flare, referred to as the *Box flare*, a box-shaped flare starting at MJD 56937.81 and ending at MJD 57096.21, corresponding to 158.40 flaring day, has been assumed.
In the ANTARES time-dependent analysis, which account for a power law energy neutrino spectrum with three different spectral indexes ($\gamma = 2.0$, 2.1 and 2.2) for signal events, first the values of selection cuts on the maximum reconstructed neutrino zenith angle, θ, and the quality of reconstructed tracks, Λ, that optimise the Model Rejection Factor (MRF) were defined. After the optimisation, the data were unblinded and the results were compatible with the expectation from the atmospheric background for both the bursting period. In the whole analysed period 10 background events were expected within 2° from the source position, while 13 events have been found in data. None of them was within the two considered flaring periods. From these null results, the 90% C.L. upper limits have been set for the $E^{-2.0}$, $E^{-2.1}$ and $E^{-2.2}$ energy spectrum corresponding to a neutrino flux of $\Phi^{90\%}_{100\text{TeV}} = 4.6$, 4.4 and 4.2×10^{-18} $\text{GeV}^{-1}\text{cm}^{-2}\text{s}^{-1}$ for the Gaussian-shaped period. The corresponding energy range containing the 5-95% of the detectable flux are [2.0 TeV, 3.2 PeV], [1.3 TeV, 1.6 PeV] and [1.0 TeV, 1.0 PeV]. For the Box-shaped period, the flux normalization factors are a factor 3.3 higher.

3.5 The KM3NeT Research infrastructure

The KM3NeT research infrastructure [7] will host two neutrino detectors: the ARCA telescope, optimised to search for high energy neutrino sources in the Universe, and the ORCA telescope, whose main physics goal is the determination of the neutrino mass hierarchy. Two different sites have been chosen to build the telescopes. In the Italian site, at ∼80 km offshore Capo Passero, the ARCA telescope is already under construction at a depth of ∼3500 m, and it will reach a volume of a cubic kilometre. Whereas, the ORCA telescope is located 40 km offshore of Toulon, in the France Site, at a depth of 2500 m.
The two telescopes share almost the same technology, as well as the basic detection elements, but the different scientific goals obliged to develop slightly different detector geometries. Each telescope will consists of a three-dimensional array of optical sensors, the Digital Optical Module (DOM), a pressure resistant glass sphere of 43 cm diameter, containing 31 3" photomultiplier tubes (PMT). The DOMs represent the basic detection elements of the detectors. In fact, they are responsible for the detection of the Cherenkov radiation induced in the medium by relativistic charged particles produced in neutrino interactions. Eighteen DOMs are arranged in a vertical floating string anchored on the sea floor, the Detection Unit (DU) and 115 DUs make one Building Block. This modular

design can be optimised, having blocks with different distances between DOMs and DUs, in order to ensure the best coverage of the different neutrino energy ranges of interest for the ARCA and ORCA detector. The ARCA-DUs are 700 m tall, with an average interspace between consecutive DOMs of 36 m, starting about 80 m from the sea floor. The horizontal distance between DUs is about 90 m. With this configuration the ARCA telescope is sensitive to cosmic neutrinos in the TeV – PeV energy range. Whereas, to reduce the energy threshold of detectable neutrinos necessary for the mass hierarchy determination, the ORCA detector has a much more dense configuration than ARCA. The ORCA-DUs are 200 m tall, housing 18 DOMs with an average distance between them of 9 m, starting about 40 m from the sea floor and with an horizontal inter-distance of about 20 m.
The performances of the ARCA and ORCA telescopes have been widely investigated through MC simulations and presented in [7]. MC simulations allowed to carry out sensitivity studies for both detectors. For the ARCA telescope the sensitivity to a diffuse neutrino flux as well as to the point-like neutrino sources have been deeply investigated, proving the ARCA capability to detect the diffuse neutrino flux detected by IceCube in few years and to constrain the hadronic scenario in galactic gamma rays sources. Sensitivity studies for the determination of the neutrino mass hierarchy with the ORCA detector have been also performed, demonstrating the possibility to discriminate between the normal and inverse mass hierarchy in few years of data acquisition.
The Phase-1 of the KM3NeT research infrastructure realisation is currently ongoing. With the Phase-1 the KM3NeT Collaboration is proceeding with the deployment of 24 DUs in the Italian site, with a corresponding volume of about 0.1 km^3, and 7 DUs in the France site. The first two ARCA-DUs were deployed in December 2015 and in May 2016. Even if in a minimal configuration, the ARCA detector has taken data continuously from December 2015 up to April 2017. The analyses performed with the reconstructed data (see sec. 7.5), as well as the data-MC comparison, proved the reliability of the KM3NeT infrastructure and technology. In the KM3NeT-Phase 2.0 both telescopes will reach their final configurations, two Building Blocks for ARCA and one Building Block for ORCA, as shown in Fig. 3.8.

3.6 Installation sites

The search for the suitable site to build underwater neutrino telescopes was one of the primary goals of the KM3NeT Collaboration. Careful studies have been performed in order to identify the best installation sites. The criteria considered for the choice of the telescopes locations mainly involved the properties of the sites themselves, as the deep sea water optical properties (absorption and diffusion), biological activity, optical background, water currents, sedimentation and seabed nature. Thanks to its location and deep sea water properties, the Mediterranean Sea turns out to be an excellent place all over the world able to host a neutrino telescope. Using up-going muon track events, the sky coverage of a neutrino telescope located in the Mediterranean Sea is complementary

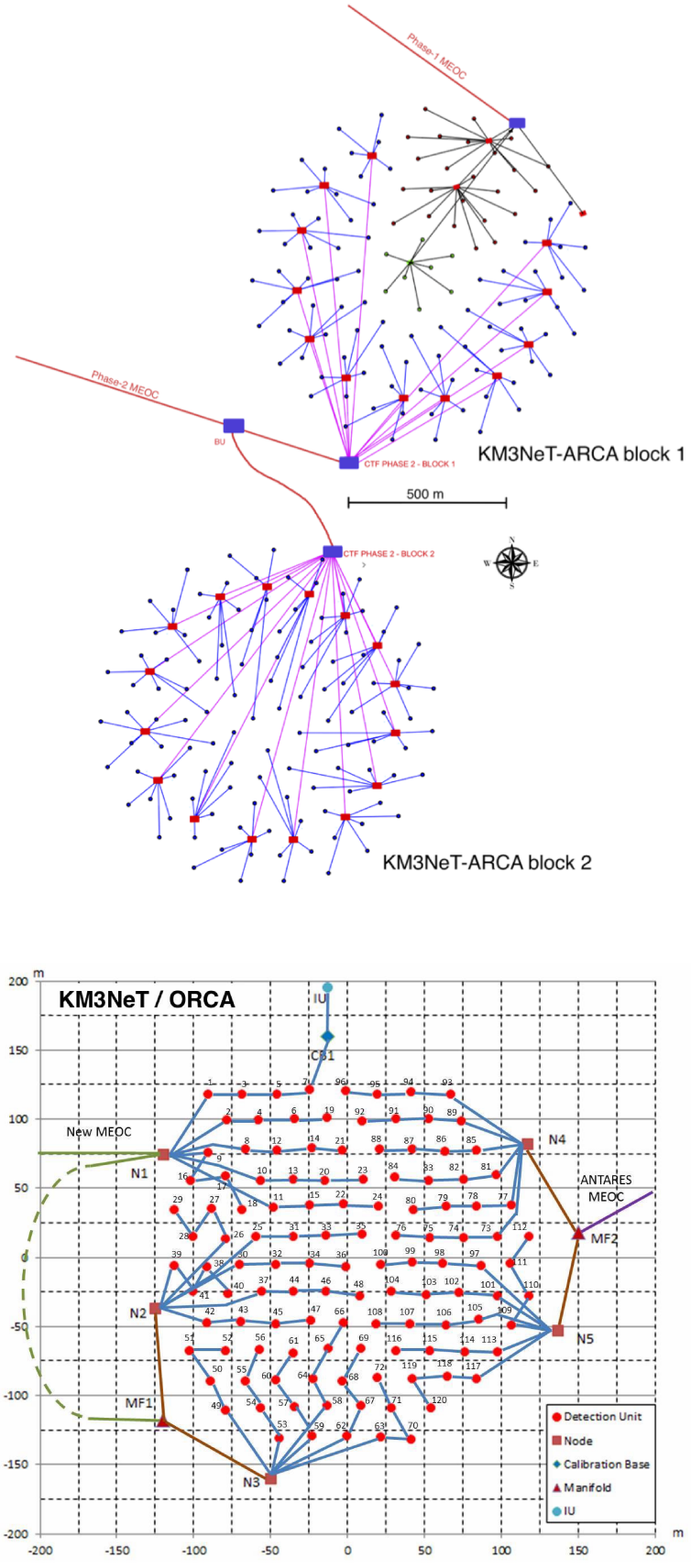

Figure 3.8: ARCA (top) 2 building blocks and ORCA (bottom) 1 building block layouts [7].

to the field of view of IceCube, as shown in Fig. 3.9, ensuring also a direct observation of the Galactic Plane where many sources of interest for the neutrino astronomy are located.

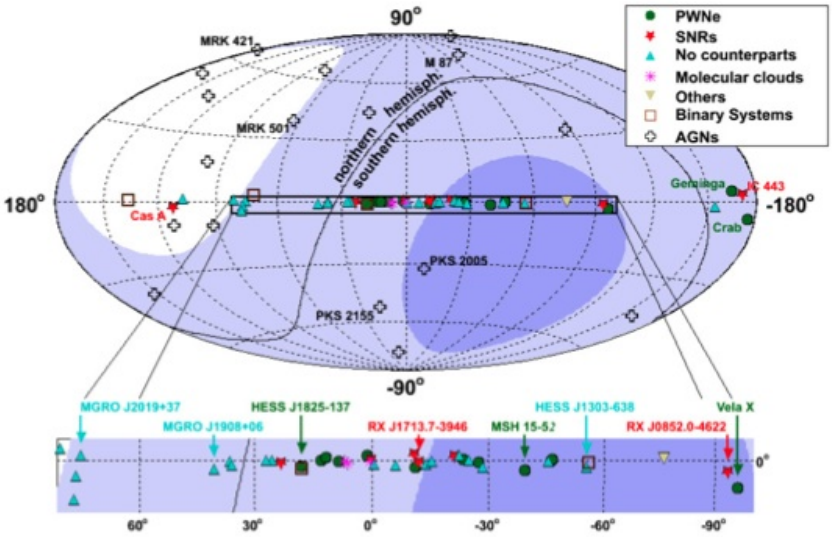

Figure 3.9: Sky coverage in Galactic coordinates for a detector located in the Mediterranean Sea [109]. The shading indicates the visibility for a detector in the Mediterranean with 2π downward coverage; dark (light) areas are visible at least 75% (25%) of the time. The locations of recently observed sources of high energy gamma-rays are also indicated.

In the Mediterranean Sea tree different locations have been identified as reasonable installation site: 40 km offshore of Toulon, France, at a depth of 2500 m; 80 km offshore of Capo Passero, Italy, at a depth of 3500 m and 20 km offshore of Pylos, Greece, at depths of 4500-5200 m, see Fig. 3.10.
Great attention has been focused on the Capo Passero site due to the excellent light transmission properties. These properties have been widely studied, proving that the deep water has an absorption length almost equal to pure sea water at all wavelength, with no seasonal dependence of the optical parameters. The transmission lengths for Cherenkov photons is about 70 m and the results of the measurements carried out in different seasons are shown in Fig. 3.11.

3.7 Optical Modules and photomultipliers

The DOM is the basic detection element of the KM3NeT neutrino telescope. The design of the multi-PMT DOM, chosen for the ARCA and ORCA detectors, has several advantages with respect to traditional optical modules with single large PMTs since

1. the total photocathode area in a single sphere is maximized;

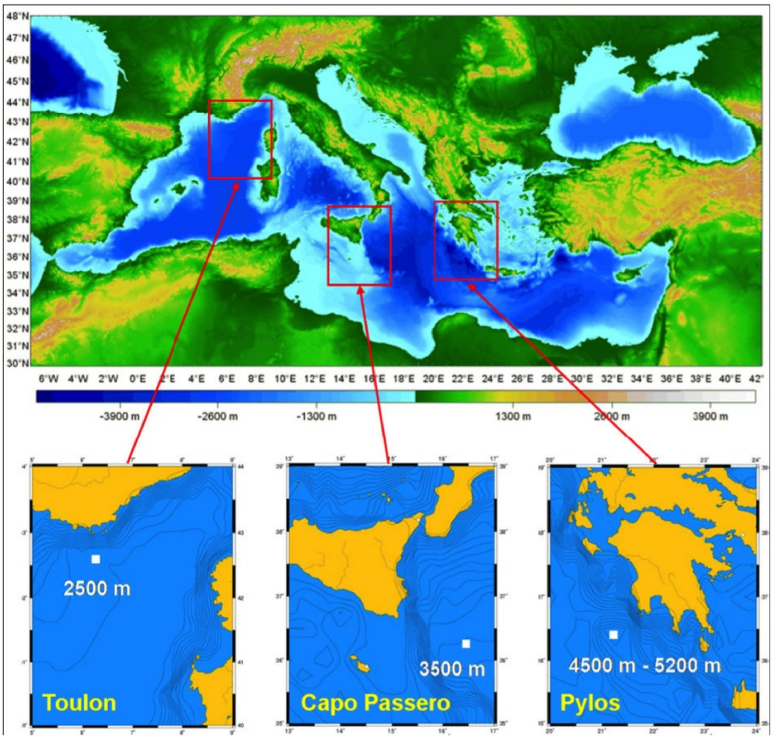

Figure 3.10: Selected installation sites of the KM3NeT neutrino telescope in the Mediterranean Sea [110].

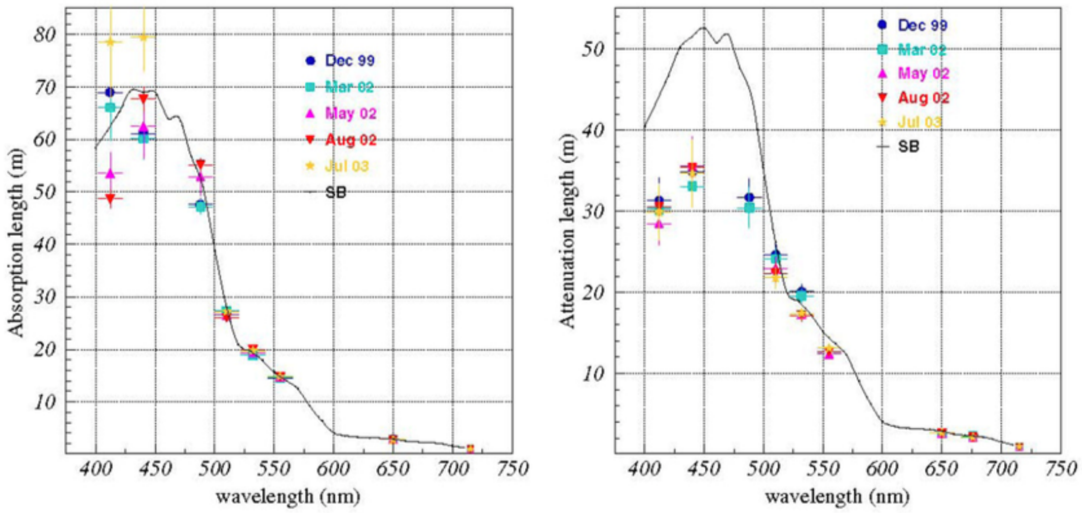

Figure 3.11: Absorption length (left panel) and attenuation length (right panel) measured at the Capo Passero site at four seasons. The values for optically clean salt water (black lines) are also reported [111].

2. small photomultipliers are less sensitive to the Earths magnetic field and therefore do not require to be shielded;

3. the PMTs have a small integrated anode charge and are therefore less subject to ageing;

4. due to the segmentation of the detection area in the DOM, the identification of more than one photon arriving at the DOM can be done with extremely high efficiency and purity.

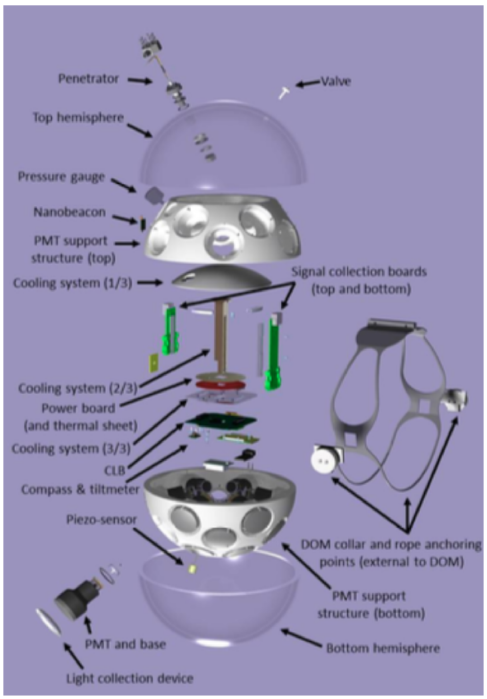

Figure 3.12: DOM internal structure and its main components [7].

An expansion of the DOM internal structure and its main components is shown in Fig. 3.12. Inside the DOMs, the PMTs are arranged in 5 rings plus a single PMT at the bottom pointing vertically down. In each ring, the 6 PMTs are spaced at 60° in azimuth and successive rings are staggered by 30°. There are 19 PMTs in the lower hemisphere and 12 PMTs in the upper hemisphere. Optical gel fills the cavity between the PMTs and the glass, in order to guarantee optical coupling and assure structure stability.
Each PMT has an individual high-voltage supply integrated on its base, with integrated amplification and adjustable discrimination. The PMTs collect the Cherenkov photons and convert them into electronic signals, the so-called *hits*. An event is then represented by the sample of detected *hits* related to Cherenkov radiation. One of the main parameter that determine the accuracy of the event reconstruction is the PMT timing precision. The *hit* time is defined as the time at which the PMT pulse overcomes a threshold of

0.3 p.e. The system provides nanosecond precision on the arrival time of single photons. The charge estimate of the electronic signals, generated by the detected *hits*, is based on the Time over Threshold (ToT) values of the PMT pulses. The ToT is the time during which the PMT pulse remains above the 0.3 p.e. threshold. The accuracy of this estimation affects the event energy resolution. Dark count rate and pre/after-pulses can also affect the telescope performance. The arrival time and the ToT are recorded by a local Time-to-Digital Converter embedded in the Field Programmable Gate Array (FPGA), located in the DOM Central Logic Board (CLB).

Each optical module incorporates also three further sensors:

- a LED emitter (nano-beacon pulser) located inside the DOM working in pair with a laser located in the DU base. The LED nano-beacons are used for the Inter-DOM time calibration and measurement of the water optical parameters;
- a compass and tiltmeter for orientation determination;
- an acoustic piezo-sensor attached to the inner surface of the glass sphere for the acoustic position.

The PMTs are calibrated onshore before the deployment. In April 2013 the first prototype of a DOM (Pre-Production Model DOM, PPM-DOM) was deployed at a depth of 2500 m in the ANTARES site in order to validate the DOM concept and technology, as described in [112]. The photon counting capability and the directionality provided by the multi-PMTs DOM design enable each DOM to identify muons and to be sensitive to their arrival directions, as shown in Fig. 3.13 .
In Fig. 3.13 A the rate of coincidence levels is shown. For the PPM-DOM the coincidence level was defined as the number of PMTs having a detected hit within a 20 ns time window. The event rate due to the decay of ^{40}K is typically homogeneous over the full detector and it is expected that involves only local coincidences of few PMTs. For coincident level lower than six, the analysis of data shows that the measured rate is in agreement with the event rate given by the simulation of the ^{40}K decays. Above the coincidence level of seven, the signals from atmospheric muons dominate and also in this case a good agreement between data and simulated muons is achieved. Since a very good agreement between data and simulated atmospheric muons was found, coincidences level higher than 7 allow a single DOM to unambiguously identify atmospheric muons.
In Fig. 3.13 B the number of hits detected by each PMT is shown as a function of their position, corresponding to the different zenith angles of the rings in the DOM. To select a pure muon sample, a cut at a coincidence level larger than seven was applied. Since atmospheric muons come from above, the PMT rate increase with the decrease of the PMT zenith angle. Also in this case a good agreement between data and atmospheric muon simulation was obtained, proving that the DOM is sensitive to hits arrival directions.

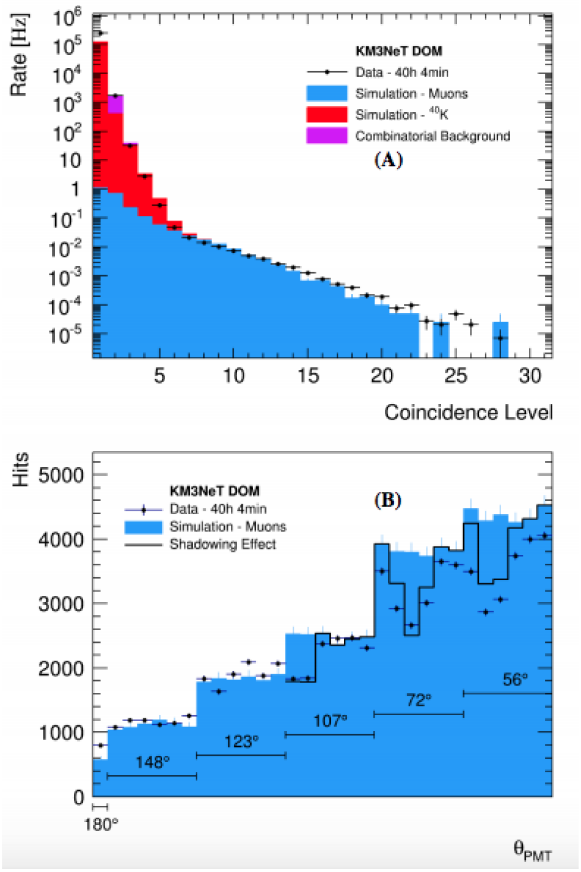

Figure 3.13: In (A) the rate of coincidence level is shown. Black dots correspond to data while blue, red and purple histograms represent simulations of atmospheric muons, ^{40}K and accidental coincidences respectively. In (B) the number of hits as a function of the PMT zenith position, for coincidence levels above seven, is shown. One PMT is looking downward at 180° while the others are grouped in five different angles according to their distribution on PMT rings. The black dots are data, the blue histogram is simulation of atmospheric muons and the black histogram shows the calculated effect of the shadowing by the ANTARES electronics cylinder [112].

3.8 Detection Units

The KM3NeT DOMs are lodged in vertical structures, the detection units, anchored to the seafloor and kept vertically by a buoyancy at their top. The detection unit is kept together by two Dyneema ropes, as shown in Fig. 3.14. An electro-optical backbone provides connections for each DOM, two conductors proving power supply and two optical fibers allow the communication to shore. Through the ropes, cables provide power and slow-control communication to the detector from a shore station.
A new technique has been developed for the deployment of the detection units, which simplify the operations during the sea campaign. At first, the detection unit is rolled in a sphere with 2 m diameter, the launcher vehicle. During the sea operation, the launcher

Figure 3.14: The DOM fixation on the two parallel DU-Dyneema ropes [7].

vehicle is dropped off to the seabed from a surface vessel. When the launcher vehicle reaches the seabed, the buoy is released allowing for the unfurling of the detection unit, as shown in Fig. 3.15. A further advantage, derived by the deployment of the detection unit in this compact arrangement, is the enhancement of the number of detection units that can be deployed during each sea campaign.

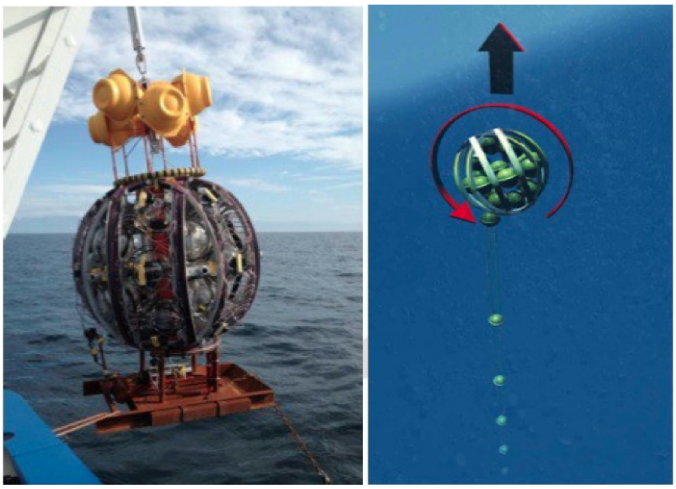

Figure 3.15: Detection unit and launcher vehicle of KM3NeT telescope [7].

In order to take under control the position of the telescope's mechanical structures, both during the deployment and the operation phases, an Acoustic Positioning System (APS) is used. A deep-sea APS is composed of a Long Baseline (LBL) of acoustic receivers,

anchored on the seabed in known positions, and an array of acoustic receivers on board of the DOMs. Therefore, during the deployment the DOM position is evaluated by measuring the time difference between the emission time from acoustic receivers at known position and the arrival time on receivers at unknown position.
In order to validate the DU concept and technology, but also the unfurling procedure, a prototype Detection Unit (Pre-Production Model DU, PPM-DU) [113] with three DOMs was deployed at the Capo Passero site in May 2014, providing more than one year of data taking until its decommissioning in July 2015. The PPM-DU implements the mechanical structure, the electro-optical connections and the data transmission system developed for the final KM3NeT-DU design.
The PPM-DU allowed to validate the procedures for the time calibration between DOMs, the *inter-DOM* calibration (see sec. 3.9). This procedure proved that a synchronisation at a nanosecond level between DOMs is obtained. The inter-DOM calibration can easily be extended to a detector with several thousands of optical modules, ensuring the nanosecond accuracy in the time calibration required for an accurate reconstruction of the muon trajectories.

3.9 Positioning system and Data Calibration

As already discussed in sec. 3.2, for a neutrino telescope the knowledge of the DOM positions, with an accuracy of about 10 cm, and the relative time offsets between the PMTs measured at the level of about 1 ns, are essential prerequisites to achieve an angular resolution of a few tenths of a degree in the energy range between 100 TeV and 10 PeV. Also in the KM3NeT framework, an acoustic positioning system [114], which allows to keep under control the detector configuration altered by sea currents, and a time calibration procedure [113], though which the time offset among all the detector components is measured, ensure to achieve optimal performance in term of angular resolution.
Being anchored to the sea bed, the KM3NeT DUs modify their vertical position under the effect of the sea currents. Therefore their alignment must be monitored and determined during the whole data acquisition. The combination of a long baseline (LBL) of acoustic transmitters (beacons), placed on the sea bed in known positions and an array of acoustic receivers (hydrophones and acoustic piezo-sensors), connected to the mechanical structures of the telescope, constitute the KM3NeT Acoustic Positioning System (APS). On shore, the positions of the acoustic receivers are calculated though the emission of acoustic signals, easily recognised by the acoustic receivers of the telescope, measuring the travel time of the signal emitted by the LBL beacons to the acoustic receivers, the so-called Time of Flight (ToF). The acoustic signal repetition rate could be varied according to the intensity of sea current. The APS, in combination with compass and tilt data should provide the measurement of the DOM position in the deep sea with an accuracy of about 10 cm.
Since the reconstruction of the particle trajectories requires a nanosecond accuracy on the measured time of Cherenkov photons to ensure good angular resolution, in addiction to the acoustic positioning system, a time calibration procedure is necessary. The time

calibration procedure allows to know the relative time offset among all the detector components with sub-nanosecond accuracy. In order to reach this goal tree different time calibrations are performed:

- the *intra*-DOM calibration, responsible for the determination of the time latency among the PMTs inside the same DOM. It is mainly affected by the PMT transit time spread;
- the *inter*-DOM calibration, which depends on the cable lengths and looks for the time offset between the DOMs of the same DU;
- the *inter*-DU calibration, through which the time offset between DUs is determined.

The efficiency and nanosecond precision achievable with both the intra-DOM and inter-DOM time calibrations have been already proved with the PPM-DOM and PPM-DU data analyses, being expandable to a detector with several thousands of optical modules. The intra-DOM calibration is based on the measurement of coincident PMT signals produced in the sea water by the ^{40}K decay. In fact, a ^{40}K single decay occurring in the vicinity of the DOM can produce a genuine coincidence between different PMTs inside the same DOM, which can be exploited for the DOM time calibration. Precisely, the distributions of the time differences between signals detected in different PMTs in the same DOM are studied as a function of the angular separation of the involved PMTs. The distribution of hit time differences between all possible combinations of PMT pairs is expected to follow a Gaussian shape and, for each DOM with $N = 31$ PMTs, a total of $N(N-1)/2$ distributions are considered, as shown in Fig. 3.16 for the PPM-DU DOM1. In Fig. 3.16 (A), the number of PMT pairs is ordered according to their angular separation. The peak due to genuine coincidence between different PMTs decreases as the angular separation increases, according to the limited field of view of each PMT. An example of time differences between two adjacent PMTs of the same DOM is given in Fig. 3.16 (B). The rate of coincidences was obtained by subtracting the flat combinatorial background due to uncorrelated hits on the two PMTs. Since all these distributions are well fitted by a Gaussian function, the time offsets, detection efficiencies and intrinsic time-spreads of all the PMTs are related to the mean values, heights and widths of the Gaussian peaks. The angular dependence for all PMT pairs can be fitted by an exponential function and a χ^2 minimisation procedure is applied to obtain simultaneously the relative time offsets, the detection efficiencies and the intrinsic time-spreads of all PMTs in a DOM. Typically, a full width at half maximum (FWHM) of 7–10 ns is found for all different PMT pairs, mostly reflecting the intrinsic PMT transit time spread of up to 5 ns at FWHM.
The Inter-DOM calibration, which measures the time offsets between the different optical modules in the same DU, is performed using LED nanobeacons mounted on the DOM itself. In fact a LED nanobeacon is abled to illuminate surrounding DOMs up to a distance of approximately 400 m. The time differences between a pair of DOMs is obtained during runs in which the LED nanobeacon of the lowest DOM is operating. The distribution of time differences of coincident hits on the DOM with the nanobeacon and in the lighted

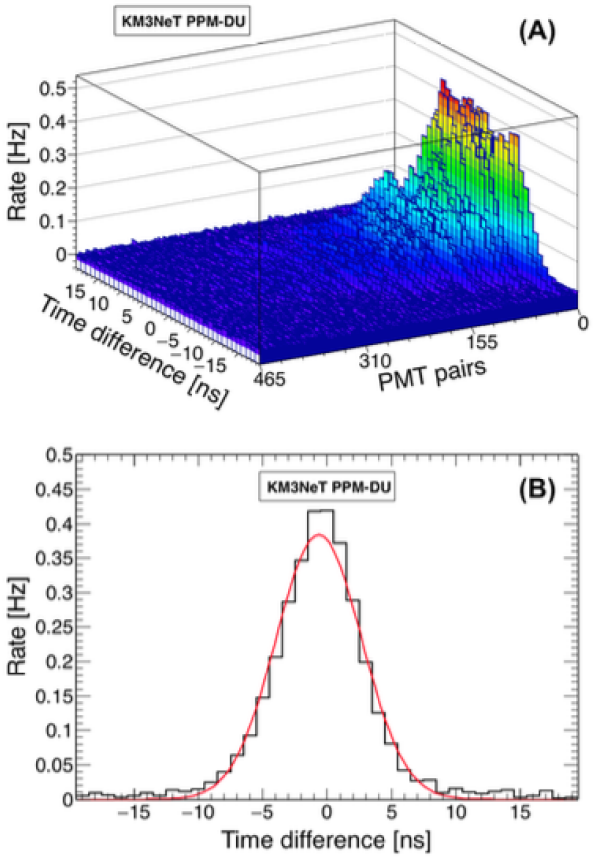

Figure 3.16: (A) Distribution of time differences between the hit times for all PMT pairs in PPM-DU DOM 1 for one physics run. The PMT pairs are ordered according to the angular distance between PMTs. (B) For the same DOM, the distribution of time differences between the hit times of two adjacent PMTs for one physics run is shown. The Gaussian function, represented by the red line, is the result of the simultaneous fit. The baseline due to combinatorial background has been subtracted from the data [113].

one, the DOM to be calibrated, are corrected for the travel time of light in the sea water. The calibrated time obtained with this procedure is stable within few nanoseconds. The calibration using nanobeacons has been also cross checked by an alternative calibration procedure, which account for the signal due to atmospheric muons. An agreement within 2 ns between the two calibration procedures was found. Since the beacons signal emitted at the bottom of the DU can be detected by the lowest DOM in several neighbouring DUs, the laser beacons are also used to perform the inter-DU calibration.

3.10 Trigger and Data Acquisition System

The KM3NeT Trigger and Data Acquisition System (TriDAS) [115] is the ensemble of software and computing infrastructure responsible for the acquisition and triggering of

all the collected data. The modular design of the KM3NeT telescope allows for a progressive detector implementation and data taking. The same scalable design is used for the TriDAS, being able to handle an increasing data rate and implement an efficient data filtering.
The main off-shore data streams are produced by the 31 3" PMTs and piezo-electric acoustic sensor encompassed in each DOM. They represent the optical and acoustic data streams respectively. The readout electronics on board of each DOM, named CLB, digitise the signals from the PMTs, the L0 hits, and collects them into optical data frames. Precisely, a frame collects the amount of data detected by one DOM within a time window of 100 ms. For each *hit* the start time and the ToT are recorded. Acoustic signals from the piezo-electric sensor are sampled, at a constant frequency and with a proper resolution, and assembled in an acoustic data frame. Once a data frame is completed, the DOM sends it to shore using a UDP/IP protocol.
On-shore, the first data processing stage is performed by the DataQueue (DQ), which collects unfiltered data and distributes them to the computing infrastructures dedicated to the on-line analysis and trigger, named DataFilters (DFs). For each data stream a dedicated DF exists, the so-called AcousticDataFilter (aDF) and opticalDataFilter (oDF). The DQ is in charge of the collection of data coming from a subset of DOMs of the detector. In particular, for the optical data stream the oDF receives from all DQs the data belonging to a precise time interval called timeslice (TS). The duration of a TS is fixed, typically 100 ms. The time interval is identified by the TimeStamp, which is the UTC time, in nanoseconds, of the beginning of the timeslice. This strategy enables the oDF to have a complete snapshot of the status of the whole detector limited to the TS duration. The oDF discriminates the physics events from the background through two trigger levels. The first trigger level, the Level-1 (L1), triggers a couple or a sample of hits in the same DOM detected by separate PMTs in a time window of 25 ns (L1 hit). The second trigger level, Level-2 (L2), looks for a physics events due to particles passing in the vicinity of the detector. L2 trigger involves all L1 hits detected in a time window smaller than 330 ns. After the hit selection two online trigger algorithms, called JTrigger3DShower and JTrigger3DMuon, are used to look for track-like or shower-like events. Then, the triggered data, coming out from the oDFs, are sent to the DataWriter (DW) that collects them on permanent storage as ROOT files. The acoustic data are handled differently with respect to the optical case. Since the aim of the aDF is to provide online reconstruction of the Time Of Arrival (TOA) of the acoustic signals emitted by the acoustic positioning system, the aDF receives all data from a single DQ continuously to ensure a complete data time flow from a subset of the acoustic sensors. The output of all the aDFs is collected by the DataBaseWriter (DBW) and written to a database.
In order to steer the detector and take under control the whole data taking, an user interface is used, the ControlUnit (CU). The CU has the aim of coordinating the TriDAS and operating the DOMs through a dedicated SlowControl (SC) protocol.
All the TriDAS components are connected through a network whose topology consists mainly of 3 subnetworks: the raw data, the managed data and the filtered data network, as illustratd in Fig. 3.17. The raw data network aims to connect the off-shore detector el-

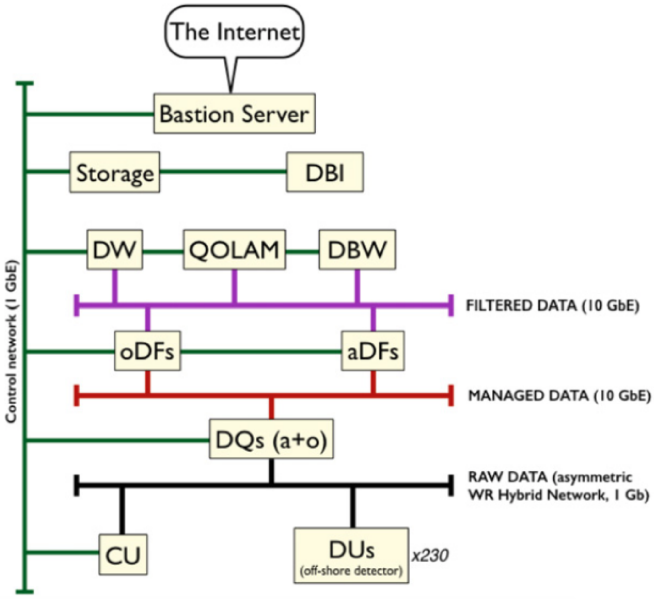

Figure 3.17: Sketch of the TriDAS network topology of the KM3NeT detector and shore-station infrastructure [115].

ements (DOMs and DU bases) with the on shore computers dedicated to the aggregation and distribution of data, the DQ and the CU. It uses a White Rabbit [116] asymmetric Ethernet-based network for data transfer, which also provides sub-nanosecond time synchronisation. The asymmetry comes from the topology of the optical links between the underwater detector elements and the on-shore station. Each DOM has an unidirectional uplink to reach the on-shore station, through which sends the acquired data and replies to slow control commands. On the other side, the on-shore station has a unique unidirectional downlink to communicate with all the DOMs. This optical link is called the Broadcast and it is shared by all DOMs. As last steps, the Managed data network connects the DQ with the DF infrastructures, while the Filtered data network is in charge of the transportation of post trigger data. A Control network allows the connection of all the shore-station computing elements with the CU and provides access to the Internet through a Bastion Server, which protects the internal networks.

3.11 Post triggered data format

According to the Jpp-ROOT format, post triggered optical data are written in ROOT files using the Jpp classes and methods [117]. A ROOT file encloses the data detected in a predefined interval of time, which represents a physics run. In the KM3NeT framework

a 6 hours interval of time is defined as run. Each data file has the following data types

- JDAQSummaryslice
- JDAQtimeslice
- JDAQEvent

and each type consists of a JDAQPreamble, a relevant Header and data, usually stored in vectors. All these type of data are created by the DF and store different information. In particular, the JDAQSummaryslice collects the information about the average rate of L0 hits detected by every PMT over a frame and several status flags indicating further important information about the data acquisition. Among such flags the UDP status and the High Rate Veto (HRV) are the most important. The first one allows to extract information about the data transmission from the off-shore detector to the TriDAS. The latter indicates the status of a safety mechanism which protects the DAQ system from having to process too many hits at the same time. It is activated when the number of L0 hits on a PMT exceeds 2000 in a frame, corresponding to a PMT rate of 20kHz. Subsequent hits are then no longer processed for the duration of the vetoed frame. In the JDAQtimeslice the identifier of detected L1 hit, the hit time, PMT identifier and ToT are stored. In the end, the JDAQEvent data type is dedicated to store the information about the triggered events or $L2$ hits, such as the hits satisfying the trigger conditions, the type of satisfied trigger(s) condition, the timestamp and timeslice identifier of the timeslice that contain the event.

3.12 KM3NeT sensitivity studies

In addiction to the main scientific goals aimed at identifying astrophysical sources of high energy neutrinos and determine the neutrino mass hierarchy, both ARCA and ORCA detectors will offer a wide spectrum of further physics opportunities. ARCA will allow to investigate the field of cosmic ray physics, particle physics with atmospheric muons and neutrinos, dark matter and perform multimessenger studies, while ORCA can allow to detect MeV neutrinos from SNs.
The performance of the ARCA and ORCA detectors estimated by means of multivariate analyses are presented in [7]. In this section an update of the results presented in [7] is reported.

3.12.1 ARCA sensitivity studies to cosmic neutrino sources

The studies about the ARCA sensitivity to diffuse fluxes and point-like sources presented in this section take into account neutrinos and antineutrinos of all flavors (ν_μ, ν_e, and ν_τ) in equal proportions and their CC and NC interactions. Also in this case the sensitivity studies have been performed using multivariate analyses, based on the Boosted Decision Tree algorithm (BDT) [118], and unbinned maximum-likelihood method.

ARCA detection capability to a diffuse flux of cosmic neutrinos

The detection and the investigation of the diffuse flux of cosmic origin observed by IceCube is one of the main physics goals of the ARCA telescope. In this section the main results on the search for a diffuse flux of cosmic neutrinos originating from the whole sky and from a selected region covering the central part of the Galactic Plane reported in [119] are presented.
One of the most promising potential source of a diffuse cosmic neutrino flux is the Galactic Plane (GP). Neutrinos are expected to be produced in the interactions of the galactic cosmic rays with the interstellar medium and radiation fields, with a significant excess respect to the expected extragalactic background. The observation of diffuse TeV γ-ray emission from the Galactic Plane [91, 92], which is expected to derive from the same hadronic processes that would produce high-energy neutrinos, strongly supports this hypothesis.
For the search of a neutrino flux from the Galactic Plane, a region encompassed by $|l| < 30°$ and $|b| < 4°$ in galactic coordinates is considered. The neutrino signal from this region has been computed according to the KRA_γ model of [120], assuming a 50 PeV cutoff for CR primaries. In order to evaluate the ARCA sensitivity to diffuse neutrino fluxes detailed Monte Carlo simulations of have been performed. The sensitivity studies presented here are based on a maximum-likelihood method applied to the event sample resulting from an event preselection, as described in [119], and the results are shown in Fig. 3.18. These results indicates that the sensitivity of ARCA will be enough to study this flux within less than a year of data taking with the complete detector, and a 5σ discovery of such a flux can be obtained in 4 years of operation.
For the search of a diffuse flux of cosmic neutrinos originating from the whole sky, the one flavour cosmic flux has been parameterised considering two different hypothesis

$$\Phi_\nu(E_\nu) = 1.2 \times 10^{-8} \left(\frac{E_\nu}{1\text{GeV}}\right)^{-2} \cdot e^{\left(-\sqrt{\frac{E_\nu}{3\text{PeV}}}\right)} \ [\text{GeVcm}^2\text{s sr}]^{-1} \tag{3.1}$$

$$\Phi_\nu(E_\nu) = 4.11 \times 10^{-6} \left(\frac{E_\nu}{1\text{GeV}}\right)^{-2.46} \ [\text{GeVcm}^2\text{s sr}]^{-1} \tag{3.2}$$

The sensitivity on the search has been estimated following the same procedure used for the galactic plane search but considering only the track channel. The results are reported in Fig. 3.19. As can be seen, the discovery at 5σ can be reached in about one year for a flux with a spectrum $\propto E^{-2}$ and a cutoff at 3 PeV, while for a softer spectrum $\propto E^{-2.5}$ in less than one year.

Point-like neutrino sources

Due to its good angular resolution, KM3NeT/ARCA will be a very promising instrument for the detection of point-like neutrino sources. In particular, its location in the Northern

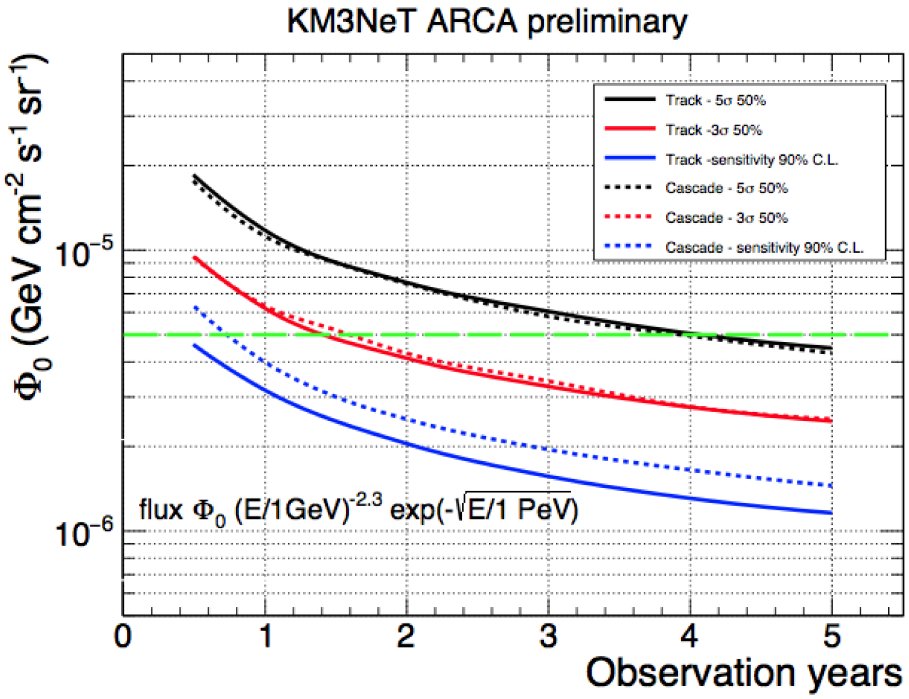

Figure 3.18: In figure the ARCA discovery fluxes and sensitivity as a function of the observation time for the Galactic Plane region ($|l| < 30°$ and $|b| < 4°$) are presented [119]. Both the cascade (dashed lines) and track channels (full lines) are reported. The dashed green line corresponds to the normalization factor of the one-flavor neutrino flux from the Galactic Plane.

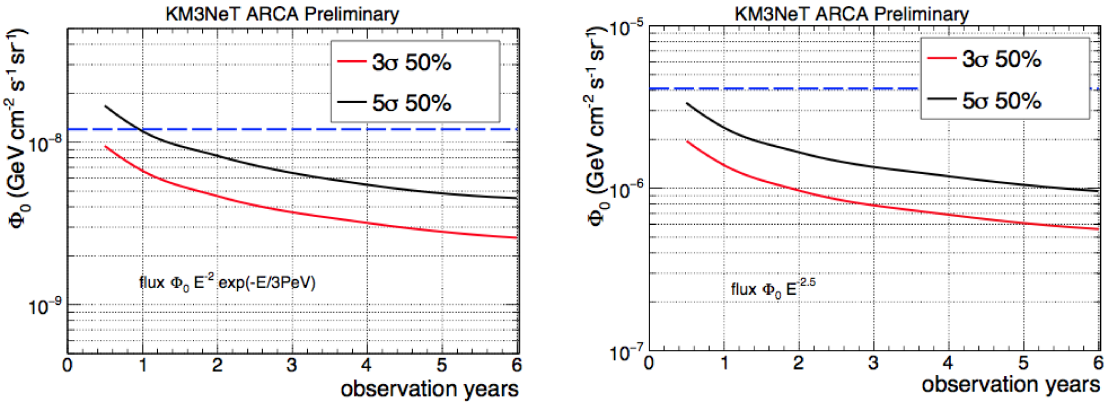

Figure 3.19: ARCA discovery fluxes as a function of the observation years for the track channels for the all-sky analysis for the flux of Eq. 3.1 (left) and Eq. 3.1 (right) [119]. The dashed blue lines represent the normalization factors of Eq. 3.1 and Eq. 3.1.

Hemisphere will allow to study most of the Galactic sources, as well as extragalactic one, using up-going muon track events. The sensitivity of the ARCA detector to point-like

sources reported here refers to preliminary results of:

- Neutrino emission by the SNR RXJ1713 and the Vela Junior, which are at present the Galactic γ-ray sources exhibiting the most intense high-energy emission [121, 122]. For these sources the zenith position, angular extension, and neutrino flux parameterisation are extracted from the measured high-energy γ ray spectra. In both cases, the expected neutrino spectra have been evaluated from the spectrum under the hypothesis of a transparent source and 100% hadronic emission.
- Sources without significant angular extension and a E^{-2} energy neutrino spectrum.

In order to evaluate the ARCA sensitivity and discovery potential to a neutrino emission from the these sources, detailed Monte Carlo simulation have been performed. For the sensitivity studies both track and shower events have been considered and specific event reconstruction algorithms have been applied to each event class.
An event selection, based on cuts on quality parameters and on a multivariate analysis which uses random decision forest [123], has been performed to discriminate signal from background events. Finally the sensitivity studies have been carried out through an unbinned likelihood method.
To study the ARCA sensitivity to the SNR RX J1713.7-3946, a homogeneous emission from a circular region around the measured source declination with a radial extension of 0.6° has been assumed. The neutrino flux has been parameterised following [124] as

$$\frac{d\Phi}{dE} = 0.89 \times 10^{-11} \left(\frac{E_\nu}{\text{TeV}}\right)^{-2.06} \cdot \exp\left(-\frac{E_\nu}{8.04\text{TeV}}\right) \quad [\text{TeVcm}^2\text{s sr}]^{-1} \tag{3.3}$$

While for the Vela Junior a radial extension of 1° has been assumed and the neutrino flux has been parameterised as

$$\frac{d\Phi}{dE} = 1.30 \times 10^{-11} \left(\frac{E_\nu}{\text{TeV}}\right)^{-1.87} \cdot \exp\left(-\frac{E_\nu}{4.5\text{TeV}}\right) \quad [\text{TeVcm}^2\text{s sr}]^{-1} \tag{3.4}$$

The results are shown in Fig. 3.20. The preliminary results for the Galactic Centre and for two different neutrino flux parametrisation of the galactic source HESS J1614-518 are also reported. The fluxes reported in Fig. 3.20 have been divided for the flux expectation Φ_ν (given by Eq. 3.3 and Eq. 3.4 for the RX J1713.7-3946 and Vela Junior respectively), which correspond to a purely hadronic scenario. As shown in Fig. 3.20, the average observation time needed for a 3σ detection is given in terms of the ratio $\Phi_{3\sigma}/\Phi_\nu$. These results suggests that the sensitivity necessary to exclude the predicted fluxes at 90% CL is reached for all the sources after about 5 years for a pure hadronic scenario.
The flux required for a 5σ discovery has also been calculated for a generic point-like source with a E^{-2} energy spectrum. The resulting sensitivity and 5σ discovery flux are shown in Fig. 3.21 as a function of the source declination for six years of data taking. This observation time has been chosen to have a similar exposure as for the IceCube results reported in [126].

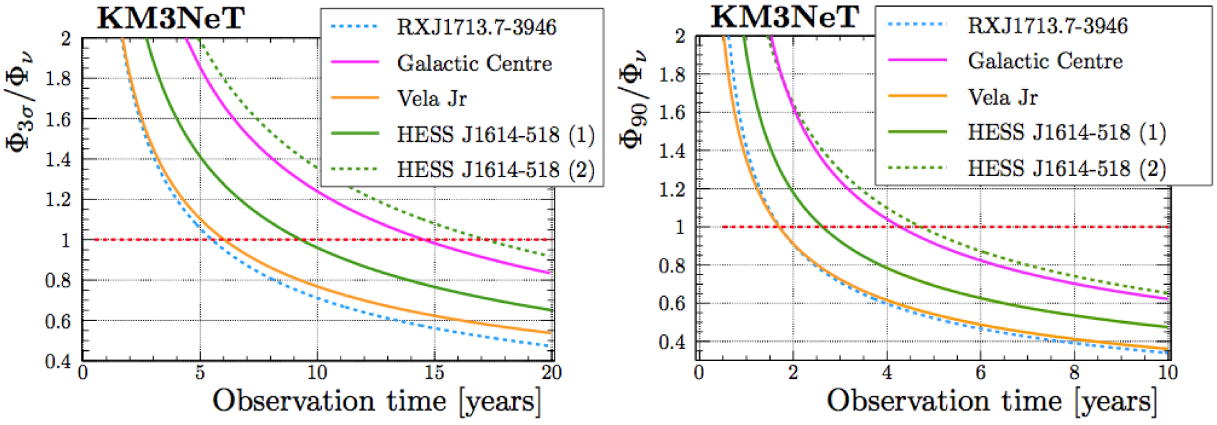

Figure 3.20: In figure the discovery potential $\Phi_{3\sigma}/\Phi_\nu$ (left) and sensitivity $\Phi_{90\%}/\Phi_\nu$ (right) as a function of the observation time for the RX J1713.7-3946 and Vela Junior are reported [125]. The preliminary results for the Galactic Centre and for two different neutrino flux parametrisation of the galactic source HESS J1614-518 are also reported.

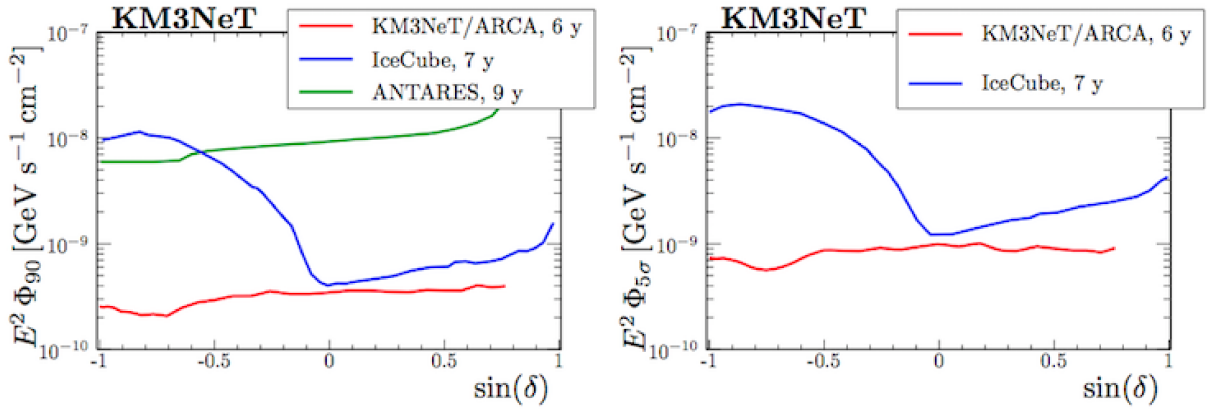

Figure 3.21: Sensitivity (left) and discovery flux at 5σ (right) for sources with a generic neutrino flux proportional to E^{-2}, as a function of the source declination [125]. An observation time of 6 years was assumed. For comparison, the corresponding IceCube [126] and ANTARES [95] results are also shown.

Chapter 4

Monte Carlo simulation and the ANTARES event reconstruction methods

Monte Carlo (MC) simulations are a key tool to understand the detector response to physics events and estimate the detector performance. They play a significant role also to keep under control the correct functioning of all the detector components, optimise the selection cuts for the rejection of the background events and estimate some relevant parameters through which calculate the detector sensitivity.
In the ANTARES and KM3NeT frameworks two different stages of data handling, preceding the data analysis for the production of physics results, can be identified. At first the simulation of both physics and background events, as well as the detector response and the trigger condition is performed through a complete MC simulation chain. This stage involves only simulated events and aims to reproduce real data and study the detector response to physics events. The simulation of real data is carried out by means of a chain of codes. In particular, the atmospheric and signal neutrinos are generated with GENHEN while atmospheric muons are generated with the MUPAGE package. At this point, the muon propagation across the detector and the generation of the hits due to Cherenkov photons are simulated by the KM3 package. In the end, the study of the detector response is done using two different software for the ANTARES and KM3NeT detectors, the TriggerEfficency and JTriggerEfficency packages respectively. These software, in addition to simulate the behaviour of the front-end electronics and apply trigger algorithms, add to physics events the optical background produced by the ^{40}K decay in sea water.
The same reconstruction algorithms are then applied to both simulated and real data, aiming to estimate the arrival direction and energy of the incident neutrino. At this point, the comparison between reconstructed data and MC events makes possible to take under control the detector performance and extract physics information from data. All the above-mentioned software used for the MC simulations and event reconstruction have been developed in the ANTARES and KM3NeT Collaborations. In order to carry

out reliable MC simulations which take into account the not constant data acquisition condition over long period of time, due to the unstable environmental condition in deep see water and the temporary malfunctioning of part of the detector components, the ANTARES and KM3NeT Collaboration follow the Run-by-Run approach. In this approach the simulation of the real data and of the detector covers the same fixed period of time used for the acquisition of data, named *run*. During a *run* all the information related to the current detector configuration are stored and the background rate is extracted directly from data. This strategy ensures to produce MC simulations as much realistic as possible improving the data/MC agreement and allows for a better monitoring of the time evolution of data acquisition.
The software used for the simulation of physics events and the reconstruction algorithms considered in the search for a neutrino counterpart to the HAWC γ-ray sky are described in this chapter, while the results are presented in Chapter 6. Furthermore, some of the main event reconstruction algorithms developed for the ANTARES neutrino telescope for the track-like and shower-like events are also described.

4.1 Event generation method

In ANTARES the first stage of MC simulation is the generation of the detector geometry through the GENDET code [127]. It takes into account all the information about the detector geometry and the current functioning of all detector components. The user can specify the layout of the detector, its geographic coordinates, the spatial coordinates of PMTs, DUs and of all constitutive components. In the analysis presented here the geographic coordinates and the spatial coordinates of the ANTARES layout have been taken into account.
Once the detector geometry is defined, the neutrino-induced muon flux at the detector is generated with the GENHEN code. GENHEN provides a complete simulation of incident neutrinos from 10 GeV up to 10^8 GeV. GENHEN is also responsible for neutrino interactions in the medium and the tracking of resulting secondary particles. The muons produced in the interaction are propagated to the detector and their energy loss is calculated in the process. Since the cross-section of the CC and NC neutrino interactions is very small (see sec. 2.1.1) and in order to reduce the CPU-time, only the neutrino events which interact inside or near the detector able to produce detectable muons are simulated. For this purpose a cylindrical volume, called *can*, containing the instrumented volume of the detector but extended by three times the light absorption length ($\lambda_{abs} = 70m$) in water above the instrumented volume is defined, as shown in Fig. 4.1. The *can* represents the sensitive volume of the detector, because photons produced beyond it have negligible probability to reach the PMTs and produce signals. Therefore, the can defines the volume within which the Cherenkov light is generated in the MC simulation to determine the detector response.
The volume where the simulated events are generated is the *generation volume* (V_{gen}). Precisely, the generation volume is defined as the volume beyond which a muon has negligible probability to reach the *can*. The size of V_{gen} depends on the maximum energy of

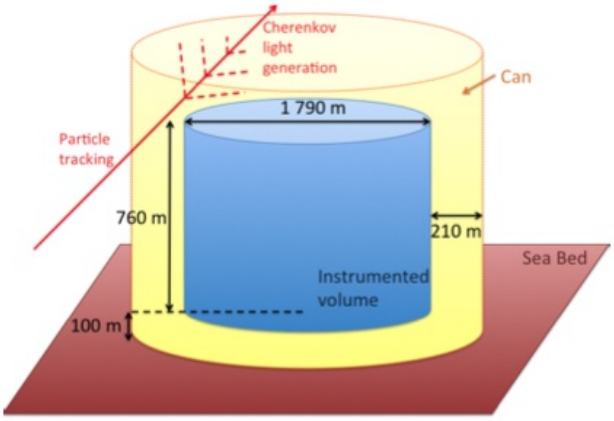

Figure 4.1: Overview of the detector geometry for the event simulation used in GENHEN [128]. Neutrino interactions are generated in a large volume and the resulting muons are propagated to the can (yellow volume). Only inside it the Cherenkov light and the detector response are simulated.

the generated events (E_{max}), on the corresponding maximum muon range in water R_w and in rock R_r and on the angular range of the simulation. Hence, the generation volume is a cylinder exceeding the height of the *can* by R_r for up-going events or $R_w \cos\theta_{max}$ for down-going events, and having R_w as radius. Inside the generation volume neutrinos are generated according to a user defined power law energy spectrum and the neutrino direction can be generated isotropically, in a user defined zenith angle range, or according to a point source mode, from a given declination in the sky.
At this point the neutrino interactions, with rock and water around the detector, are simulated using LEPTO [129] (for deep inelastic scattering) and RSQ [130] (for resonant and quasi-elastic scattering) (see sec. 2.1.1). For a neutrino with the interaction vertex outside the *can*, the shortest distance from the vertex position to the *can* is calculated. No muons produced by this neutrino can reach the *can* if the distance from the vertex position to the *can* is greater than the maximum muon range. In this case the event is rejected. For events with the vertex outside the *can* but whose distance from the *can* is shorter than the maximum muon range only the muon is kept. The muon is then propagated to the *can* using the muon propagation codes MUSIC [131]. For the remaining events with the interaction vertex inside the *can*, all the particles produced in the interaction are recorded for further processing.

4.2 Neutrino fluxes and event weights

In GENHEN a predefined power law energy spectrum $E^{-\gamma}$, specified by the user, is chosen for the generation of the neutrino interactions at the detector level. The advantage of this method relies on the possibility to obtain the neutrino event rates corresponding to a specific model simply *re-weighting* the generated flux, avoiding to repeat the generation of neutrino flux according to the new energy spectra. Thus the new neutrino event rate is

obtained re-weighting each event, generated with E_ν and θ_ν in a given interval $dE_\nu d\Omega_\nu$, with the ratio between the model flux and the generated flux

$$Event\ Rate = \frac{\Phi^{model}(E_\nu, \theta_\nu)}{\Phi^{gen}(E_\nu, \theta_\nu)} \tag{4.1}$$

This approach allows to exploit the relation between the rate of interacting neutrinos at the detector level, Γ^I_ν, and the incoming differential flux Φ_ν of interacting neutrinos at the Earth surface, and at the same time also the possibility to build, at the simulation level, a *weight* for each event which preserves the information about the predefined power law energy spectrum $E^{-\gamma}$. In fact, the distribution of the rate of generated neutrinos Γ^I_ν (in unit of [GeVm^3 s sr]$^{-1}$), interacting at the detector, is described by

$$\frac{d\Gamma^I_\nu}{dE_\nu dV dt d\Omega} = \frac{E^{-\gamma}}{I_E} \cdot \frac{1}{I_\theta} \cdot \frac{N_{total}}{V_{gen}} \cdot \frac{1}{t_{gen}} \tag{4.2}$$

where

- V$_{gen}$[m^3] is the total generation volume;
- I_θ [sr] the angular phase space factor $2\pi \cdot [\cos(\theta_{max}) - \cos(\theta_{min})]$, where θ_{max} and θ_{min} are the maximum and minimum angles of generation.
- I_E the energy space factor, equal to $(E^{1-\gamma}_{max} - E^{1-\gamma}_{min})/(1-\gamma)$ (where E_{max} and E_{min} are the maximum and minimum energies of generation) and to $\ln(E_{max}/E_{min})$ for γ=1;
- t_{gen} is the generation time (arbitrary);
- N_{tot} is the total number of generated events.

The total number of generated events, N_{total} is obtained integrating the previous distribution over the range of simulated angles, energy, time and volume. But the rate of interacting neutrinos depends on the incoming neutrino flux Φ_ν per unit area dS, the target density and the neutrino cross-section. Therefore the incoming neutrino flux Φ_ν arriving at the detector, to which the rate of interacting neutrino correspond to, is described by the ratio between the interaction rate and the target nucleon density times the neutrino interaction cross-section

$$\frac{d\Phi_\nu}{dE_\nu dS dt d\Omega} = \frac{d\Gamma^I_\nu}{dE_\nu dV dt d\Omega} \cdot \frac{1}{\sigma(E_\nu)\rho N_A} = \frac{E^{-\gamma}}{I_E} \cdot \frac{1}{I_\theta} \cdot \frac{N_{total}}{V_{gen}} \cdot \frac{1}{t_{gen}} \cdot \frac{1}{\sigma(E_\nu)\rho N_A} \tag{4.3}$$

where

- $\sigma(E)$[m^2] is the total neutrino cross-section for energy E;
- $\rho \cdot N_A$ is the number of target nucleon per m^3 (N_A is the Avogadro's constant N_A = 6.022·10^{23} mol^{-1}).

The flux of neutrinos arriving at the detector is just the flux of neutrinos arriving at the surface of the Earth times the probability of transmission through the Earth, $P_{Earth}(E,\theta)$, for a particular E_ν and θ_ν. Hence, the flux of simulated neutrinos arriving at the Earth is given by

$$\frac{d\Phi_\nu}{dE_\nu dS dt d\Omega} = \frac{N_{total}}{V_{get} I_\theta I_E E^\gamma \sigma(E_\nu) \rho N_A t_{gen} P_{Earth}(E,\theta)} \tag{4.4}$$

and it is thus expressed in terms of quantities that can be evaluated during the generation phase, the so called *generation weight*

$$W_{generation} = \frac{V_{gen} I_\theta I_E E^\gamma \sigma(E_\nu) \rho N_A P_{Earth}(E,\theta)}{N_{total}} \tag{4.5}$$

This weight preserves the information about the power law energy spectrum $E^{-\gamma}$ used for the generation of neutrino interactions at the detector and usually it is calculated for each event during the generation phase. To obtain the event rates corresponding to a particular model $d\Phi_\nu^{model}/dE_\nu dS dt d\Omega$ it is thus sufficient multiply each event by its generation weight times the new reference model of neutrino production

$$W_{event} = W_{generation} \cdot \frac{d\Phi_\nu^{model}}{dE_\nu dS dt d\Omega} \tag{4.6}$$

This will produce the *event weight*, W_{event}, according to the considered model with a flux independent part, $W_{generation}$.
For high energy neutrinos the probability of being absorbed by the Earth must be calculated taking into account the neutrino interaction cross-section and a model of the Earth density profile. The reference model used for the Earth's density profile ρ_{Earth} in the ANTARES and KM3NeT simulation is the Preliminary Reference Earth Model (PREM). According to this model, the integrated column density of the Earth along the neutrino path L is

$$\rho_L(\theta_\nu) = \int_L \rho_{Earth}(r) dL \tag{4.7}$$

and it is shown on the left plots of Fig. 4.2, for a given zenith angle θ. Since the Earth's density increase towards the Earth's core, the column density crossed by upgoing neutrinos enhance during their path. Therefore, the probability that a neutrino survives crossing the Earth is given by

$$P_{Earth}(E_\nu,\theta_\nu) = e^{-N_A \rho_{Earth}(E_\nu)\rho(\theta)} \tag{4.7}$$

and it is shown on the right plot in Fig. 4.2 as a function of the energy and zenith angle of the neutrino.
Since the Earth's density profile is not uniform, the probability that a neutrino survives crossing the Earth depends on the neutrino zenith angle and energy. For upwards neutrinos, $\cos\theta = 1$, the Earth absorption begins to be significant for neutrino energies

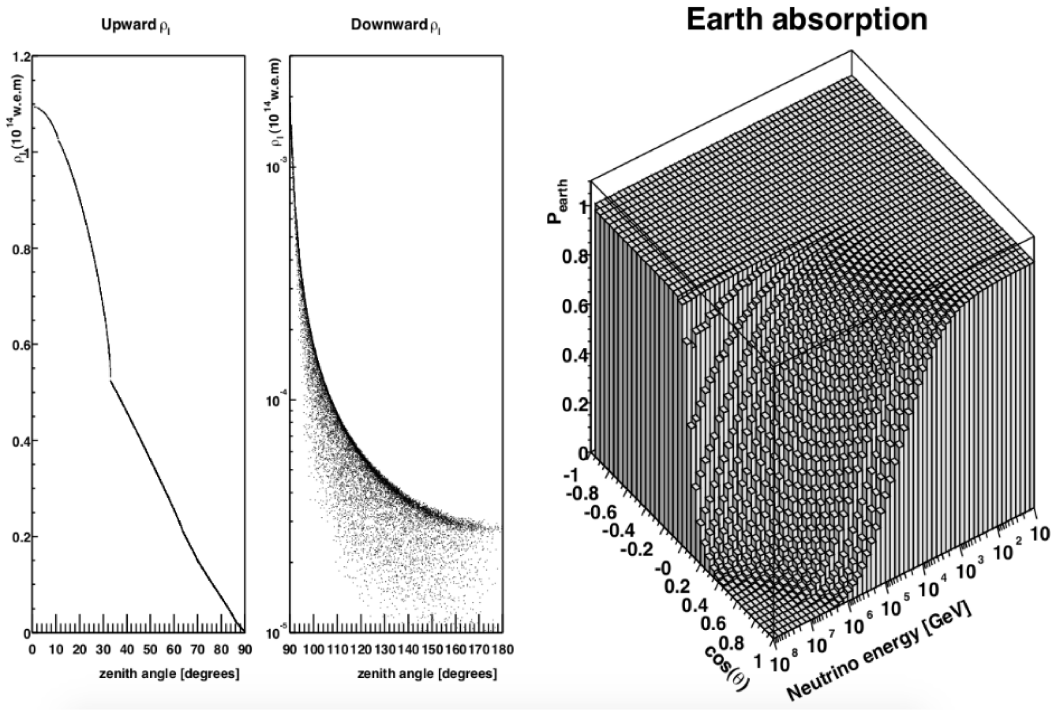

Figure 4.2: In the left panel the integrated column density of the Earth along the neutrino path, for a given zenith angle θ is shown. On the right panel the transmission probability as a function of energy and zenith angle of the neutrino. Events with $\cos\theta > 0^\circ$ are up-going so they cross the Earth before reaching the detector, while events with $\cos\theta < 0^\circ$ are down-going [128].

above 10 TeV. For $E_\nu > 1$ PeV, only neutrinos close to the horizon remain unattenuated, proving that the Earth is opaque to very high energy neutrinos.

4.3 Atmospheric neutrino fluxes

The atmospheric neutrinos are the result of the cosmic ray interactions on the Earth atmosphere and, since different measurements of the primary cosmic ray flux and interaction models exist, several assumptions on the atmospheric neutrino flux can be done. In ANTARES and KM3NeT the simulation of atmospheric neutrinos is done using the GENHEN code weighting the generated neutrino events with an atmospheric neutrino model. In the ANTARES analyses, the Bartol flux [132] is assumed while in the KM3NeT analyses the Honda model [62], for the conventional atmospheric flux, and the Enberg model [60], for the prompt component, are taken into account. Both of them have been corrected for the presence of the knee in the cosmic-ray spectrum.

4.4 Generation of atmospheric muons

For the generation of atmospheric muons the MUPAGE package [133] is used. MUPAGE allows to perform a detailed simulation of extensive air showers produced by the interactions of high energy cosmic rays with the particles present in the Earth's atmosphere. The code is based on parametric formulas derived in [133], which describe the angular distribution and the energy spectrum of underwater muon bundles with depth from 1.5 to 5 km "water equivalent" (w.e.) and with zenith angles less than 85°. The parametrization of the interaction of cosmic rays and the propagation in the atmosphere up to the sea level is based on full simulations of the atmospheric shower performed with the HEMAS code [134], while the MUSIC code propagates muons until 5 km under the sea level. The muons are generated by MUPAGE on a cylindrical surface whose dimensions and position are defined by the user, but usually the same *can* surface used during the generation phase is considered. In the simulation all the muon bundles are parallel to the axis of the shower and they arrive at the same time into a plane perpendicular to the shower axis. Then the "livetime" of every N simulated events, defined as the interval of time in which the flux correspondent to N muons is produced in nature, is estimated.

4.5 Propagation of particles and light production

The propagation of simulated particles through the detector volume produces emission of light inside the *can*. Within this volume three different type of particles able to produce light exist:

- Muons, which are characterized by long and approximately straight tracks. They lose energy emitting Cherenkov photons.
- EM showers, that are produced both through bremsstrahlung photons emitted by muons or by electrons at the neutrino interaction vertex. All their energy is deposited in a short distance (respect to the scale of the detector), so they can generally be considered point-like.
- Hadrons produced at the neutrino interaction vertex. They have complex decay chains and the amount of light produced depends on the primary particle and its particular set of decays. In addition, they may produce muons in the final state which may travel a significant distance.

The light emitted by leptons and hadronic showers, as well as their propagation inside the detector volume, is simulated with KM3 [135]. The code takes into account all the muon interaction mechanisms with matter, the energy loss and the Cherenkov photons emission. It also incorporates the absorption and scattering processes in the sea water. The produced photons are then propagated to the OMs. In order to reduce the CPU time, absorption and diffusion photon tables have been generated for different photon energies and the photon propagation is made by interpolation of these tables. These tables also contain the OM properties and optical water properties. They have to be

re-calculated for different types of OM and different water properties.
The KM3 package is divided into three further subpackages:

- GEN, which generates "photon fields" at various radii from a muon track segment or an electromagnetic shower;
- HIT, that transforms the photon fields from GEN into "hit probability distributions" in a photomultiplier tube;
- KM3MC, a detector simulation program which uses the hit probability distributions generated in HIT with a geometrical description of the detector to simulate events in it.

GEN

The generation of Cherenkov light by a particle in a given medium (in this case water), including also light from any secondary particles, is simulated by GEN. A complete GEANT 3.21 [136] simulation is used at this step. GEN tracks the Cherenkov photons through space taking into account wavelength-dependent absorption and scattering and recording the position, direction and arrival time of photons at spherical shells of various radii. The output of GEN consist of:

- a table containing all the photons recorded in each spherical shell;
- an ASCII file containing the information relevant for the simulation (particle type, energy, number of processed events, track length, medium type, number of events stored in each shell, water model used, etc.).

HIT

HIT creates the Optical Module hit distribution from muon track segments and from the EM showers using the photon fields simulated by GEN. All the information about the hits (position, direction, energy and time) are read shell by shell and stored. Since a large number of hits is recorded for each shell, these shells are divided in angular bins of $\cos\theta$. Then for each bin the flux of photons is weighted by the PMT effective area and orientation, as shown in Fig. 4.3. The PMT effective area is given by

$$A_{eff}^{OM} = A_{geom}(\theta_{OM}) \cdot QE(\lambda) \cdot CE \cdot P_{trans}^{glass}(\lambda, \theta_{OM}) \cdot P_{trans}^{gel}(\lambda, \theta_{OM}) \qquad (4.7)$$

where λ is the photon wavelength, $QE(\lambda)$ is the quantum efficency (which is the probability that a photon generates a photoelectron inside the PMT), CE is the collection efficency (the probability that an electron inside the PMT is accelerated up to the first photocathod) and finally $P_{trans}^{glass}(\lambda, \theta_{OM})$ and $P_{trans}^{gel}(\lambda, \theta_{OM})$ are the transmissions probability of the glass and the gel that constitute the OM.

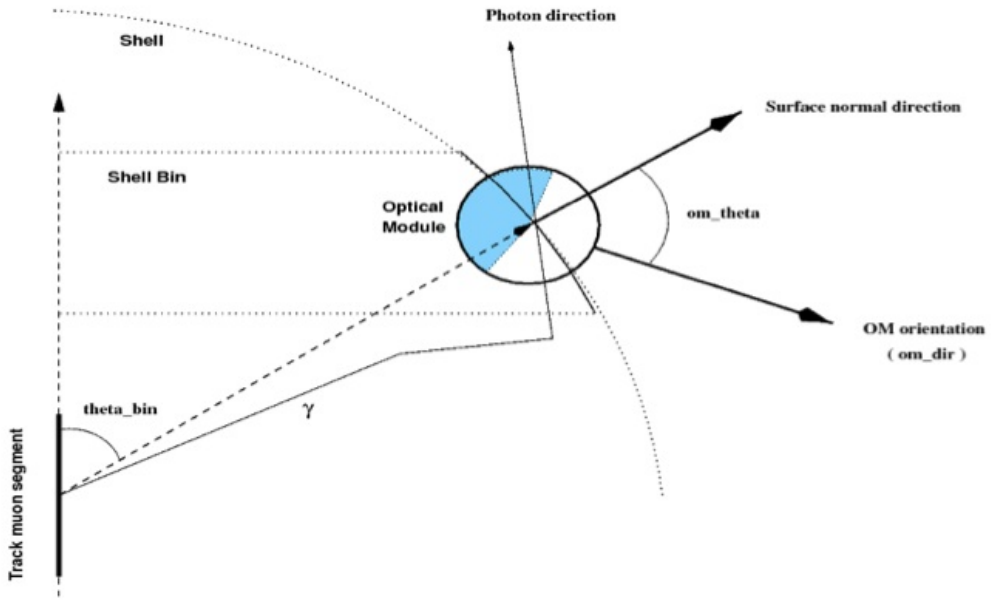

Figure 4.3: A schematic view of the geometry used to generate the photon tables.

KM3MC

The output of HIT is read by KM3MC and the muons are propagated through the *can* volume with the MUSIC package. This code generates segment of track of the same dimension of those used by GEN until the muon leaves the detector or stops. The energy loss is evaluated and if it is greater than a threshold value, an EM shower is generated in a random position along the segment track.
At this point the signal "hits" are obtained from the track and shower parameters (initial and final position, direction, time of occurrence). For all hits the identifier of PMT involved, the number of deposited photoelectrons (p.e.) and the photon arrival time are recorded.

4.6 Generation of optical background and trigger simulation

Once that the simulated events have been propagated until the detector and the emission of Cherenkov light has been simulated, three additional steps characterise this stage of the MC chain:

- the addition of the optical background to simulated events;
- the simulation of the detector response to individual hits;
- the triggering of simulated events by means of the same trigger algorithms considered during the data acquisition.

For both the ANTARES and KM3NeT telescopes, the environmental conditions responsible for the emission of the optical background are the light produced by the ^{40}K decay and by the bioluminescence activity present in the sea water. Whereas, the detector response and the trigger conditions are strictly related to the different detector geometries and trigger algorithms considered to discriminate signal from background events. For this reason, at this stage of the MC simulation, two different codes are used in the ANTARES and KM3NeT frameworks, the TriggerEfficiency [137] and JTriggerEfficiency [138] package respectively.
TriggerEfficiency is used to process the MC data and it takes into account the main features of the ANTARES PMTs. The number of simulated photon is used to determine the charge of the analogue pulse. The simulated charge of the analogue pulses are generated according a Gaussian distribution with a specified width and gain. In order to take into account also the effect of a reduced quantum efficiency (QE) on-the-fly, a relative QE with a values ranging between 0 and 1 is applied. The time of simulated hits is generated according a Gaussian distribution with a specified width, the so-called transition-time spread (TTS), which for the ANTARES PMTs is of about $\sigma_{TTS} = 1.3$ ns.
The JTriggerEfficiency code is part of the JPP package. Through this code, at first, the hits due to optical background are simulated and added to physics events. In order to do this, a 5 kHz rate per PMT is simulated, which produces correlated hits of 2, 3 and 4 coincidences between PMTs in the same DOM at frequencies of 500, 50 and 5 Hz. Then, two different trigger algorithms, called JTrigger3DShower and JTrigger3DMuon, can be applied to simulate the same trigger criteria used for the triggering of real data for the two different event topologies.
The simulation of the detector response is performed both in the TriggerEfficiency and the JTriggerEfficiency codes by using the summary data taken during operation, in which all the information about the functionality of all detector components is stored.

4.7 ANTARES reconstruction methods

The event reconstruction procedure is a crucial point in the data processing chain because it allows to estimate two important information, the arrival direction and energy of interacting events. Since in a neutrino telescope two different event topologies can be identified, the track-like and the shower-like events, different reconstruction algorithms have been developed to reconstruct the typical patterns of these two classes of events. The key point of the reconstruction procedure for both of the two event topologies is the search for the time-space correlation among the Cherenkov hits detected by different OMs in an event and the features that characterised one of the two event topologies. In the case of a track-like event a muon can travel several kilometers in sea water producing a very long track. In order to reconstruct the muon trajectory and infer the direction of incident neutrino, the algorithm maxmises the likelihood that the detected Cherenkov hits are in space and time correlation with the reconstructed track. At the same time, since the amount of light collected by the PMTs is correlated with the muon energy, these algorithms exploit this relation to estimate the energy of the interacting event.

For shower-like events, since in the GeV-TeV energy range the length of the shower is of about 10 m, the reconstruction of both the direction and the energy of interacting event is much more complicated than in the previous case and a different approach is used to reconstruct the vertex position, direction and energy of the event.
In the following sections the main track and shower reconstruction algorithms used in the ANTARES data analysis are described.

4.7.1 Track reconstructiod: AAFit

Several track reconstruction algorithms have been developed by the ANTARES Collaboration and, among them, the AAFit is the one currently used for point-like source searches due to its better detection efficiency at high energies and angular resolution. The algorithm is based on a two steps procedure. At first a multi-step procedure based on a linear prefit, an M-estimator fit and a maximum likelihood fit is performed. Then, the output of the last fit is used as starting point for a further maximum likelihood fit, which returns the direction of the reconstructed track.
The muon tracks can be described by the position $\vec{p} = (p_x, p_y, p_z)$ of the muon at a fixed time t_0 and its normalized direction $\vec{d} = (d_x, d_y, d_z)$, which may be parameterized in terms of the azimuthal and zenithal angles, ϕ and θ, as $\vec{d} \equiv$ (sin θ cosϕ, sin θ sin ϕ, cos θ). The reconstruction algorithm allows to estimate the five parameters p_x, p_y, p_z, θ, ϕ of the track while the track fit quality parameter is used to reject badly reconstructed events.
At the reconstruction level one of the most important parameter is the "time residual", defined as the difference between the expected arrival time t^{th} of the photon on the PMT and the recorded hit time t_i. The time residual is calculated considering that the event starts at a time t_0, the muon travels on a straight line with speed c and the Cherenkov light is emitted at an angle $\theta_C \sim 42°$ with respect to the muon direction, with a speed c/n, where n is the refractive index in the medium ($n \sim 1.35$). For a given OM and a given track, the expected arrival time of a photon to an OM is given by

$$t^{th} = t_0 + \frac{1}{c}\left(l - \frac{k}{\tan\theta_C}\right) + \frac{1}{v_g}\left(\frac{k}{sin\theta_C}\right)$$

where v_g is the group velocity of light in water and k is the shortest distance between the track and the OM, as sketch in Fig. 4.4. In order to perform the reconstruction, the algorithm needs as input parameters the time residual of each hit, the photon path length ($b = k/sin\theta_C$), the angle of incidence of the photons into the OM and the amplitude in term of the number of p.e..
In the first step of the reconstruction chain a hits pre-selection is performed by considering all the hits with satisfying the condition

$$\mid \Delta t \mid \leq \frac{d}{v_g} \; + \; 100\, ns$$

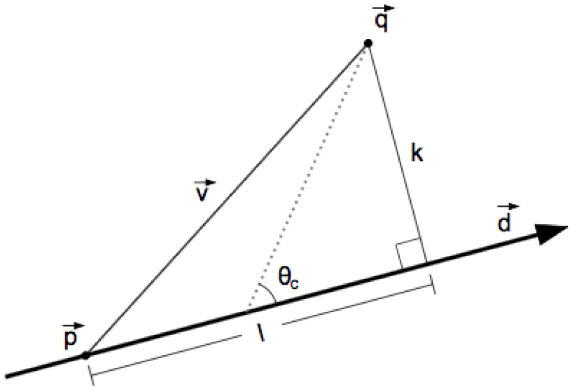

Figure 4.4: Sketch of a muon passing through the detector coming from a direction $\vec{d}$ at a position $\vec{p}$ for a given time t_0. The dotted grey line represents the Cherenkov radiation emitted by the muon at an angle θ_C, while the $\vec{q}$ vector shows the location of a OM. The vector $\vec{v} = \vec{q} - \vec{p}$ gives the distance between the point $\vec{p}$ and the OM. The perpendicular and parallel components of $\vec{v}$ with respect to the direction of the muon are represented by the k and l segments.

where Δt is the time difference between a hit with a given v_g respect to the one having the largest amplitude, and d denotes the distance between the OMs. With the preselected hits a linear pre-fit is performed under the assumption that the position of the considered hits lies along the muon trajectory.
The output information of the linear pre-fit is used in order to perform an M-estimator minimisation. The further condition on the hit time residual

$$-150 \leq t_{res} \leq 150\ ns$$

within distances from the fitted track smaller than 100 m, or with amplitudes larger than 2.3 p.e., is considered. The function to be maximised depends on the time residuals of the hits, t_{res}, and the angular response function of the optical module, f_{ang}.
The best fit parameters from the M-estimator are used for a maximum likelihood fit. At this stage only hits with a time residual between -0.5 $t^{RMS} < t_{res} < t^{RMS}$ are considered, where t^{RMS} is the root mean square of the time residuals obtained from the M-estimator fit. The likelihood function used in the maximization procedure can be described as the product of the probabilities of each individual hit

$$L = \prod_i P(t_i \mid t_i^{th}, a_i, b_i, A_i) \tag{4.7}$$

and, at this step, only the information of the hit time and the expected arrival time are considered. Since the likelihood maximisation is sensitive to the starting point position, the previous two steps are repeated considering eight alternative additional starting points chosen by rotating or translating the track direction from the pre-fit. The number of starting points, N_{comp}, which provides a track within 1° from the one with the largest likelihood is stored.

In the last step of the reconstruction procedure a maximum likelihood fit takes all the information from Eq. 5.7 together with the direction and position of the best fit from the previous step. At the same time the quality parameter Λ, related to the goodness of the reconstruction procedure, is estimated

$$\Lambda = \frac{logL}{N_{dof}} + 0.1(N_{comp} - 1)$$

where N_{dof} is the number of degrees of freedom (N_{hits} – 5) and N_{hits} the number of selected hits. The angular error estimate of the track can be obtained from the error estimates on the zenith, β_θ, and azimuth, β_ϕ, angles as

$$\beta = \sqrt{\beta_\theta^2 + sin^2\theta\beta_\phi^2}$$

Once that the track reconstruction has been performed by AAFit, the energy of an event is derived through the $dEdX$ energy reconstruction method [139, 140]. Even if a muon coming from ν_μ CC interaction can release a large fraction of their energy outside the detector volume, a correlation between the amount of energy deposited per unit length by the muon and the energy of the event can be established. The $dEdX$ method reconstructs the energy by calculating the parameter

$$\rho = \frac{\sum_i^{N_{hits}} Q_i}{\epsilon} \frac{1}{L_\mu}$$

where Q_i is the charge collected from the hit i, L_μ is the reconstructed track length of the muon within a volume defined by the cylinder of the ANTARES instrumented volume increased by twice the light attenuation length, and ϵ is the ANTARES light detection efficiency. The ρ parameter is calculated considering only the hits used in the last part of the AAFit reconstruction procedure. In Fig. 4.5 the ANTARES angular resolution for events coming from ν_μ CC interactions is shown. An angular resolution of about 0.3° is reached for E_ν above tens of TeV. This result has been obtained by considering the following cuts: $\Lambda > -5.2$, $\cos\theta > -0.1$, $\beta < 1°$, $log_{10}(\rho) > 1.6$, $L_\mu > 380$ m. The $dEdX$ method allows to obtain an angular resolution better than 0.4° for energies above 10 TeV.

4.7.2 Cascade reconstruction: TANTRA

TANTRA [141, 142] is the cascade reconstruction algorithm which allows to obtain the best angular resolution in ANTARES. This reconstruction algorithm at first reconstructs the vertex of the interaction and then the direction of the cascade is fitted. At each step a specific hits selection is performed. In order to reconstruct the interaction vertex,

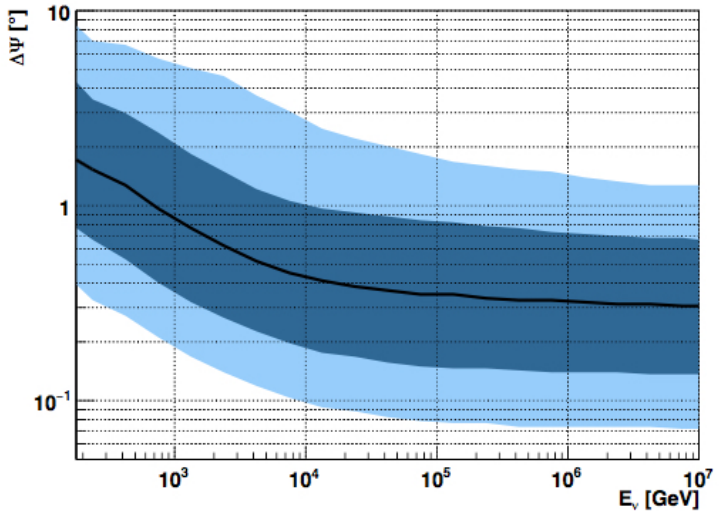

Figure 4.5: Angular resolution for track events coming from ν_μ CC interactions using AAFit events. The following cuts have been applied: $\Lambda > -5.2$, $\beta < 1^\circ$, $cos\theta > -0.1$, $L_\mu > 380$m and $log_{10}(\rho) > 1.6$ have been applied. The dark blue area shows the 1σ region, whereas the light blue area shows the 90% belt.

TANTRA looks for samples of hits from a triggered event such that each pair of selected hits satisfy the condition

$$\mid \vec{r}_i - \vec{r}_j \mid \geq c_W \mid t_i - t_j \mid$$

where $\vec{r}_i$ is the position of the OM of the detected hit i, t_i is the recorded time of the hit, and c_W is the speed of light in water. Among all samples the one with the largest sum of detected hit charges is considered. Once the hit selection is done, a pre-fit is performed to obtain the location of the vertex position under the assumption that all selected hits come from the same interaction vertex. Therefore, each hit should has

$$(\vec{r}_i - \vec{r}_{vertex})^2 = c_W^2 (t_i - t_{vertex})^2$$

where r_{vertex} and t_{vertex} indicate the location and time of the fitted vertex, and i is the index of each of the N selected hits. Exploiting this information, the pre-fitted vertex position and time are obtained performing a least square fit minimization. These values are used as the starting point for the M-estimator fit, which minimises the function

$$M_{Est} = \sum_i^N (q_i \sqrt{1 + t_{i-res}^2/2})$$

with q_i and $t_{i-res} = t_i - t_{Shower} - \mid \vec{r}_i - \vec{r}_{Shower} \mid / c_W$ are the charge and the time residual of the hit i respectively.

The reconstruction of the cascade direction is based on a different hit selection. All the triggered hits with a time residual

$$-200\ ns\ <\ t_{res}\ <\ 500\ ns$$

are considered, with t_{res} the time residual respect to the previously fitted vertex. The hits arriving at the same PMT are merged, with a corresponding charge given by the sum of the charge of individual hits and the time taken as the one of the first detected hit in the PMT. The direction of the cascade is then obtained performing a maximisation of a likelihood defined as

$$LogL = \sum_{i=1}^{N_{selected}} log[P_{q_i>0}(q_i \mid E_\nu, d_i, \phi_i, \alpha_i) + P_{bg(q_i)}] + \sum_{i}^{N_{PMTwithouthits}} log[P_{q=0}(E_\nu, d_i, \phi_i)]$$

where $P_{q_i>0}$ denotes the probability for the PMT i to measure a charge q_i, $P_{q=0}$ is the probability of not measure the charge, and P_{bg} is the probability for the PMT i to detect a hit with charge q_i from background. All these probabilities depend on the charge of the hit, q_i, while $P_{q_i>0}$ and $P_{q=0}$ depend on the neutrino energy, E_ν, the distance between the PMT i and the vertex of the interaction, d_i, the angle between the neutrino direction and the vector which connects the PMT i with the interaction vertex, ϕ_i, and the angle between the direction of the PMT with the incident photon, α_i. In Fig. 4.6 the performances of the TANTRA reconstruction method are shown. For contained events, which means events within $\mid Z_{vertex} \mid < 300$ m and $\rho_{vertex} < 250$ m from the detector centre, a median angular resolution between 2° and 4° can be achieved for ν_e CC events with energies between 10^3 and 10^6 GeV.

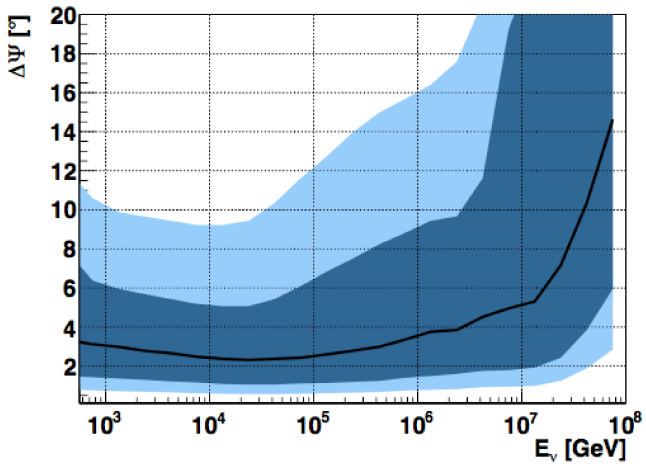

Figure 4.6: Angular resolution for cascades coming from ν_e CC interactions using the TANTRA reconstruction method. The same event selection of the last ANTARES point-source analysis has been considered. The dark blue area shows the 1σ region, whereas the light blue area shows the 90% belt.

Chapter 5

Neutrino counterpart to the HAWC γ-ray point source sky maps

Most of the γ-ray sources of our Galaxy show a power law energy spectrum consistent with acceleration shock of charged particles, which could provide the evidence of the hadronic origin of γ-rays produced in the Milky Way. In consequence of the cosmic ray interactions with the dense matter in our Galaxy, it is also expected that a significant component of the diffuse neutrino flux reaching the Earth has a galactic origin and it can be directly related with the observed galactic γ-ray emission. In this case, the brightest γ-ray regions of the Galaxy, like the Galactic Plane, are considered the suitable sites for the production of such a neutrino component.
The *2 years HAWC γ-ray source catalogue* [143], recently published by the HAWC Collaboration, represents the most sensitive survey of the TeV sky at the present day and it can be used to investigate the origin of the diffuse neutrino emission in our Galaxy. The catalogue construction is based on the analysis of γ-ray sky maps of reconstructed signal and the background events. The sky maps are then analysed using a maximum likelihood approach and the significance of a cluster of events is estimated through a hypothesis test.
In this work the possibility to detect the corresponding neutrino emission to the HAWC γ-ray sky maps with the ANTARES telescope is investigated. In order to search for a neutrino counterpart to the HAWC γ-ray sky, two γ-ray point source sky maps have been considered as reference models to determine a topological and spectral energy distributions of the neutrino flux all over the sky. The sky maps have been provided by the HAWC Collaboration specifically for this analysis in compliance with the memorandum of understanding between the HAWC and the ANTARES Collaborations.
The source model of the maps consists of a single test source with a fixed geometry (point source) and a power law with fixed spectral index as energy spectrum. In particular in the first map, that is the one used by the HAWC Collaboration to develop the 2 years HAWC γ-ray source catalogue, a power law $dN/dE = F_0\ (\mathrm{E}/1\mathrm{TeV})^{-2.7}$ is assumed as energy spectrum. In the second map a power law energy spectrum with a different spectral index and reference energy, $dN/dE = F_0\ (\mathrm{E}/7\mathrm{TeV})^{-2}$, is considered. For both maps

F_0 is the differential flux at reference energy in [$\mathrm{TeV}^{-1}\mathrm{s}^{-1}\mathrm{cm}^{-2}$].
Even if only a fraction of the observed Galactic γ-ray emission can be considered of hadronic origin, in this work a one-to-one correspondence between the γ-ray and neutrino fluxes has been assumed to derive the neutrino counterpart to the HAWC γ-ray sky maps. Even though this assumption is not strictly corrected it allows to obtain an optimistic limit setting on the corresponding neutrino flux. A much more realistic neutrino production model will be taken into account in a future analysis.
In this chapter, after a brief description of the HAWC water Cherenkov telescope and of the construction of the γ-ray point source sky maps, the procedure followed to derive the neutrino emission corresponding to such maps is presented. The possibility to detect the corresponding neutrino emission with the ANTARES telescope will be investigated in the next chapter.

5.1 The HAWC water Cherenkov telescope

The HAWC (High Altitude Water Cherenkov) detector is the most sensitive wide-field-of-view telescope for γ-rays at TeV energies currently in operation, with a 1-year survey sensitivity of about 5–10% of the flux of the Crab Nebula. Unlike the Imaging Atmospheric Cherenkov Telescopes (IACTs), such as H.E.S.S., MAGIC, VERITAS, and FACT which observe the Cherenkov light emitted by the extensive air showers as they develop in the atmosphere, HAWC (see Fig.5.1) detects particles of these air showers that reach the ground level, allowing it to operate continuously and observe an instantaneous field of view of 1.5 sr.

Figure 5.1: The HAWC observatory in Mexico at 18° 59'41" N 97° 18' 30.6" W and an elevation of 4100 m a.s.l.. [8]

The HAWC observatory is located in Mexico, at an elevation of 4100 m a.s.l., and consists of 300 water Cherenkov detectors tanks of about 5 m height and 7.30 m of diameter. Four upward-facing photomultiplier tubes (PMTs) are mounted at the bottom of each tank and the WCDs are arranged in a compact layout to maximize the density of the sensitive

area, as sketch in Figure 5.2. The WCDs are filled to a depth of 4.5 m, more than 10 radiation lengths of water above the PMTs. This large depth guarantees that electrons, positrons, and γ-rays in the air shower are absorbed in the tanks, so that the detectors act as an electromagnetic calorimeter providing an accurate measurement of electromagnetic energy deposition. The high-energy electrons are detected via the Cherenkov light they emitt in the WCD water, while gamma rays produce electrons through pair production and Compton scattering, which in turn are detected exploiting the Cherenkov effect they induce in the WCD water.

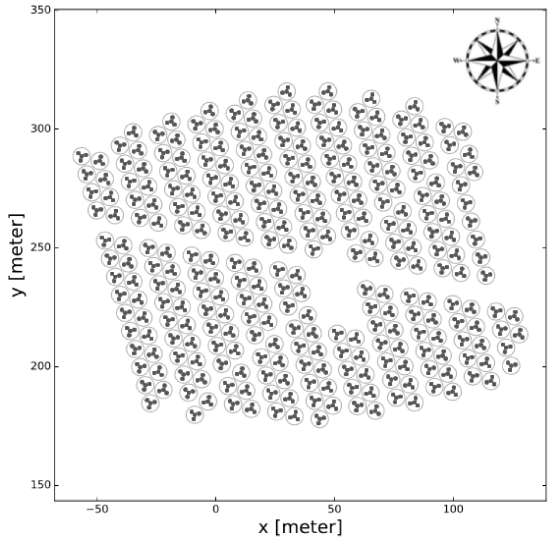

Figure 5.2: Layout of HAWC WCDs and positions of the PMTs (PMT not to scale) [143].

For each triggered event the parameters of the air shower, such as the direction and the size, as well as some relevant variable for the gamma/hadron separation analysis, are extracted from the recorded hit times and amplitudes using a reference shower model developed through Monte Carlo simulations. The model accounts for both γ-ray induced showers and the hadronic background. In fact, the first are generally compact with a smooth lateral distribution (i.e. the spread of particles) around the shower axis. In contrast, the hadronic background events are broader, with badly defined cores and large signals from muons and hadrons at significant distance from the shower axis. Then selection cuts on shower morphology, optimised through Monte Carlo simulations, allow to reduce most of the hadronic background and discriminate between signal and background events.

Compared to the previous generation of surface arrays, represented by the MILAGRO and the ARGO observatories, the HAWC sensitivity is improved by more than an order of magnitude thanks to its large size, high elevation, and unique background rejection capability. All these features make the HAWC observatory an ideally suited instrument for very high energy sky survey. In addiction to the better sensitivity at VHE energies, the higher HAWC performance takes advantage also from its larger angular resolution

respect the IACT's one.
Due to the development of air showers in the atmosphere, the HAWC's sensitivity and its energy response varies with the source declination as shown in Fig. 5.3. These dependences have been taken into account in the point source search analysis performed to develop the 2 years HAWC γ-ray catalogue. In fact, only sources with a declinations between –20° and 60° have been considered. In Fig. 5.3 the curves correspond to the flux

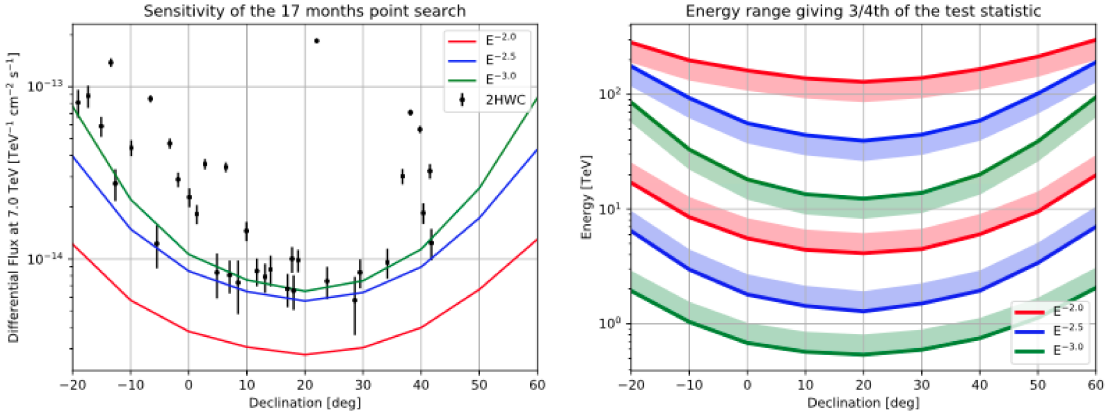

Figure 5.3: The flux required to obtain a central expectation of 5σ, for the point source search in the HAWC 2 years γ-ray catalogue analysis, as a function of declination are shown in the left panel [143]. Three different spectral hypotheses are considered. The differential fluxes of the sources detected in the point source search are also shown with their statistical uncertainties. On the right panel the upper and lower ends of the energy range contributing to the test statistic of the point source search are shown.

that gives a central expectation of a 5σ signal for a point source with a power law flux of index –2.0, –2.5, and –3.0. The maximum sensitivity is obtained for sources transiting at the zenith of HAWC, whose declinations are close to 19°. In Fig. 5.3 the sources observed in the point source search, with statistical uncertainties, are also shown at the corresponding declination.

5.2 The 2 years HAWC γ-ray source catalogue and sky map generation

The full HAWC observatory has been completed in March 2015. The 2 years HAWC γ-ray catalogue has been realised using the data collected between 26 November 2014 and 2 February 2016, which correspond to the 92% of duty cycle of the HAWC detector, and with a variable number of WCDs, ranging from 250 to 300. The catalogue lists the position and the energy spectrum, with uncertainties, of 39 sources. Seven of the detected sources can be associated with pulsar wind nebulae, two with supernova remnants, two with blazars (AGNs), while the remaining have no definitive identification yet.
The events used to realise the catalogue have been reconstructed and analysed using *Pass4*, a new software which accounts for the improvement on the calibration procedure,

event reconstruction and on the likelihood approach used for the map analysis. In particular, the new event reconstruction strategy takes advantage from a directional fit which uses an improved shower model, a new algorithm to separate γ-ray and hadronic events and also a better electronics model. The reconstructed events have been classified in nine bins according to the fraction, f_{hit}, of active PMTs of the detector that are involved in the reconstruction procedure of the air shower. A further event selection has been also performed applying cuts on the gamma/hadron separation variables, optimised for each bin using observations of the Crab Nebula. Precisely, the cuts on the efficiency of the gamma/hadron separation have been estimated using Monte Carlo simulations of the detector for the gamma efficiency and through direct measurement of the hadron efficiency from cosmic ray data.
The reconstructed events have been then used to generate the event and background sky maps. The event map is simply an histogram of the arrival direction of the reconstructed events, in the equatorial coordinate system, while the background map is computed using a method based on a new background rejection technique, developed by the MILAGRO experiment, named *direct integration*. This technique is used to fit the isotropic distribution of events that pass the γ-ray event selection, taking into account for the asymmetric detector angular response and the variation of the all-sky rate. Since strong γ-ray sources can bias the background estimate, for the production of the background sky map some regions of the sky are not included. The excluded regions cover the Crab Nebula, the two Markarians, the Geminga source and a region of the sky over $\pm$ 3° around the inner Galactic Plane.
The event and background sky maps are then created using the HEALPix pixelization [144]. In this pixelization scheme a sphere (representing the sky) is divided in 12 pixels and each pixel is further divided into a grid of $N_{side} \times N_{side}$. For the analysis presented in [143] sky maps with $N_{side} = 1024$ have been produced, which corresponds to an average distance between the pixel centers less than 0.06°.
Since high-energy photons are absorbed by the interactions with the interstellar medium, most of the observed sources listed in the 2 years HAWC γ-ray catalogue are in the Milky Way. The majority of these objects are indeed at low galactic latitude, along the Galactic Plane. It should be noted that a significant component of the observed γ-ray emission could be related to the Galactic Plane itself, which can not be disentangled from the point-source one and it could actually contribute to the measured flux for these individual sources.

5.2.1 Source hypothesis test

The event and background sky maps are analysed using the maximum likelihood approach presented in [145]. In this method the significance of a cluster of events is estimated through a hypothesis test (TS) based on the likelihood ratio between the maximised value of the likelihood of a source model, $\mathcal{L}$(Model), and its value for the only-background hypothesis, $\mathcal{L}$(Null Model)

$$TS = 2 \ln \frac{\mathcal{L}^{max}(\text{ Source Model})}{\mathcal{L}(\text{ Null Model})} \tag{5.1}$$

The likelihood of the source model is obtained by comparing the counts of the observed and expected events in the pixels covering the region of interest in all the nine analysis bins. In this case the expected counts correspond to the same background counts plus a signal contribution from the source derived from simulations. For the null model the likelihood is computed considering the background counts derived from data.
In order to search for sources and determine the source characteristics, the TS is maximised with respect to the source flux, which is the only free parameter of the model. Therefore a TS map is built by moving the location of the hypothetical source across the possible locations in the sky. According to the Wilks' Theorem [146], if the statistics are sufficiently large the TS follows a χ^2 distribution with one degree of freedom and the significance of the search is obtained by taking the square root of the test statistic. As shown in Fig. 5.4, the distribution of $\sqrt{TS}$ is well reproduced by the Normal distribution for $\sqrt{TS}$ values lower than ~ 3, whereas at greater values a large excess can be seen due to the presence of sources in the sky.

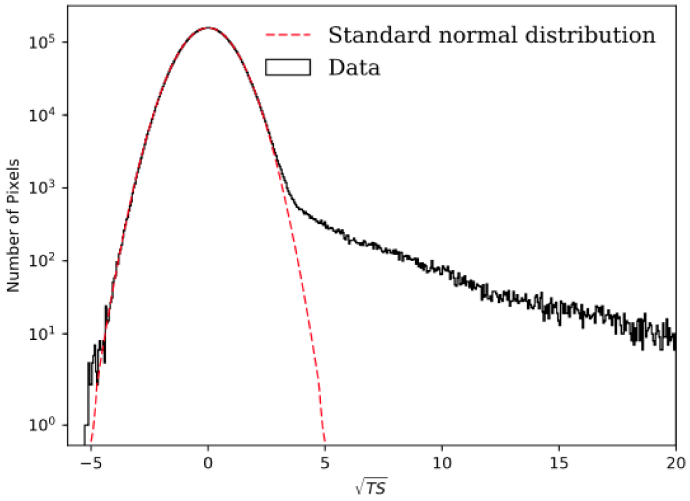

Figure 5.4: The test statistic distribution for the HAWC point source search (black) and standard normal distribution (red) used to fit the null hypothesis [143].

5.2.2 Catalogue construction

In order to build the HAWC catalogue taking advantage from the HAWC's sensitivity to both point-like and extended sources, multiple searches have been carried out considering different source morphologies. The source model used to compute the TS map consists of a single test source with a fixed geometry (point source or uniform disk of fixed radius)

and a power law of fixed index as energy spectrum

$$\frac{dN}{dE} = F_0(E/E_0)^{\alpha} \quad [\mathrm{TeV}^{-1}\mathrm{s}^{-1}\mathrm{cm}^{-2}] \tag{5.2}$$

where E_0 is a reference energy, F_0 is the differential flux at E_0 and α is the spectral index. To account for the different source extensions and the wide range of spectra observed by HAWC, four different maps have been used to build the catalogue and testing different source hypotheses

1. a point source map of index –2.7 (map resolution $N_{side} = 1024$ or 0.06° per pixel);
2. an extended source (fixed radius equal to 0.5°) map with index –2.0 (map resolution $N_{side} = 512$ or 0.1° per pixel);
3. an extended source (fixed radius equal to 1.0°) map with index –2.0 (map resolution $N_{side} = 256$ or 0.2° per pixel);
4. an extended sources (fixed radius equal to 2.0°) map with index –2.0 (map resolution $N_{side} = 256$ or 0.2° per pixel).

To limit the possible source contamination when multiple nearby sources are added together, the priority of the search is given to the point source search. The position of both point-like and extended source, with characteristic sizes 0.25°, 0.5°, 1° and 2°, is then identified from a list of local maxima in the $\sqrt{TS}$ maps. All local maxima with TS > 25 are considered. When multiple local maxima are found the primary sources are defined as all local maxima that are separated from neighboring local maxima of higher significance by a valley of $\Delta(TS) > 2$. While secondary sources are those satisfying the condition $1 < \Delta(\mathrm{TS}) < 2$. In the catalogue [143] all the sources of the point source search plus the sources of the extended searches, ordered by increasing radius, are listed.
For the analysis presented in this thesis the point source sky map of index $\alpha = -2.7$ (HEALPix map resolution $N_{side} = 1024$ or 0.06° per pixel) has been used to evaluate the ANTARES sensitivity to a neutrino flux emitted by γ-ray point sources. The full-sky test statistic map is shown in Fig. 5.5. In the map some well-known sources are clearly visible, like the Galactic Plane, the Crab Nebula, Geminga, Markarian 421 and Markarian 501. In Fig. 5.6 the corresponding differential flux sky map is shown in the equatorial coordinates reference system.

5.3 Neutrino counterpart to HAWC point source sky maps

The neutrino counterpart of the HAWC sky maps has been obtained following a two step procedure. Since the HAWC data are written in FITS (Flexible Image Transport System) format while the ANTARES data are created using the ROOT Analysis Framework of CERN, a conversion of the HAWC data from FITS to ROOT format has been done. The map of the expected number of reconstructed neutrino events is then built *re-weighting*

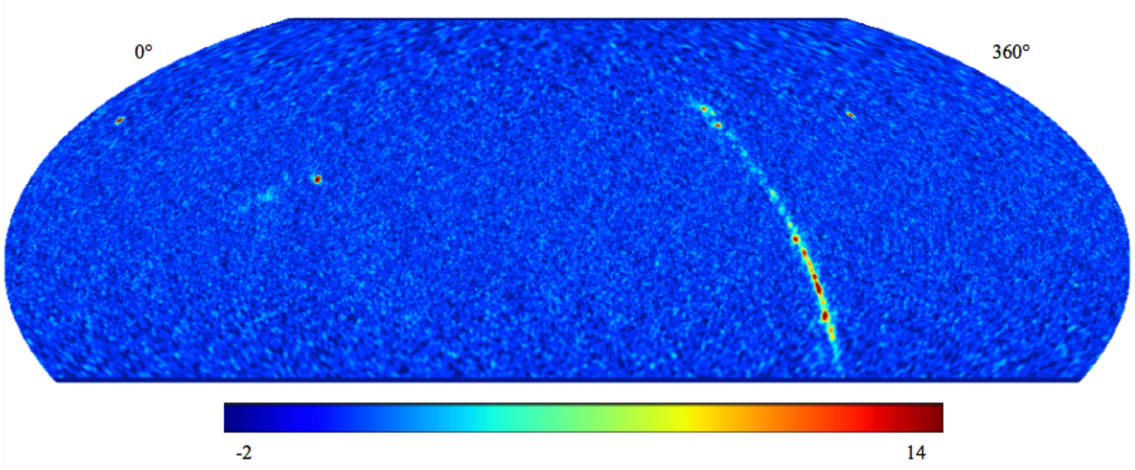

Figure 5.5: The Mollweide projection of the HAWC full-sky test statistic map, reported in the equatorial coordinates reference system, for a point source hypothesis with a spectral index of $\alpha = -2.7$.

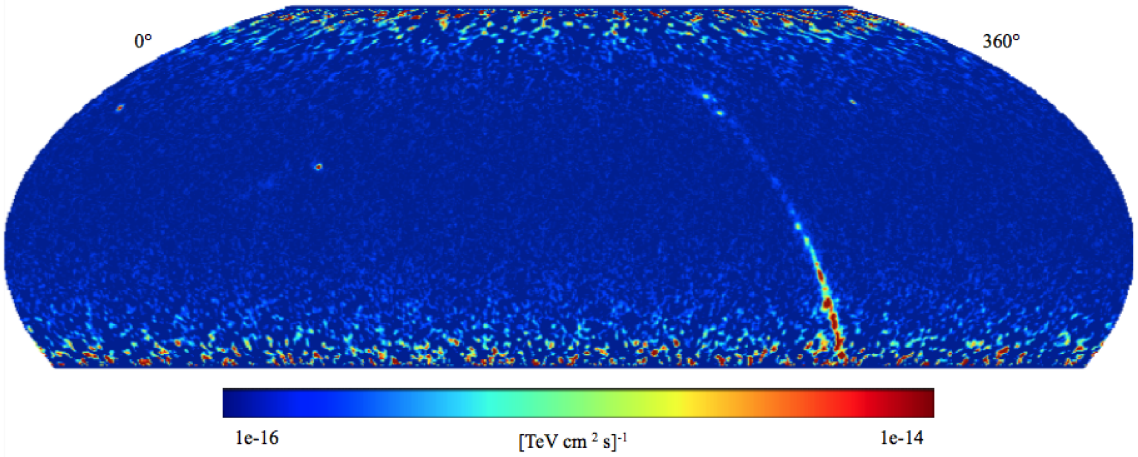

Figure 5.6: The Mollweide projection of the HAWC full-sky map, reported in the equatorial coordinates reference system, for a point source hypothesis with a spectral index of $\alpha = -2.7$

the ANTARES MC events assuming the HAWC sky maps as reference models and a one-to-one correspondence between neutrino and γ-ray differential fluxes, $F_\nu = F_0$ (see Eq. 7.2).

5.3.1 HAWC point source data processing

In order to read the HAWC data and convert them into ROOT file the *healpy* python package for reading, writing and manipulating maps has been used. In *healpy* a map is simply a numpy array, where each array element refers to a location in the sky as defined by the HEALPIX scheme.
The pixelization of the HAWC sky maps, which correspond to $N_{side} = 1024$ and a pixel

angular resolution $\theta_{pix} = 0.06°$, is too over refined to be reproduced with ROOT. For this reason a new pixelization schemes, with $N_{side} = 64$, having a pixel size corresponding to the ANTARES angular resolution in the GeV–TeV energy range ($\theta_{pix} \sim 1°$) has been considered.
To reduce the number of pixels the healpy `pixelfunc.ud_grade` method has been used. This method upgrade or degrade the resolution of a map. In degrading the resolution, `ud_grade` sets the value of the superpixel as the mean of the children pixels.
As can be seen in Fig. 5.6, the HAWC point source sky map exhibits an excess of events in the declination range [–30°, –10°] which is not related to known γ-ray sources. Since the HAWC's sensitivity and energy response varies with the source declination, worsening at lower declinations, this excess is mainly due to a worse background estimation in that sky region. In order to reduce the observed excess and avoid to overestimate the neutrino emission, a cut on declination of the HAWC point source $\delta > -20°$ has been applied.
To remove the excess of events in the declination range [–20°, –10°], accounting for the signal strength, different cuts on the HAWC $\sqrt{TS}$ value has been considered. For selecting events corresponding to a specific significance level, the $\sqrt{TS}$ distribution has been converted into a probably density function (normalizing the distribution to the total number of pixels). The 1σ, 3σ and 5σ significance of the hypothesis test distribution have been obtained through a gaussian fit of the $\sqrt{TS}$ distribution region related to the only background hypothesis, as shown in Fig. 5.7 and Fig. 5.8.
The HAWC sky maps corresponding to no $\sqrt{TS}$ cut and 1σ, 3σ and 5σ significance levels are shown in Fig. 5.9 and Fig. 5.10 for the model with $\alpha = -2$ and reference energy $E_0 = 7$ TeV, and in Fig. 5.11 and Fig. 5.12 for $\alpha = -2.7$ and reference energy $E_0 = 1$ TeV.
As highlighted by the above mentioned figures, if a 5σ significance is requested the number of point sources is drastically reduced all over the sky and not only in the region of the observed excess. Since a less stringent cut on $\sqrt{TS}$ allows to reduce the observed excess without lose point sources at higher declinations, the $\sqrt{TS}$ value corresponding to a 3σ significance has been selected as the optimal cuts on the HAWC hypothesis test distribution. Finally, the HAWC sky maps corresponding to a 3σ significance of the hypothesis test distribution for the two different source models have been used as reference maps to determine the neutrino counterpart to the HAWC data and estimate the sensitivity of the ANTARES telescope to such an emission.

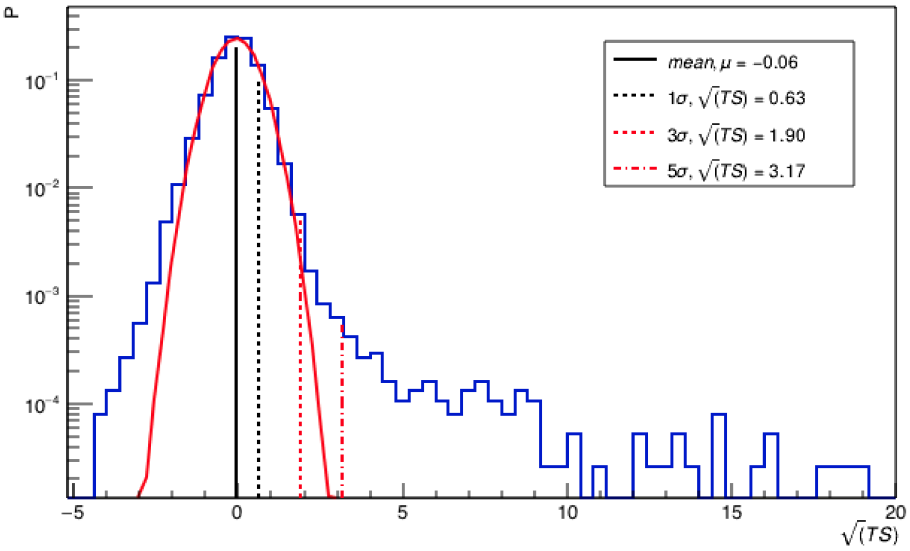

Figure 5.7: Distribution of the $\sqrt{TS}$ of the HAWC test statistic analysis for the HAWC sky map with spectral index α= –2 and reference energy E_0 = 7 TeV. The mean value of the distribution, obtained with a gaussian fit, and the values of $\sqrt{TS}$ corresponding to 1σ, 3σ and 5σ of the distribution are also indicated.

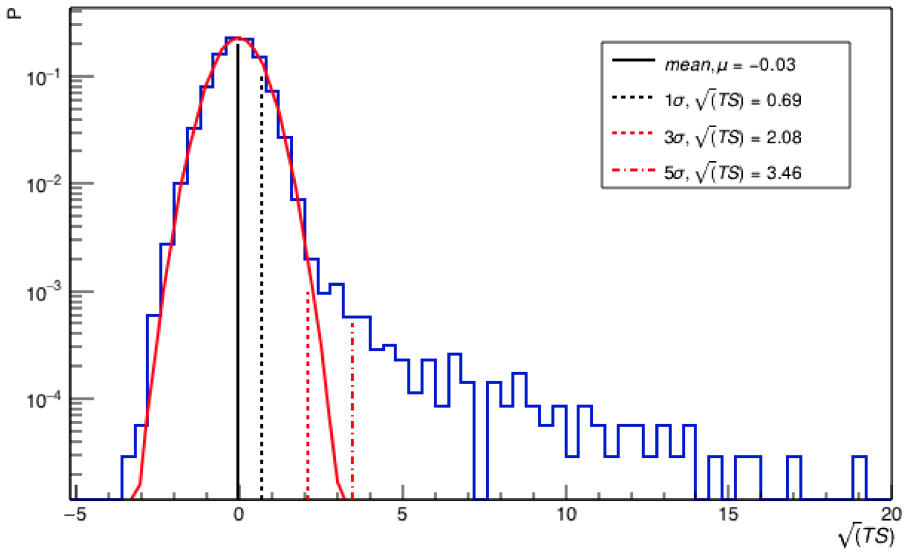

Figure 5.8: Distribution of the $\sqrt{TS}$ of the HAWC test statistic analysis for the HAWC sky map with spectral index α= –2.7 and reference energy E_0 = 1 TeV. The mean value of the distribution, obtained with a gaussian fit, and the values of $\sqrt{TS}$ corresponding to 1σ, 3σ and 5σ of the distribution are also indicated.

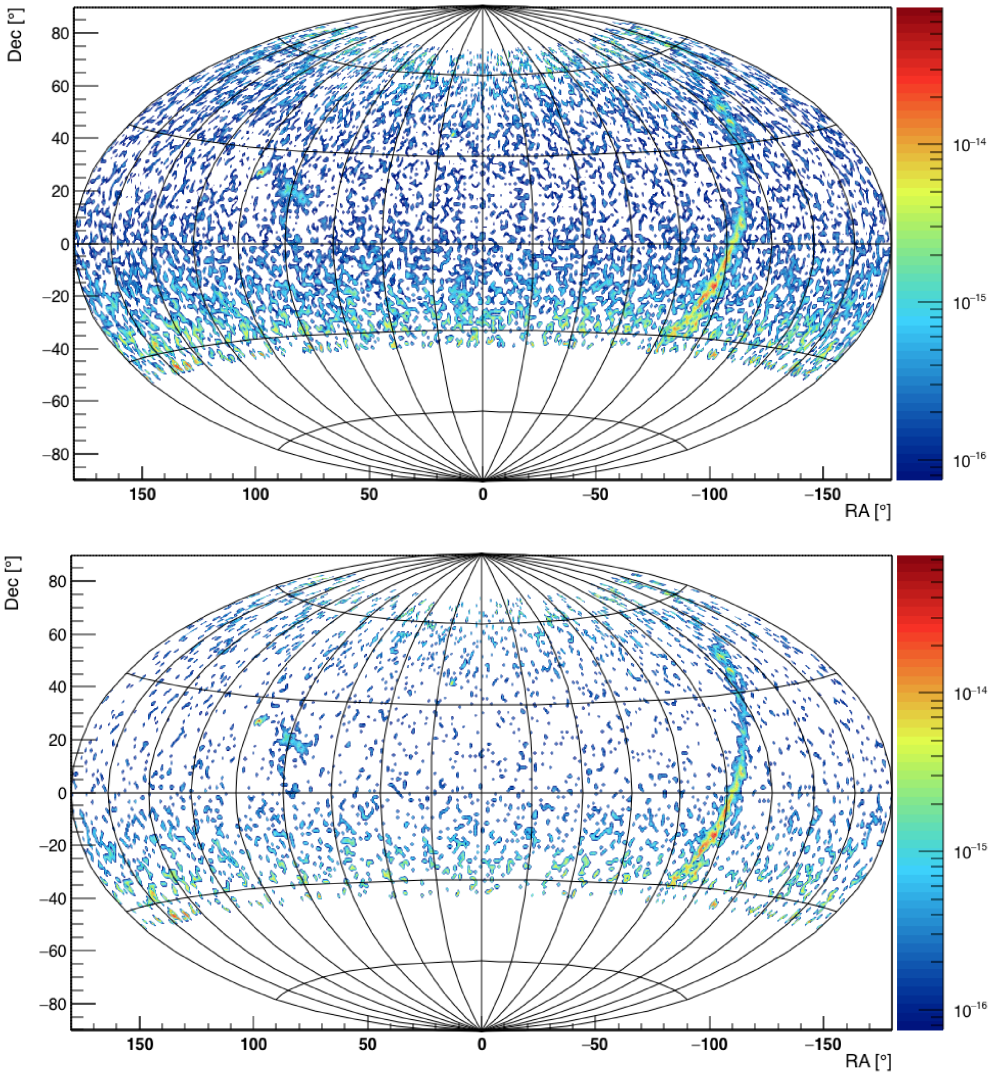

Figure 5.9: HAWC differential flux sky maps, in Aitoff projection, for the model with α= –2 and reference energy E_0 = 7 TeV. The maps are obtained applying a cut on the declination, δ > -20°, no cut (upper panel) and a cut corresponding to 1σ (lower panel) of the hypothesis test distribution respectively. The maps are reported in the equatorial coordinate reference system. The color scale is in $[\text{TeVcm}^2\text{s}]^{-1}$.

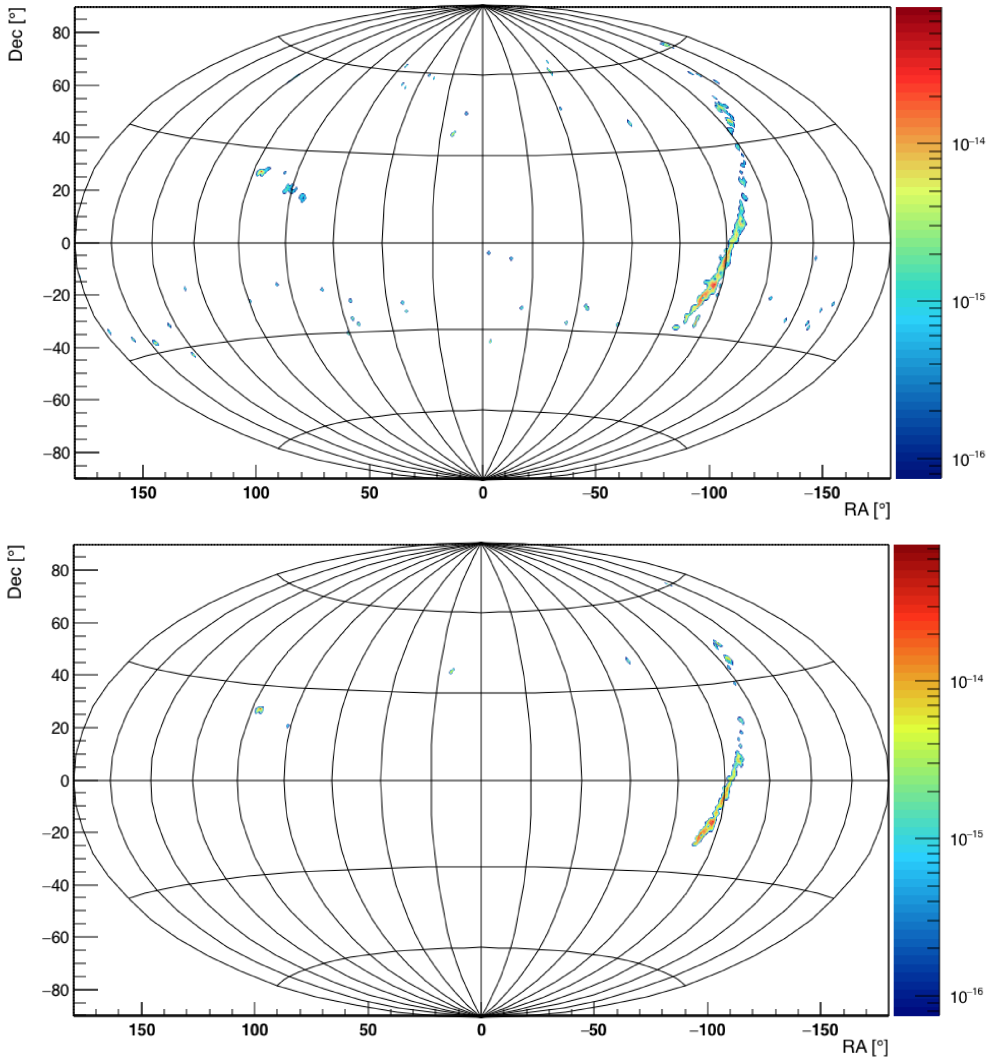

Figure 5.10: HAWC differential flux sky maps, in Aitoff projection, for the model with α= –2 and reference energy E_0 = 7 TeV. The maps are obtained applying a cut on the declination, $\delta >$ -20°, cuts corresponding 3σ (upper panel) and to 5σ (lower panel) of the hypothesis test distribution respectively. The maps are reported in the equatorial coordinate reference system. The color scale is in $[\mathrm{TeVcm^2s}]^{-1}$.

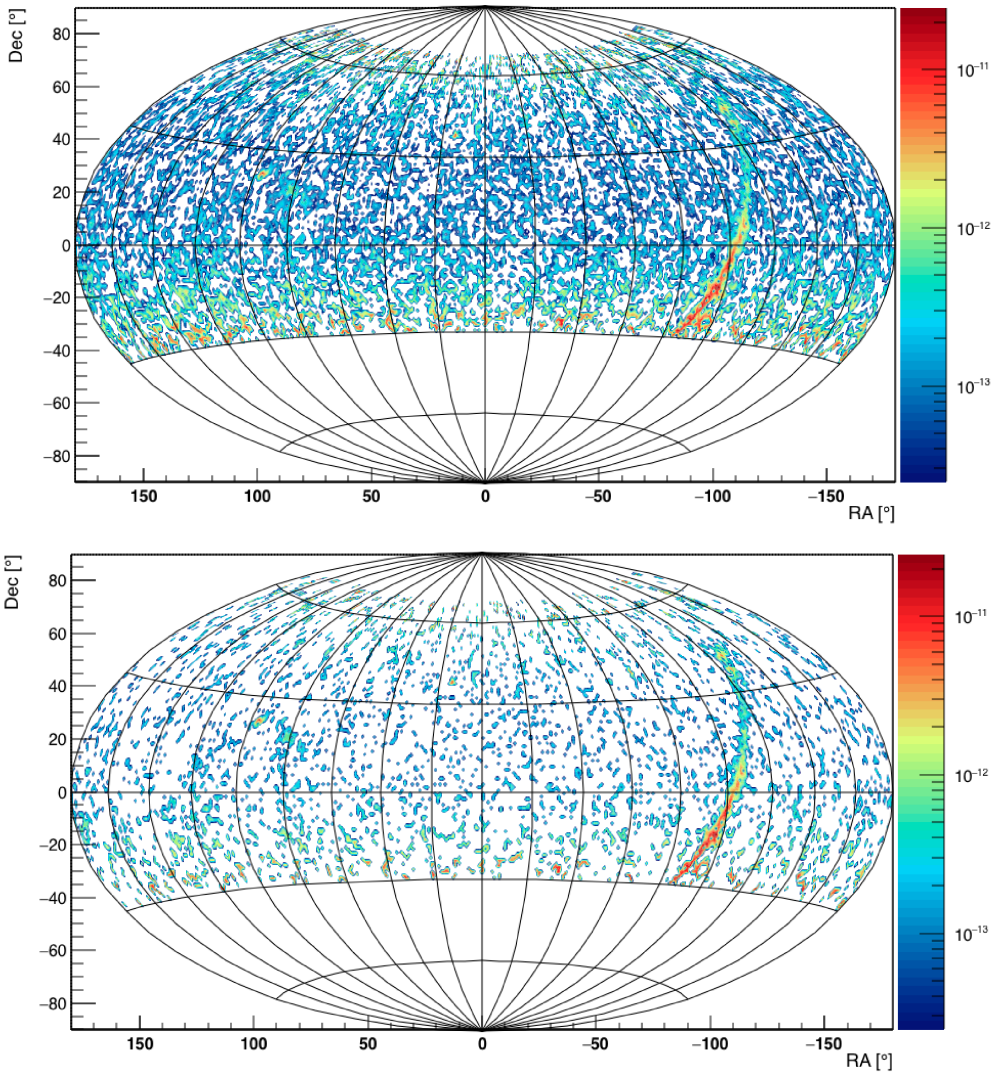

Figure 5.11: HAWC differential flux sky maps, in Aitoff projection, for the model with α= −2.7 and reference energy $E_0 = 1$ TeV. The maps are obtained applying a cut on the declination, $\delta >$ -20°, no cut (upper panel) and a cut corresponding to 1σ (lower panel) of the hypothesis test distribution respectively. The maps are reported in the equatorial coordinate reference system. The z-axis is in $[\text{TeVcm}^2\text{s}]^{-1}$.

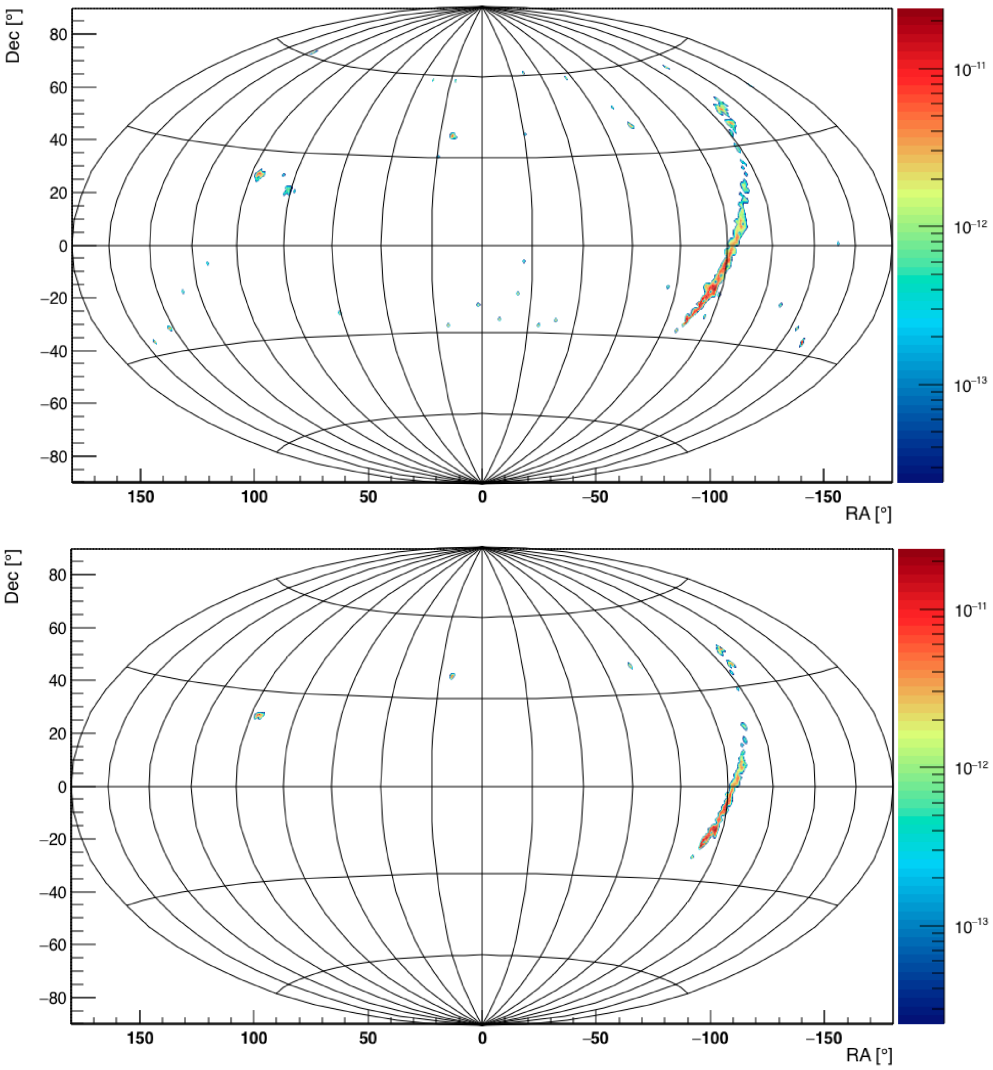

Figure 5.12: HAWC differential flux sky maps, in Aitoff projection, for the model with α= –2.7 and reference energy E_0 = 1 TeV. The maps are obtained applying a cut on the declination, δ > -20°, cuts corresponding 3σ (upper panel) and to 5σ (lower panel) of the hypothesis test distribution respectively. The maps are reported in the equatorial coordinate reference system. The z-axis is in $[\mathrm{TeVcm^2s}]^{-1}$.

5.3.2 ANTARES sky maps

The neutrino counterpart to the HAWC γ-ray sky has been estimated through MC simulations of a diffuse neutrino flux, uniformly distributed all over the sky, which cover the period of ANTARES data taking from 2007 to 2017. For the analysis presented in this thesis only the MC events reconstructed as *track-like* events have been considered. The *shower-like* events will be included in a future extension of this work.
In order to reduce the contribution of background events and to optimise the sensitivity of the ANTARES telescope, an events selection have been performed on the basis of the track quality parameter Λ, the angular error estimate β, on the value of the reconstructed energy estimator ρ, the reconstructed zenith angle $\cos\theta$ and on the reconstructed track length L_μ. The same quality cuts optimised for the previous ANTARES point source analysis have been used, corresponding to $\Lambda > -5.2$, $\cos\theta > -0.1$, $\beta < 1°$, $log_{10}(\rho) > 1.6$, $L_\mu > 380$ m.
Since a one-to-one correspondence between neutrino and γ-ray fluxes is assumed, the sky map of the expected number of reconstructed neutrino events for the considered period of data acquisition is obtained re-weighting the MC neutrino events in each bin of right ascension and declination (pixel) according to the energy spectrum of the reference model of neutrino production

$$W_{event} = w_2 \cdot F_{0,\mathrm{GeV}} \cdot \left(\frac{E}{1\mathrm{GeV}}\right)^{-\alpha} \tag{5.3}$$

In this formula w_2 is the weight of the generated event provided by MC simulations (see sec. 4.2), E is the energy of the event in GeV, $F_{0,\mathrm{GeV}}$ is the value of the differential γ-ray flux of the 3σ significance HAWC sky maps expressed in [GeV^{-1} cm^{-2} s^{-1}] and α is the spectral index of the model. According to Eq. 7.3 the maps of the expected number of reconstructed neutrino events using 10 years of ANTARES data are shown in Fig. 5.13.

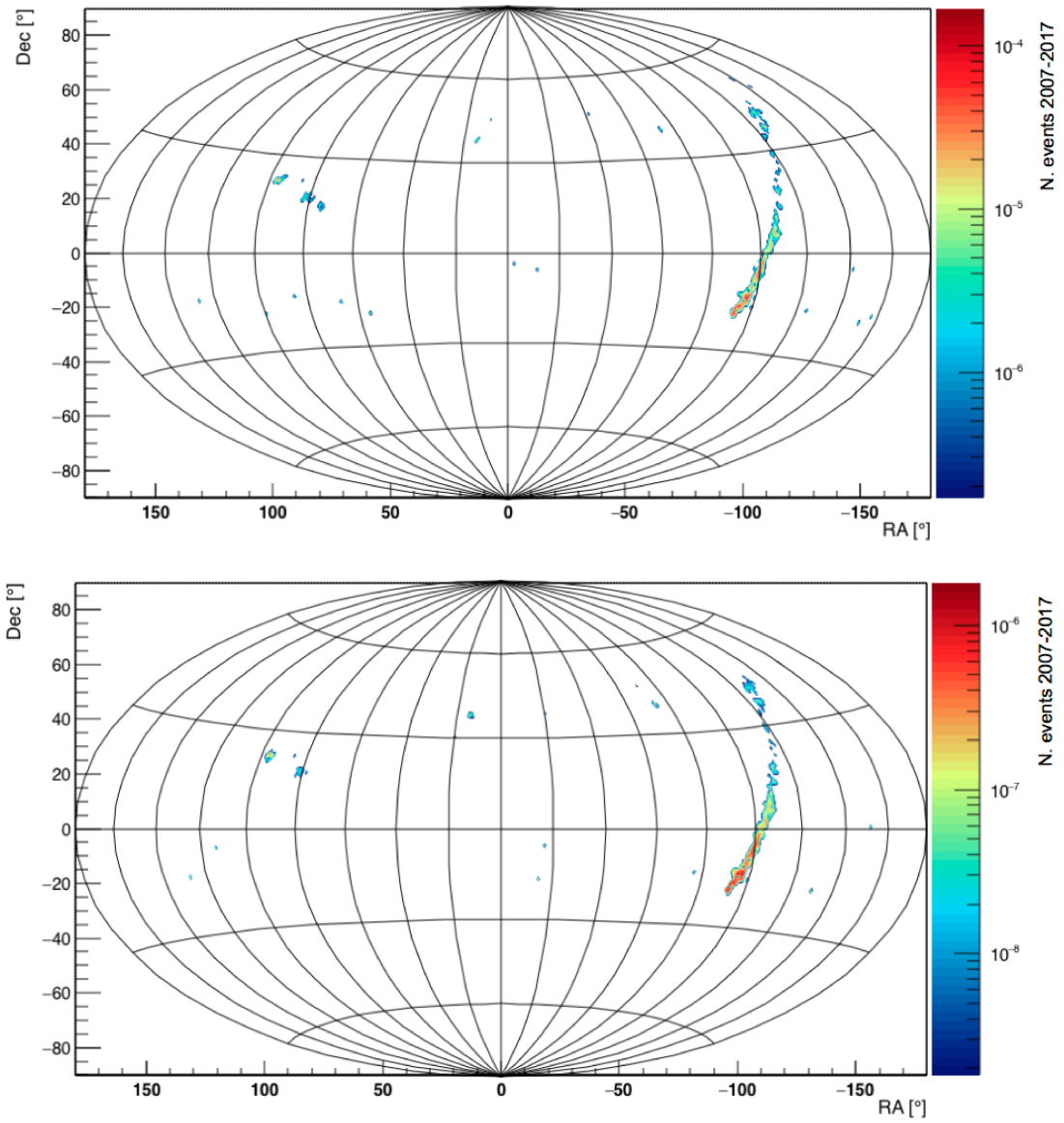

Figure 5.13: Sky maps, in Aitoff projection, of the expected number of reconstructed neutrino events for the period of ANTARES data taking 2007-2017. The upper panel shows the map of neutrino events accounting for a reference model of neutrino production with α= –2 and reference energy E_0 = 7 TeV. In the lower panel the map of neutrino events for a model of neutrino production with α = – 2.7 and reference energy E_0 = 1 TeV is presented. The maps are reported in the equatorial coordinate reference system.

Chapter 6

Search for cosmic neutrinos from the HAWC γ-ray sky

In order to investigate the ANTARES capability to detect the neutrino counterpart of the HAWC γ-ray sky, a search for a neutrino emission from the HAWC point source sky maps presented in sec. 5.3.1 has been performed. The search is based on statistical methods which rely only on signal and background expectations derived from MC simulations, so no bias is introduced by looking at actual data. In particular, the average upper limit, or sensitivity, and the discovery potential of the search have been estimated. The sensitivity is defined as the average upper limit of the neutrino flux $d\Phi_\nu/dE_\nu$ that would be obtained by an ensemble of experiments where no significant signal is observed. The discovery potential is defined as the neutrino flux, $d\Phi_\nu/dE_\nu$, that produces a significance (here 5σ) observation in a fraction of 50% of the hypothetical experiments.
In the analysis presented in this thesis two different searches have been performed:

- a search for a neutrino emission from the point-like sources Markarian 421 and Markarian 501, using both HAWC sky maps as reference models of neutrino production;
- an all-sky point source search, considering as reference model for neutrino production the HAWC sky map with the power law energy spectrum having α=–2.

The searches for neutrino emission have been performed following a maximum-likelihood method. In such method the significance of a cluster of neutrino events is estimated through a hypothesis test based on the likelihood ratio between the maximised value of a likelihood function and its value for the only background hypothesis.
In this chapter, after a brief description of the ANTARES data and MC samples considered in the analysis, a detailed explanation of the maximum likelihood method and of the test statistic definition used to estimate the sensitivity and discovery power of the searches are provided. Finally the results are presented.

6.1 The ANTARES data and Monte Carlo samples

The sensitivity of the search for point-like neutrino sources has been estimated through MC simulations of ν_μ ($\bar{\nu}_\mu$) and $\nu_e(\bar{\nu}_e)$ (CC and NC interactions). The simulations account for the events collected by the ANTARES telescope in the period of time between 2007 and 2017. To consider only periods of good data taking the run-by-run analysis of the official ANTARES data production has been considered, corresponding to a total livetime of $\sim$ 3125.42 days.
For the analyses performed in this thesis the latest ANTARES MC production ($v4$) has been used. The MC sample consists of neutrino events generated in the energy range $10 < E_\nu < 10^8$ GeV and zenith angle $0° < \theta < 180°$. The ν_τ contribution has been extrapolated from the other neutrino channels. In particular the number of ν_μ generated from the CC and NC interactions of ν_τ has been estimated from few MC files calculating the ratios of the acceptances for the different flavours. The same final set of cuts for tracks have been applied.
As described in sec. 4.2, the MC sample has been differently weighted to reproduce the background and signal events. The atmospheric neutrinos have been simulated weighting MC events according to the conventional flux of the Honda et al. model [62] and using the Enberg et al. model [60] to account for the prompt component. The signal neutrinos have been generated weighting the MC events according to the power law energy spectra of the reference model of neutrino production (Eq. 5.3).
Since most of the triggered events detected by a neutrino telescope are due to atmospheric muons, to consider also the contribution of this background component, a detailed simulation of the extensive air showers produced by the interactions of high energy cosmic rays with the particles present in the Earth's atmosphere has been performed, as described in sec. 4.4.
In order to optimise the sensitivity of the search and discriminate signal from background events, an event selection has been performed on the basis of the track quality parameter Λ, the angular error estimate β, on the value of the reconstructed energy estimator ρ, on the reconstructed zenith angle $\cos\theta$ and on the reconstructed track length L_μ. The relation between the logarithm of the MC neutrino energy E_ν and the reconstructed energy estimator ρ for up-going events is shown in the left panel of Fig. 6.1. In the right panel the Λ parameter as a function of the angular resolution for the same events is presented. Cuts on the reconstructed energy estimator ρ correspond to cuts on the true neutrino energy. Since at high energy the cosmic neutrino component dominates over the background of atmospheric neutrinos, quality cuts on the reconstructed energy estimator ρ allow to select signal neutrino events from the atmospheric background. Cuts on the Λ parameter select neutrino events with a better angular resolution. The same quality cuts optimised for the previous ANTARES point-source analysis [95] have been firstly used: $\cos\theta > -0.1$ to select only up-going events, $\Lambda > -5.2$ and $\beta < 1°$ to reject badly reconstructed track (mainly due to atmospheric muons), $log_{10}(\rho) > 1.6$ and $L_\mu > 380$ m to rejectc atmospheric neutrinos. To improve the sensitivity of the all-sky point source search a further optimization of the quality cut on Λ will be performed.

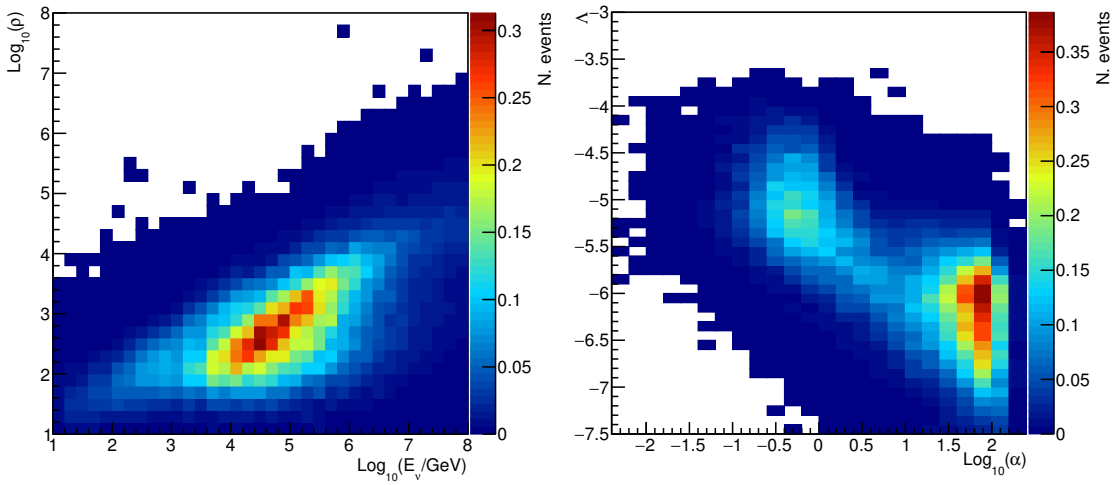

Figure 6.1: On the left panel the relation between the logarithm of the MC neutrino energy E_ν and the reconstructed energy estimator ρ for up-going events is shown. In the right panel the Λ parameter as a function of the angular resolution is presented.

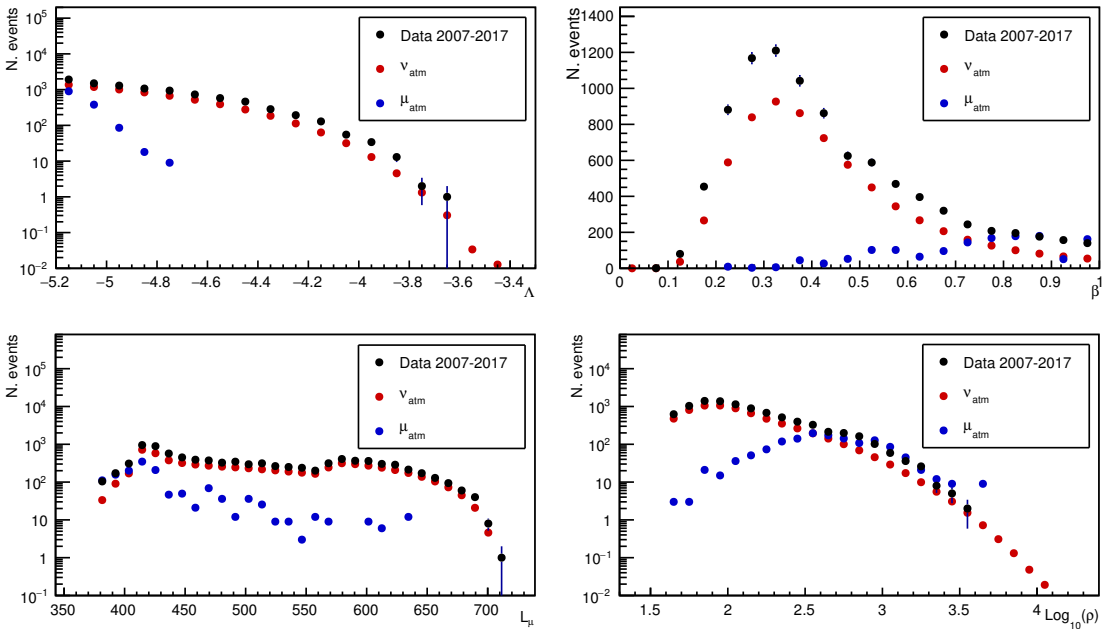

Figure 6.2: Comparison between data and MC events as a function of the track quality parameter Λ (upper left panel), the angular error estimate β (upper right panel), the reconstructed track length L_μ (lower left panel) and the value of the reconstructed energy estimator ρ (lower right panel). The error bars account only for statistical errors. The cuts reported in the text have been appled.

To avoid biases in the event selection, the analysis followed a blind policy, according to which the events selection is optimised only on the Monte Carlo events, considering 10% of the data to check the agreement with simulations. A comparison between data and simulated MC events after the quality cuts selection is shown in Fig. 6.2. As can be seen in these plots, applying the over mentioned quality cuts a discrepancy of about $\sim$20% between data and MC exists.

6.2 Search method for point-like neutrino sources

The capability of the ANTARES detector to identify the neutrino flux emitted by point-like sources is here investigated using a maximum-likelihood approach. The maximum-likelihood method searches for accumulations of neutrino events from a specific location in the sky respect to the expected background, which is uniformly distributed all over the sky. In order to estimate the significance of the candidate signal cluster a hypothesis test, based on a maximum-likelihood ratio between the maximised value of a likelihood function and its value for the only background hypothesis, is built.
Since in the maps of the expected number of reconstructed neutrino events (see Fig. 5.13) a clustering of events around the position of Markarian 421 ($\alpha = 166.08°$, $\delta = 38.19°$) and Markarian 501 ($\alpha = 253.46°$, $\delta = 39.76°$) is present, in this work the ANTARES sensitivity and the discovery potential to such emissions are estimated. Furthermore, the sensitivity and discovery potential of the full-sky point source search will be also investigated.

6.2.1 Likelihood maximization and test statistic definition

The maximised value of the likelihood function is here estimated using the maximum-likelihood method. If a random variable x is distributed according to a probability density function $f(x;\theta)$, with a known functional form and at least one unknown parameter θ, the maximum-likelihood method is a technique for estimating the values of such parameter given a finite sample of data.
In fact, under the assumption of the hypothesis $f(x;\theta)$ and after n independent measurements of the variables x, the probability that x_i is measured in the range $[x_i,\, x_i + dx_i]$ for all i is

$$\prod_{i=1}^{n} f(x;\theta) \cdot dx_i \tag{6.1}$$

If the considered probability density function and parameter values are close to the true value, the data have a high probability to be actually measured.
Since the dx_i does not depend on the parameter θ the same dependence is also true for the function

$$\mathcal{L}(\theta) = \prod_{i=1}^{n} f(x;\theta) \tag{6.2}$$

with $\mathcal{L}$ called *Likelihood function* and the maximum likelihood estimators for the parameter is that one which maximises $\mathcal{L}$. In the analysis presented here the number of signal

events is the only free parameter. Hence, in this case the maximum likelihood estimator returns the number of signal events, n_s, which maximised the likelihood function.
Under the hypothesis that the data sample includes both signal and background events, the likelihood function used for the point-like source search is defined as

$$\mathcal{L}_{sig+bkg} = \prod_i [\mu_{sig} \cdot pdf_{sig}(E_i, \alpha_i, \delta_i) + \mu_{bkg} \cdot pdf_{bkg}(E_i, \delta_i)] \tag{6.3}$$

where E_i is the reconstructed energy, α_i and δ_i are the right ascension and declination, and θ_i is the zenith angle of the event i. In the previous formula μ_{sig} is the number of signal events and it is obtained maximising the likelihood function, while μ_{bkg} corresponds to the total number of background events. Since at present the ANTARES sensitivity has been estimated considering only tracks, for such event topology the probability density functions of being a signal or a background event are defined as

$$pdf_{sig}(E_i, \alpha_i, \delta_i) = \mathcal{M}_{sig}(\alpha_i, \delta_i) \cdot \mathcal{E}_{sig}(E_i, \alpha_i, \delta_i) \tag{6.4}$$

$$pdf_{bkg}(E_i, \theta_i, \delta_i) = \mathcal{M}_{bkg}(\delta_i) \cdot \mathcal{E}_{bkg}(E_i, \delta_i) \tag{6.5}$$

In such a definition the $\mathcal{M}$ distributions are the probability density functions to reconstruct an event in a given position in the sky. In particular, the signal distributions $\mathcal{M}_{sig}$, which depend on the differential neutrino flux predicted by the reference models, are derived from MC simulations. Whereas, the $\mathcal{M}_{bkg}$ are obtained from data by scrambling the time of events, which results in a randomization of the corresponding right ascension. The $\mathcal{E}$ are the probability density functions to reconstruct an event with energy E and also in this case are derived from MC simulations. The signal $\mathcal{E}_{sig}$ depends on the equatorial coordinates, while the background energy distribution $\mathcal{E}_{bkg}$ depends only on the declination δ_i.
Despite the maximum likelihood method returns the most likely number of neutrino events of the cluster, it does not allows to make assumption about the significance of the observation. For this reason a test statistic variable, $\mathcal{Q}$, is defined to perform a likelihood ratio test

$$\mathcal{Q} = -2 \log \frac{\mathcal{L}_{bg}}{\mathcal{L}_{max}} = 2(\log \mathcal{L}_{max} - \log \mathcal{L}_{bkg}) \tag{6.6}$$

where $\mathcal{L}_{max} = \mathcal{L}_{sig+bkg}$. In the likelihood ratio test two opposite hypothesis are considered. The null hypothesis H_0, which corresponds to the case where only background events are presents, $n_s = 0$, and the alternative hypothesis H_1, corresponding the case $n_s > 0$. In Fig. 6.3 an example of the test statistic distributions corresponding to the H_0 and H_1 hypotheses are shown. As seen from the figure, the significance of the observation is given by

$$\alpha = \int_{\mathcal{Q}_{cut}}^{+\infty} f(\mathcal{Q}|H_0) d\mathcal{Q} \tag{6.7}$$

where $\mathcal{Q}_{cut}$ is the threshold value of the test statistic distribution used to evaluate the desired significance level. Therefore, the significance is given by the area of the H_0 distribution over test statistic threshold value $\mathcal{Q}_{cut}$. The power (or p-value) is defined by the area of the H_1 distribution over the threshold value $\mathcal{Q}_{cut}$.

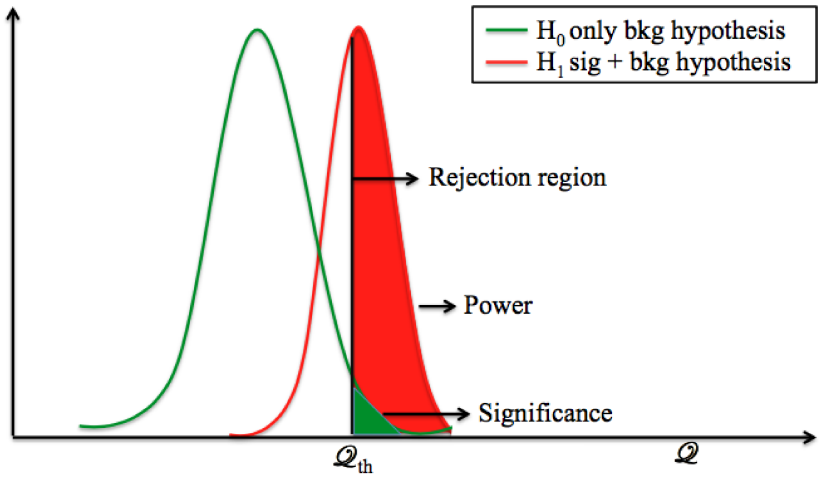

Figure 6.3: Example of hypothesis test distributions. The green (red) curve corresponds to the $\mathcal{Q}$ distribution for the H_0 (H_1) hypothesis. The significance is given by the area of the H_0 distribution over test statistic threshold value, $\mathcal{Q}_{cut}$. The power is defined by the area of the H_1 distribution over the threshold value $\mathcal{Q}_{cut}$.

6.2.2 Construction of the likelihood functions

In order to discriminate signal from background events the pdf_{sig} and pdf_{bkg} should have functional forms as much different as possible. This characteristic is well represented by the *pdf*s to reconstruct an event at a distance α_{rec} from the source, because signal and background events have different probability to be reconstructed at a certain angular distance from the source position in the sky, and by the *pdf*s to reconstruct an event with a specific energy value, because it takes care of the different spectral energy distribution of signal and background events in the energy range of interest for ANTARES.

Point Spread Function and Background Rate

The probability to reconstruct an event at a distance α_{rec} from the source is named Point Spread Function (PSF). The distribution of the PSFs as a function of the angle between the reconstructed direction and the source direction, α_{rec}, of the simulated neutrino events represent the *pdf* to reconstruct a signal event in a given position in the sky, $\mathcal{M}_{sig}$. The PSFs depend on the differential neutrino flux predicted by the reference neutrino model and are derived from MC simulations. In Fig. 6.4 the $dP(dlog(\alpha))/\mathrm{d}\Omega$

distribution for the signal events with a power law spectra E^{-2} is shown.

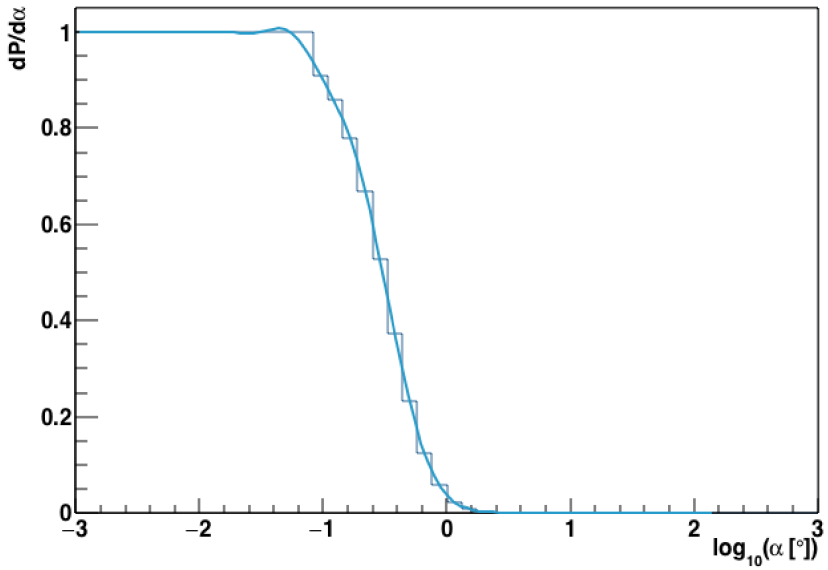

Figure 6.4: The point spread function (PSFs) distribution as a function of the reconstructed angle, α_{rec}, for simulated signal events with a power law energy spectra E^{-2}. The cyan line shows the parametrisation used in the likelihood fit.

The *pdf*s of the background events $\mathcal{M}_{bkg}(\delta_i)$ are the so-called Background Rates and represent the number of selected events as a function of the sine of the declination, $(1/2\pi)\cdot dN(\delta)/d\sin(\delta)$, as shown in Fig. 6.5. For the blind analysis presented here, this probability density function is simply obtained randomising the right ascension of the events of the ANTARES data sample.

Reconstructed energy probability density functions

In the TeV energy range the atmospheric neutrinos have a softer energy spectra than the astrophysical neutrinos with a different probabilities to be reconstructed. In this analysis the reconstructed energy is used as energy estimator to discriminate between signal and background events by exploiting the difference in the energy spectrum. The energy dependence of the likelihood functions is taken into account through the *pdf*s to reconstruct an event with a given energy value, $\mathcal{E}$. For the signal events, $\mathcal{E}_{sig}$ depends on the equatorial coordinates and it has been obtained weighting the MC event according to the power law energy spectrum of the reference model of neutrino emission. Instead, the background energy distribution $\mathcal{E}_{bkg}$ depends only on the declination δ_i and it has been derived weighting the MC events with the Honda et al and the Enberg et al. models.

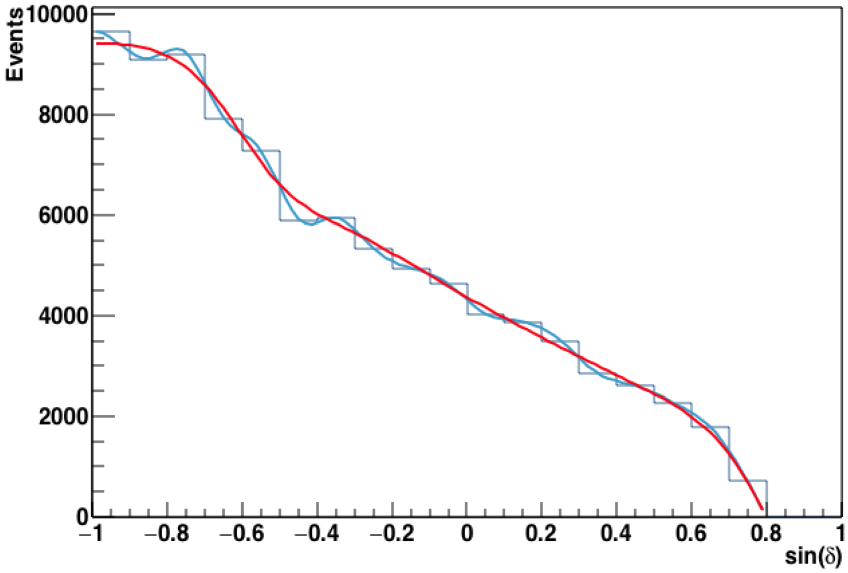

Figure 6.5: Distribution of the sine of the declination for the selected events. The blue line shows the parametrisation used in the likelihood computation. The red line shows a second parametrisation used to assign the systematic uncertainty on the background rate.

6.2.3 Pseudo-experiments

In order to derive the test statistic distributions corresponding to the different hypotheses, H_0 and H_1, a wide number of simulations have been performed using data sets of randomly generated events, the so called *pseudo-experiments*. In each pseudo-experiment a randomised set of data, representing the original data sample, is used to compute the *pdf*s of the likelihood functions and build the hypothesis test. This procedure is preliminary to the unblinding of the final set of data to avoid biases in the analysis.
At this stage of the analysis signal and background events are simulated through different procedure. The location of signal events is extracted from the source position in the sky. The event distance to the centre of the source is generated randomly from the PSFs, which account for the angular distance between the reconstructed and the original neutrino direction. Since the background is expected to be distributed uniformly over the sky, the right ascension of background events is generated by assuming a uniform distribution between 0° and 360°. While, the declination is generated randomly considering the same declination dependent of the original sample of data.
In order to compute the hypothesis test for the point-like source search, for each analysed source 10^4 pseudo-experiments are simulated by varying the number of signal events n_s coming from the source location.
In each pseudo-experiment a clustering algorithm identifies potentially significant clusters of events within a cone of 10 degrees diameter around the source position. Then, for each selected cluster, the mean number of signal events is estimated through the maximum likelihood method above mentioned. This entire procedure is repeated varying the

number of signal events in the range [0, 50] with 1 events step.
Since the number of signal events is expected to follow a Poisson distribution, a transformation to calculate the test statistic distribution for a mean number of signal events μ_s is done according to

$$\frac{dP(\mu_s)}{d(\mathcal{Q})} = \sum_i^N \frac{dP(n_i)}{d(\mathcal{Q})}\ P(n_i|\mu_s) \tag{6.8}$$

where N is the maximum number of signal events, $\frac{dP(n_i)}{d(\mathcal{Q})}$ is the test statistic distribution for a fixed number of signal events n_i, and $P(n_i|\mu_s)$ is the Poisson probability to detect n_i events given a mean number μ_s of events. The systematic on the number of detected events is taken into account by means of a Gaussian smearing

$$\frac{dP(\mu_s)}{d(\mathcal{Q})} = \sum_i^N \frac{dP(n_i)}{d(\mathcal{Q})}(n_i|\bar{\mu})\ G(\bar{\mu}|\mu_s, \sigma_\mu)d\bar{\mu} \tag{6.9}$$

where σ_μ is the uncertainty on the mean number of signal events, and $\bar{\mu}$ is a variable which ranges between $[\mu_s - 4\sigma_\mu,\ \mu_s + 4\sigma_\mu]$.

6.2.4 Acceptance and effective area

Usually, in order to compare the results with other experiments and derive the corresponding discovery flux or the upper limit on the source spectrum, the number of neutrino events is converted into the flux arriving to the Earth. Given a specific source flux $d\Phi/dE_\nu dtdS$, the number of expected events is calculated as

$$N_{event}(\delta) = \int\int \frac{d\Phi}{dE_\nu dtdS} A_{eff}(E_\nu, \theta_\nu) dE_\nu dt \tag{6.10}$$

where $A_{eff}(E_\nu, \theta_\nu,)$ is the effective area (i.e, the equivalent area of a detector with perfect efficiency) obtained from Monte Carlo simulations. The $A^\nu_{eff}(E_\nu, \theta_\nu)$ for $\nu + \bar{\nu}$ (NC e CC) events computed with same final cuts of the analysis is shown in Fig. 6.6. The flux of a source is commonly assumed to follow a power law $d\Phi/dE_\nu dtdS = \Phi_0(E_\nu/E_0)^{-\gamma}$, where Φ_0 is a normalisation constant. In ANTARES analyses, the magnitude which connects the number of expected events with a given flux Φ_0 is called acceptance, $A(\delta)$, and it is defined as

$$A(\delta) = N_{event}(\delta)/\Phi_0 \tag{6.11}$$

The acceptances used for the analyses presented in this work have been computed considering a normalization factor equal to 10^{-8} [GeV cm^2 s]$^{-1}$. In Fig. 6.7 the acceptance computed for a E^{-2} spectrum is shown as a function of the sine of the declination.

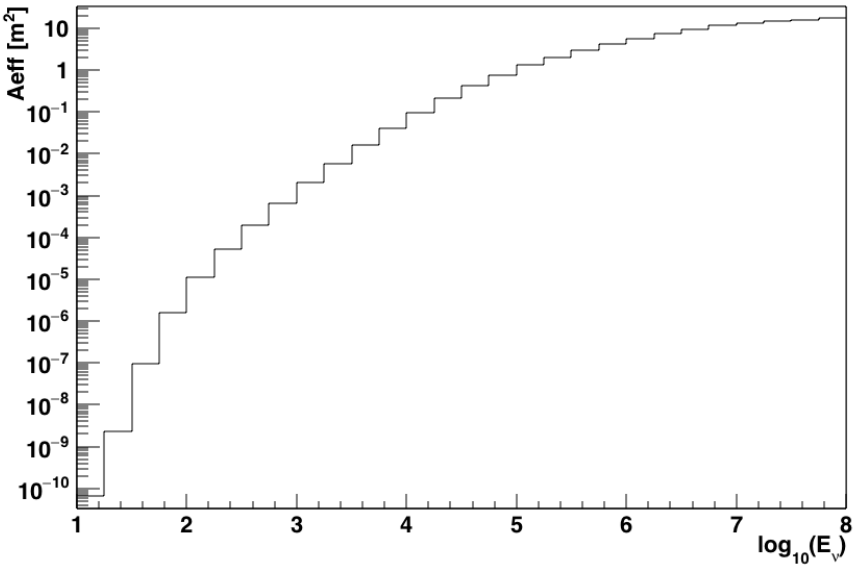

Figure 6.6: Effective area for $\nu + \bar{\nu}$ (NC e CC) events of the ANTARES detector as a function of the neutrino energy. The effective area was computed taken into account the neutrino power law energy spectra E^{-2}, used to evaluated the neutrino sky map counterpart of the HAWC γ-ray sky map, and the following quality cuts: cos$\theta > -0.1$, $\Lambda > -5.2$, $\beta < 1^\circ$, $log_{10}(\rho) > 1.6$ and $L_\mu > 380$ m.

6.2.5 Discovery potential and average upper limit

It is common to estimate the discovery potential and the sensitivity in terms of the true number of signal events n^{true} which leads to such observations. Both these estimations are performed in this work using the test statistic distributions obtained from pseudo experiments after the transformations given in Eq. 8.15, but following two different approaches described below.

Discovery potential

A discovery is claimed when the test statistic $\mathcal{Q}$ exceeds a critical value $\mathcal{Q}_{cut}$ determined from the test statistic distribution for the background only hypothesis H_0. The critical region is chosen such that the probability for $\mathcal{Q}$ to be observed there, under the assumption of the background only hypothesis, is some value α called the *significance level* or *P-value* of the test.

$$\alpha = \int_{\mathcal{Q}_{cut}}^{+\infty} f(\mathcal{Q}|H_0) d\mathcal{Q} \tag{6.12}$$

Common values for the significance levels of two sided gaussian probability are $\alpha = 2.7{\cdot}10^{-3}$ and $\alpha = 5.7{\cdot}10^{-7}$, also known as 3σ and 5σ significance levels respectively. The threshold value, $\mathcal{Q}_{th}$ which leads to a 3σ and 5σ discovery, is obtained from a fit performed over the distribution of test statistic $\mathcal{Q}$ for the only background hypothesis, as show in

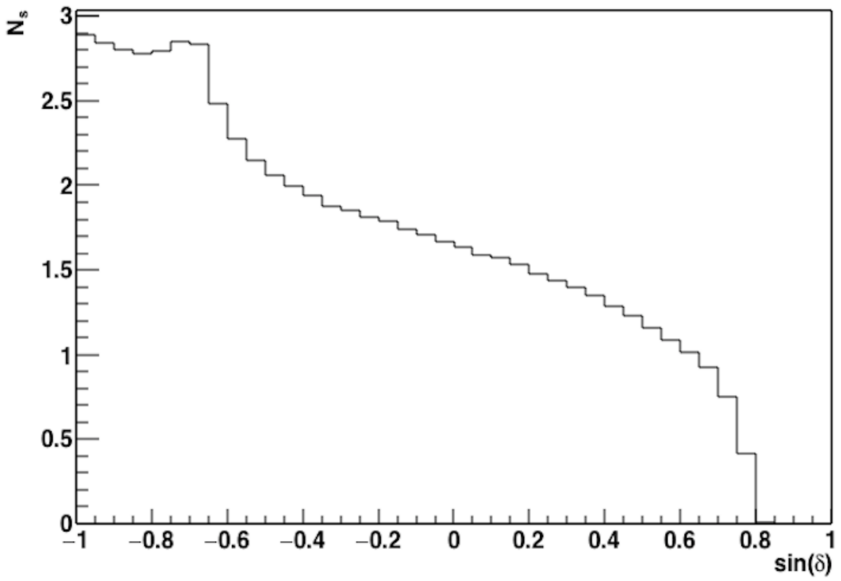

Figure 6.7: Acceptance of the ANTARES detector as a function of the sine of the declination of reconstructed events. The acceptance refers to the neutrino power law energy spectra E^{-2} used to evaluated the neutrino sky map counterpart of the HAWC γ-ray sky map.

Fig. 6.8. According to the Wilk's theorem [146], under the assumption that the null hypothesis is true, the distribution of the test statistic for the only background follows a χ^2 distribution with N degrees of freedom, where N is the number of parameters fitted in the likelihood maximisation. The only free parameter of the likelihood maximisation considered in this work is the number of signal events, n_s, therefore the test statistic distribution for the only background case is fitted by a χ^2 distribution with one degree of freedom and a free normalisation.
In order to estimate the number of events which lead to a 3σ and a 5σ discovery, the $P_{\alpha=3\sigma}$ and $P_{\alpha=5\sigma}$ significance levels of the test statistic distributions of the simulated pseudo-experiments for different number of signal events are computed, as shown in the upper panel of Fig 6.9. Finally, the number of events which lead to a 3σ and a 5σ discovery is given by the number of events which corresponds to a significance of 3σ and 5σ in a fraction of 50% of the hypothetical experiments respectively, as presented in the lower panel of Fig. 6.9. The fluxes necessary to declare a 3σ and 5σ discovery are then obtained through the following proportions

$$\Phi_{3\sigma} = \Phi_{ref.model} \cdot \frac{n_{3\sigma}}{n} \tag{6.13}$$

$$\Phi_{5\sigma} = \Phi_{ref.model} \cdot \frac{n_{5\sigma}}{n} \tag{6.14}$$

where n is the number of expected neutrino event related to a reference neutrino spectra

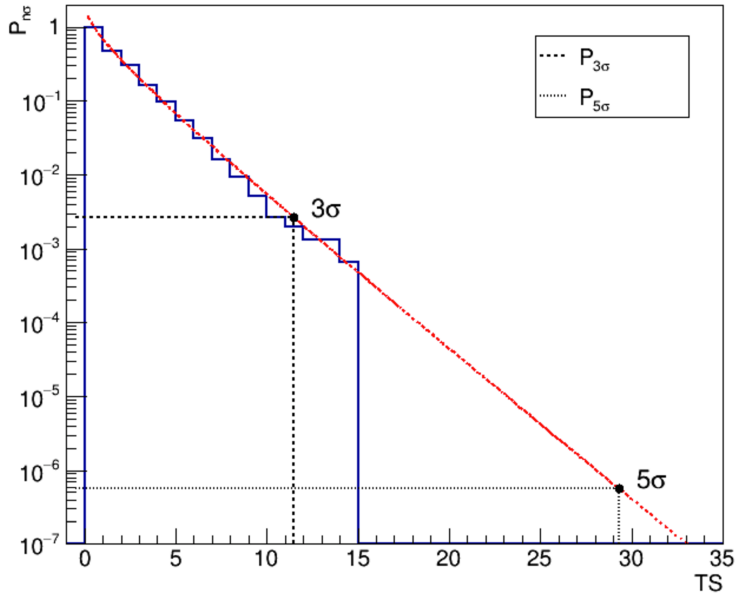

Figure 6.8: The anticumulative distribution of the test statistic for the only background case, fitted by a χ^2 distribution with one degree of freedom and a free normalisation. The threshold values $\mathcal{Q}_{th}$ which leads to a 3σ and 5σ discovery are also indicated.

$\Phi_{ref.model}$. In order to derive the discovery fluxes, in this work the number of neutrino event n has been derived from the acceptances of the analyses which account for a reference neutrino spectra $\Phi_{ref.model} = 10^{-8}$ [GeV cm^2 s]$^{-1}$.

Sensitivity

In order to evaluate the sensitivity of the analysis the frequentist approach proposed by Neyman [147, 148] has been used. The aim is to obtain an interval [n_a, n_b] which includes the number of signal events related to the given observation, n^{true}, within a given confidence level (CL) α

$$P(n^{true} \in [n_a, n_b]) = \alpha \tag{6.15}$$

which means that the range [n_a, n_b] contains the n^{true} with a probability α. However, since it is not possible to directly measure the true number of signal event, intervals of a physical parameter which depends on n^{true} are used. These intervals are named confidence belts, and are defined as

$$P(x \in [x_a, x_b] | n^{true}) = \alpha \tag{6.16}$$

where x is the physical parameter related to n^{true}, and $[x_a, x_b]$ is the corresponding interval. Different options to construct the $[x_a, x_b]$ range are possible. The one used in

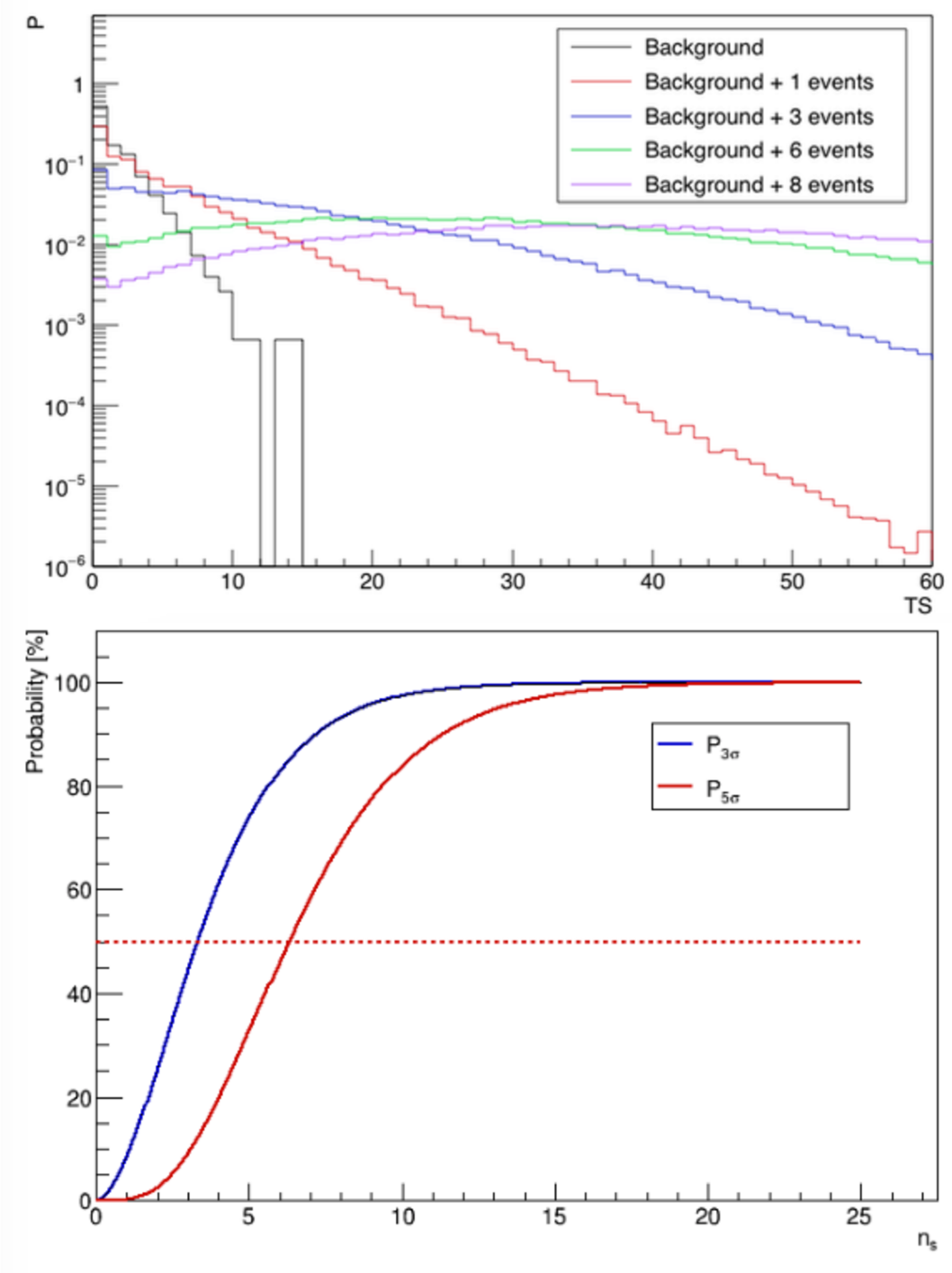

Figure 6.9: In the upper panel the distributions of the test statistic of the simulated pseudo-experiments for $n_s = 0$, 1, 3, 6, 8 are shown. In the lower panel the $P_{\alpha=3\sigma}$ and $P_{\alpha=5\sigma}$ significance levels as a function of the number of observed events are reported. The number of events which lead to a 3σ and a 5σ discovery corresponds to the number of events with a significance of 3σ and 5σ in a fraction of 50% of the hypothetical experiments.

this analyses corresponds to

$$P(x < x_a | n^{true}) = 1 - \alpha \tag{6.17}$$

which are usually known as Neyman upper limits. In order to be reasonably confident that the interval contains the true value n^{true}, the probability α is chosen large enough. In this analysis a CL $\alpha = 0.9$ has been used. The sensitivity is here defined as the upper limit which would be obtained if the observed result would be the median of the background only case. However, the median value of the test statistic distribution for the only background case is not always easy to calculate and it depends on the boundary chosen for the values of the fitted number of signal events n_s in the likelihood maximisation procedure. The simplest boundary to chose corresponds to $0 \leq n \leq n_{max}$, with n_{max} the maximum number of signal events within the search cone used in the likelihood maximization. However, if this boundary is considered more than 50% of the pseudo experiments have a $\mathcal{Q}$ value which is exactly 0 and the median of the $\mathcal{Q}$ distribution can not be determined. Therefore, in order to calculate the median value of the test statistic distribution for the only background, the approach already used in the previous ANTARES point source analysis has been followed. In this approach the minimum of the bound for the values of the fitted number of signal events n_s is set to $n_{min} = 10^{-3}$. This procedure allows to obtain a negative value for the maximum of the likelihood when under fluctuations of the signal are observed, making possible the calculation of the median for the background distribution. Then, in order to make the calculation of the median easier, the test statistic distributions are derived performing the following transformation

$$\mathcal{Q}^{new} = \log_{10}(\mathcal{Q} + K) \tag{6.18}$$

with K a constant value equals to the minimum of the bound, n_{min}.

6.3 Result

6.3.1 Markarion421 and Markarian501

The results of the searches for a neutrino emission from the point-like sources Markarian 421 and Markarian 501 are here presented. In these searches the power law energy spectrum of the HAWC point source γ-ray sky maps is assumed as reference model of neutrino production. In order to investigate the ANTARES capability to detect such emissions, the upper limits with a 90% C.L. on the number of true events $n_{90\%}$ has been estimated according to the Neyman approach. The upper limits is then transformed into a sensitivity flux by considering the proportionality relation between the number of expected events, n_0, and the reference flux, Φ_0, as

$$\Phi_{90\%} = \frac{n_{90\%}}{n_0} \Phi_0 \tag{6.19}$$

with the number of expected events n_0 estimated from the acceptances of the analyses. The number of neutrino events which leads to a 5σ discovery over the considered period

of ANTARES data acquisition has been also estimated.
The sensitivities at 90% C.L. and the 5σ discovery potentials for the two selected sources, together with the assumed model of neutrino emission derived from the HAWC sky maps and the number $n_{90\%}$ and $n_{5\sigma}$ of neutrino events are reported in Tab. 6.1 and Tab. 6.2. The results are showed in Fig. 6.10. The searches for a neutrino emission from the

	$\Phi_{\rm HAWC}$[GeV cm^{2}s]$^{-1}$	$n_{90\%}$	$\Phi_{90\%}$[GeV cm^{2}s]$^{-1}$	$n_{5\sigma}$	$\Phi_{5\sigma}$[GeV cm^{2}s]$^{-1}$
Mrk421	$1.09 \cdot 10^{-10}$	4.56	$4.48 \cdot 10^{-8}$	2.62	$2.57 \cdot 10^{-8}$
Mrk501	$2.4 \cdot 10^{-10}$	4.51	$4.43 \cdot 10^{-8}$	2.66	$2.61 \cdot 10^{-8}$

Table 6.1: In the table the upper limits $n_{90\%}$ and the number of events $n_{5\sigma}$ which lead to 5σ discovery in a fraction of 50% of the hypothetical experiments are reported if a model of neutrino emission $d\Phi/dE_\nu = \Phi_0(E_\nu/7\text{TeV})^{-2}$ is considered. The assumed neutrino fluxes $\Phi_{\rm HAWC}$ derived from the HAWC sky map, the average upper limit $\Phi_{90\%}$ and the discovery flux $\Phi_{5\sigma}$, in [GeVcm^{2}s]$^{-1}$ at the reference energy $E_0 = 1$ GeV, are also reported.

	$\Phi_{\rm HAWC}$[GeV cm^{2}s]$^{-1}$	$n_{90\%}$	$\Phi_{90\%}$[GeV cm^{2}s]$^{-1}$	$n_{5\sigma}$	$\Phi_{5\sigma}$[GeV cm^{2}s]$^{-1}$
Mrk421	$6.13 \cdot 10^{-7}$	7.46	$1.44 \cdot 10^{-4}$	3.57	$6.69 \cdot 10^{-5}$
Mrk501	$5.88 \cdot 10^{-7}$	7.1	$1.44 \cdot 10^{-4}$	3.66	$7.13 \cdot 10^{-5}$

Table 6.2: In the table the upper limits $n_{90\%}$ and the number of events $n_{5\sigma}$ which lead to 5σ discovery in a fraction of 50% of the hypothetical experiments are reported if a model of neutrino emission $d\Phi/dE_\nu = \Phi_0(E_\nu/1\text{TeV})^{-2.7}$ is considered. The assumed neutrino fluxes $\Phi_{\rm HAWC}$ derived from the HAWC sky map, the average upper limit $\Phi_{90\%}$ and the discovery flux $\Phi_{5\sigma}$, in [GeVcm^{2}s]$^{-1}$ at the reference energy $E_0 = 1$ GeV, are also reported.

point-like sources Markarian 421 and Markarian 501 allow to set an average upper limit which is almost two order of magnitude higher than the predicted neutrino fluxes.
The ANTARES sensitivity to a neutrino emission from point-like cosmic neutrino sources has been already investigated and presented in [95]. In the point-like source search all flavor neutrino interactions have been considered, using the data collected between 2007 and the end of 2015, and a generic E^{-2} energy spectrum has been used to model the cosmic neutrinos flux. A comparison between the results reported in [95] and the sensitivity of the search for a neutrino emission from the two point-like sources presented in this thesis has been performed. A difference between the two limits of about 20% has been found. Even if the analysis presented here account for two more years of ANTARES data taking, the better value obtained in [95] is mainly due to a different MC production used to perform the point-like source search. The differences between the two MC productions are currently under investigations.

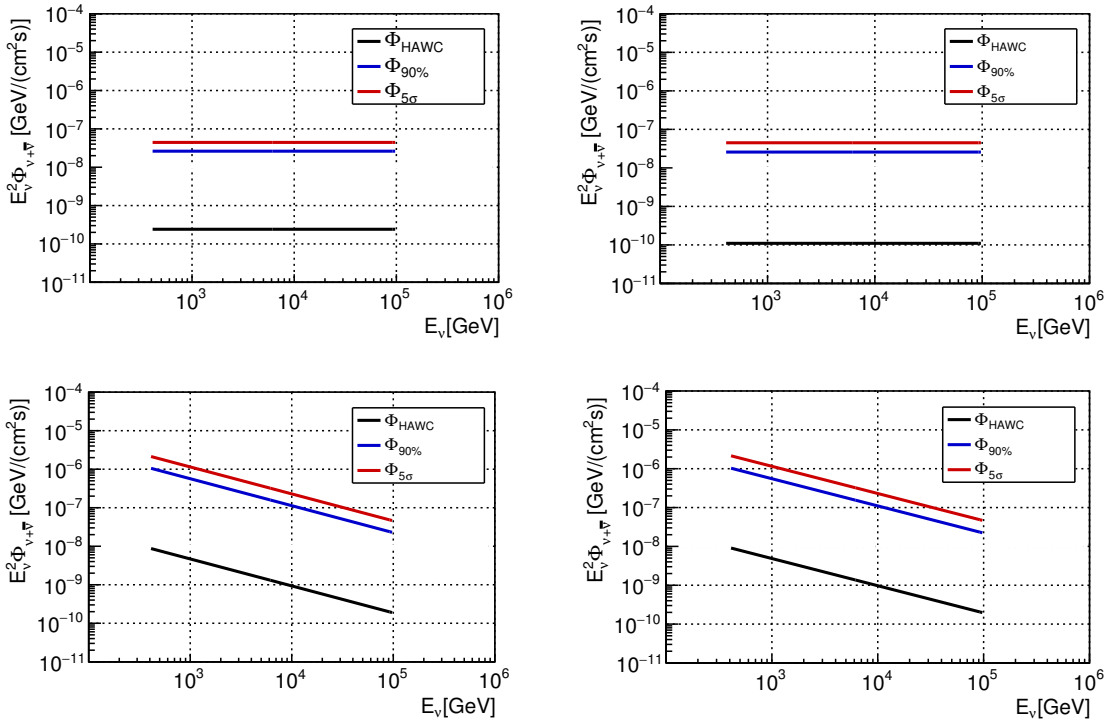

Figure 6.10: In the upper left (right) panels the sensitivity and 5σ discovery potential for the search of a neutrino emission from Mrk 421 (Mrk 501) are shown for a reference model of neutrino emission $d\Phi/dE_\nu = \Phi_0(E_\nu/7\text{TeV})^{-2}$. In the lower left (right) panels the sensitivity and 5σ discovery potential for the search of a neutrino emission from Mrk 421 (Mrk 501) are shown for a reference model of neutrino emission $d\Phi/dE_\nu = \Phi_0(E_\nu/1\text{TeV})^{-2.7}$. The neutrino fluxes predicted by the reference models are also displayed.

6.3.2 All-sky neutrino point source search

In the all-sky search the method used to search for point-like neutrino sources discussed in sec 6.2 is extended all over the sky. The HAWC γ-ray sky map with the power law energy spectra $d\Phi/dE_\nu = \Phi_0(E_\nu/7\text{TeV})^{-2}$ and a cut on the test statistic distribution of about 3σ, as discussed in 5.3.1, is assumed as model of neutrino production. The map has been used as template map to extract a list of 192 candidate point sources. In the all-sky search the quality cuts on the parameters of reconstructed tracks $\cos\theta > -0.1$, $\beta < 1^\circ$, $log_{10}(\rho) > 1.6$ and $L_\mu > 380$ m, already used in the point-like source searches, are considered. To improve the sensitivity and discovery potential of the all-sky point source search an optimisation of the track quality parameter Λ has been performed, varying the Λ cut in the range [-5.5, -5.0].

The search for a neutrino emission from the list of candidate neutrino sources is here investigated following the maximum-likelihood method. At first, as described in 6.2.2, the ingredients used to build the likelihood functions are generated as a function of the cut on Λ. Then, the significance of neutrino events is estimated through the hypothesis

test. In Fig. 6.11 the PSFs and the acceptances for a power law energy spectra E^{-2} are shown for the different Λ_{cut}.

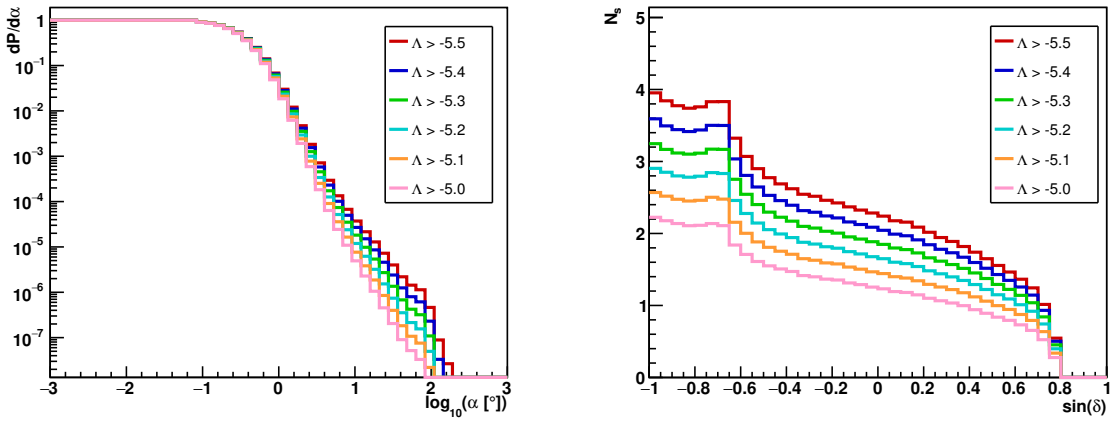

Figure 6.11: The PSFs and the acceptances for a power law energy spectra E^{-2} as a function of the cut on the track quality parameter Λ. The quality cuts on the parameters of the reconstructed tracks $\cos\theta > -0.1$, $\beta < 1^{\circ}$, $log_{10}(\rho) > 1.6$ and $L_{\mu} > 380$ m are also considered.

In Fig 6.12 the sensitivity at the 90%C.L. and the 5σ discovery potential of the searches are shown. As can be seen, different cuts on Λ optimise the 5σ discovery potential and the sensitivity of the search. In particular, the 5σ discovery potential is optimised for Λ>-5.3, while the sensitivity for Λ>-5.4. The distributions of the true MC energy of atmospheric and signal neutrino events corresponding to the Λ_{cut} which optimise the sensitivity are shown in the right panel of Fig. 6.13. The angular resolution for the same events is presented in the right panel. As can be seen, for the final set of quality cuts most of the reconstructed signal neutrino events have a $E_{\nu}\sim$15 TeV and an angular resolution of about 0.55 degrees.

A comparison between the sensitivity and discovery potential of the full-sky point source search with the neutrino fluxes predicted by the assumed model of neutrino production of the most intense sources of the list is presented in Fig. 6.14. The search for an all-sky neutrino emission from the extracted point-like sources sets an average upper limits which is a factor $\sim$ 7 higher than the brightest neutrino source of the list. In order to improve the sensitivity of the full-sky search a stacking analysis of the listed sources can be performed. The stacking analysis combines regions of potential neutrino sources in such a way that the neutrino signals add constructively to increase the cumulative significance of these sources. In order to test the hypothesis of an astrophysical origin of the observed neutrinos, the stacking analysis follows a maximum likelihood approach. In this method an extended likelihood is built to distinguish between a signal+background hypothesis, H_1, from the null hypothesis, H_0, where only background is considered. In the stacking approach a global fit of the signal *pdf* is performed. The signal *pdf* contains the sum of the sources contributions and the relative contribution of each source is fixed

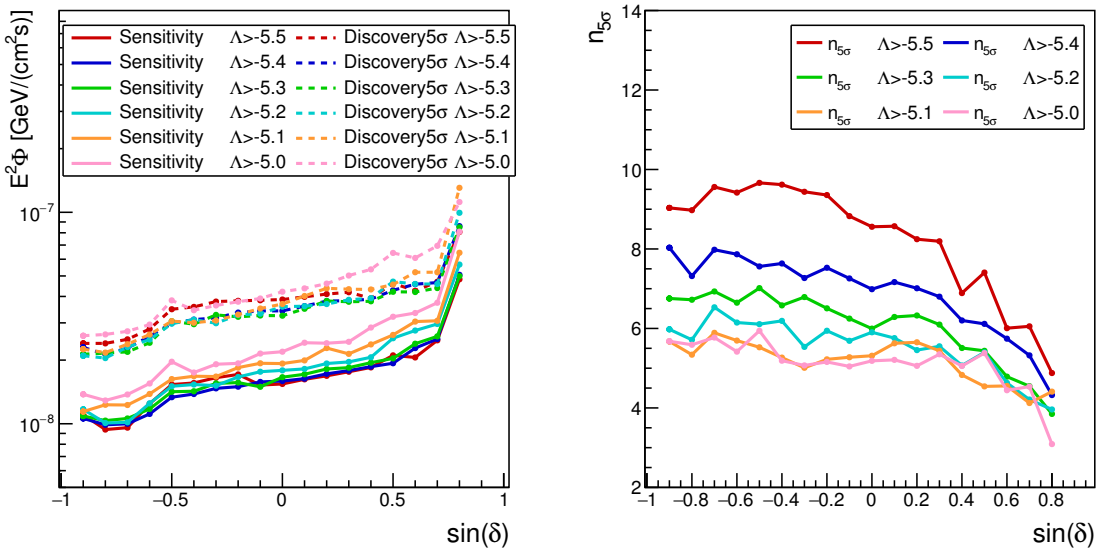

Figure 6.12: In the left panel the ANTARES sensitivity at the 90% C.L. and the 5σ discovery potential as a function of the $sin\delta$ are shown for the considered cuts on the track quality parameter Λ. The Λ cuts which optimise the 5σ discovery potential and the sensitivity of the search are Λ>-5.3 and Λ>-5.4 respectively. In the right panel the number of neutrino events necessary for a 5σ discovery in the 50% of the pseudo-experiments is reported as a function of the $sin\delta$ for the different cuts on Λ.

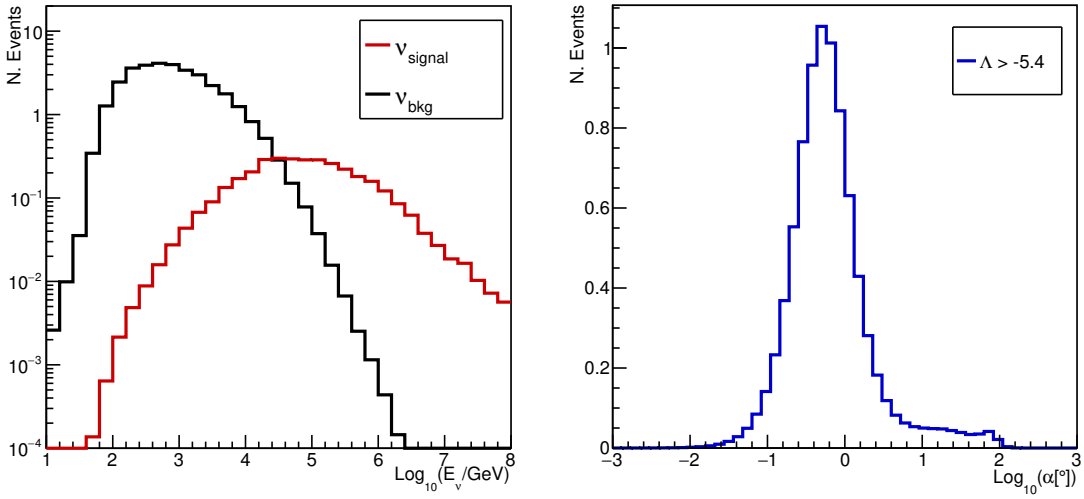

Figure 6.13: In the left panel the distributions of the true MC energy E_ν of atmospheric (black) and signal (red) neutrino events for Λ_{cut} −5.4, cosθ > − 0.1, $\beta < 1°$, $log_{10}(\rho) > 1.6$ and $L_\mu > 380$ m are presented. In the right panel the angular resolution for the same set of quality cuts is reported.

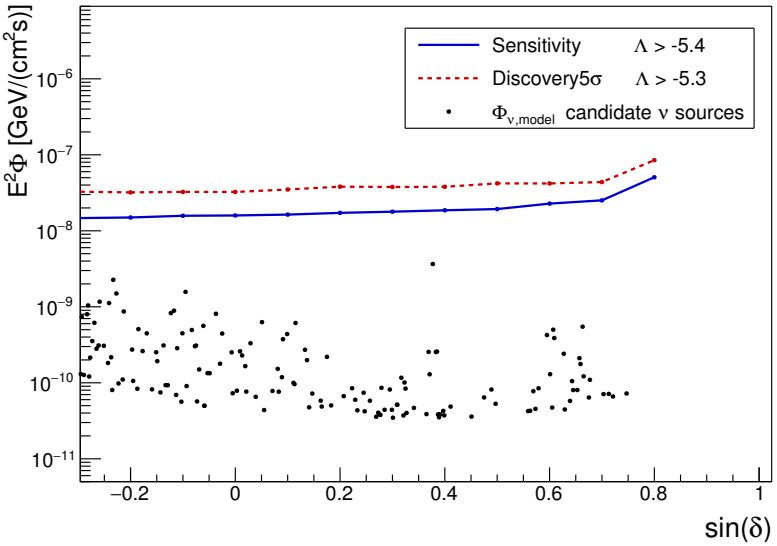

Figure 6.14: Sensitivity at the 90%C.L. and 5σ discovery potential of the full-sky point-like neutrino sources search compared with the neutrino fluxes predicted by the assumed model of neutrino emission. The full-sky search of point-like neutrino sources sets un average upper limit which is a factor ~ 7 higher than the brightest neutrino source of the list located at a $\sin\delta = 0.37$.

by a weight w.
Since the stacking analysis seems to be a promising strategy to improve the sensitivity of the full-sky point source search, the possibility to perform this analysis will be investigated in a future extension of this work. A further improvement of the ANTARES sensitivities can be also obtained including the contribution of the shower-like events detected by the ANTARES telescope over the considered period of data taking.

Chapter 7

The KM3NeT/ARCA data qualification and first results

As already described in Chapter 3, the KM3NeT research infrastructure will host a multi cubic kilometre scale neutrino telescope, composed by the ARCA and the ORCA detectors. The implementation of the ARCA detector has already started with the deployment of the first two detection units at the Capo Passero site in December 2015 and May 2016. Part of the work presented in this thesis has been dedicated to the qualification of the KM3NeT/ARCA data. In this chapter the approach adopted to identify a strategy for the monitoring of the quality of ARCA raw data is described.
In order to proceed with the qualification of the KM3NeT/ARCA data, a monitoring software aimed to verify both the data integrity and quality has been developed, the *GRunAnalyser*. Performing a detailed analysis of the physics runs and questioning about the data integrity, the software highlighted the presence of several issues in both the ARCA-DU1 and ARCA-DU2 data and allowed to identify the reasons behind the observed anomalies. Investigating about the quality of the physics runs, GRunAnalyser turned out to be an efficient tools to select a list of *golden runs*. The analysis of selected runs provided the first measurement of the depth dependence of the coincidence rates induced by atmospheric muons with the two ARCA-DUs.

7.1 KM3NeT/ARCA data taking qualification

After the deployment of the first two KM3NeT/ARCA detection units a commissioning phase was carried on, aiming at testing and verifying the correct functioning of all the ARCA components and assuring the quality of the collected stream of data according to the operational requirements described in the [7] and [150]. During this period of time great deal of effort has been focused by the KM3NeT collaboration on the qualification of the ARCA data. In order to reach this goal, the *GRunAnalyser* software has been developed to performed a detailed analysis and monitoring of the data (see sec. 7.2). Performing a fast run-by-run analysis of the JDAQSummaryslice and JDAQEvent data, GRunAnalyser looks for the value of some observables, averaged over the whole run dura-

tion, which characterise the quality of the physics runs. With the purpose of identifying the best set of parameters which qualify the detector performance in a run, the following set of observables has been defined:

- Mean number of active DOMs per DU: considered as a quality indicator of the acquired data;
- Number of missing timeslices: which allows to discard empty runs;
- Number of consecutive missing timeslices in a time interval Δt longer than 2 sec (GAP of consecutive timeslices): which implies the loss of data taking in short period of time;
- Number of timeslices with Broken Frames (more than 1 frame per TS per DOM): indicating an anomalous data structure;
- Number of frames with no UDP packets and number of frames with no UDP trailer: in order to monitor the stream of data from the off-shore detector to the shore station;
- Rate of triggered event (muon and shower triggers).

As described in sec. 7.3, the analysis of raw data through GRunAnalyser pointed out the presence of several issues in the ARCA data, allowing experts to identify the reasons of the observed anomalies and act with prompt reactions.

7.2 KM3NeT data monitoring tool: GRunAnlyser

The GRunAnalyser is a software written using the Jpp Software [117]. Jpp is a collection of Java inspired C++ interfaces, classes, methods and applications, needed for reading the KM3NeT data format as provided by the DataFilter (see sec. 3.10). The extracted observables are stored in an output ROOT file consisting of two TTree, an *Header* and a *DetRate* TTree. The Header TTree collects all the observables plus further useful information about the analysed physics run. In the DetRate TTree the rate of the both DUs and of the whole detector for each timeslice (100ms) are recorded. In this way the DUs and detector L0 hit rates can be easily displayed, as shown in Fig. 7.1.
The observables extracted by GRunAnalyser are also used to monitor the detector performance over a long period of time. Some examples are shown below. In particular referring to the period of acquisition from the December 20, 2016 to the February 4, 2017, except for nanobeacon and test runs, the average number of active DOMs, the average rate of triggered events and the percentage of missing timeslices per run as a function of the time are shown in Fig. 7.2, Fig. 7.3 and in Fig. 7.4 respectively. As can be seen in Fig. 7.2, the ARCA-DU2 lost two DOMs during the monitored period, with a consecutive decrease of the average number of active DOMs. This allowed to identify three different periods of homogeneous ARCA-DU2 runs. As a consequence of the loss of two ARCA-DU2 DOMs the average rate of triggered events per run decreased (see

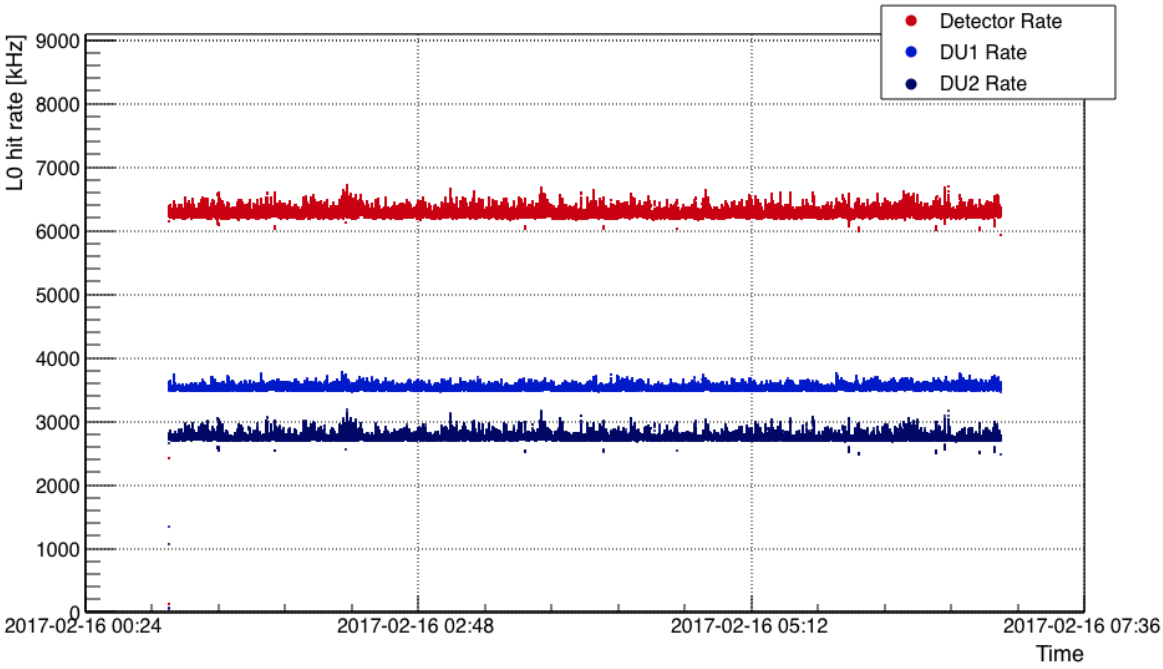

Figure 7.1: The plot shows the ARCA-DU1, the ARCA-DU2 and the full ARCA detector L0 hit rate during the physics run 5297. Due to the different numbers of active DOMs in each DU, ARCA-DU1 and ARCA-DU2 show different rates. Since the expected DOM rate is $\sim$ 200-220 kHz, the detector rate of $\sim$ 6200 kHz is compatible with the expected rate related to the number of active DOMs during the data acquisition. The bursts are due to the bioluminescence activities in the sea water. The points with rates $\sim$ 200 kHz lower than the expected DU rate are related to those timeslices that have lost a frame.

Fig. 7.3). Figure 7.4 shows the almost constant percentage of missing timeslice per run during the whole monitored period. A part for few runs, the low percentage of missing timeslice ($< 0.02\%$) highlights a stable data acquisition condition.

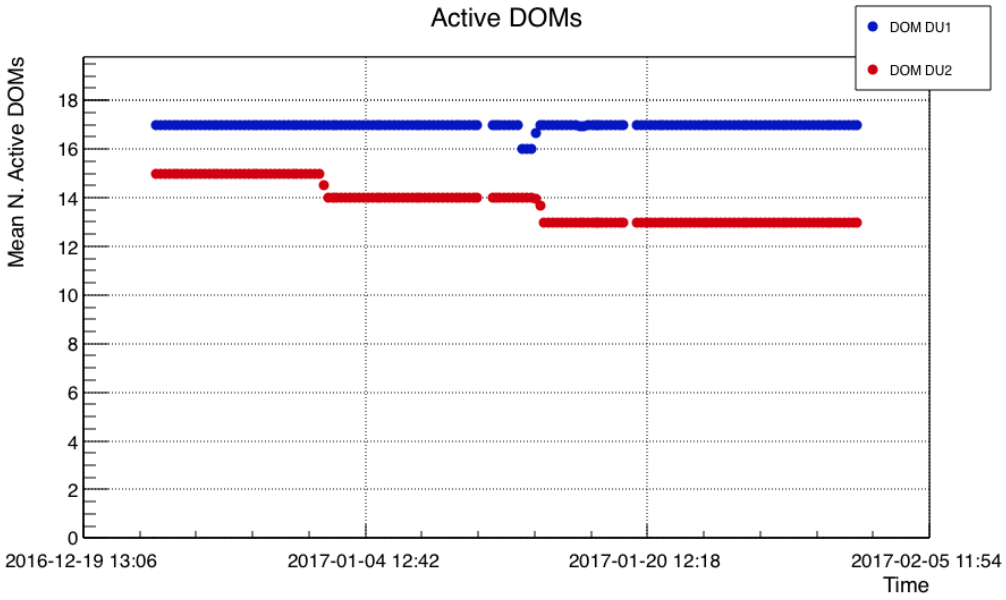

Figure 7.2: Average number of ARCA-DU1 and ARCA-DU2 active DOMs as a function of the time (physics runs 5009 – 5195). During the monitored period the ARCA-DU2 lost two DOMs, with a consecutive decrease of the average number of active DOMs.

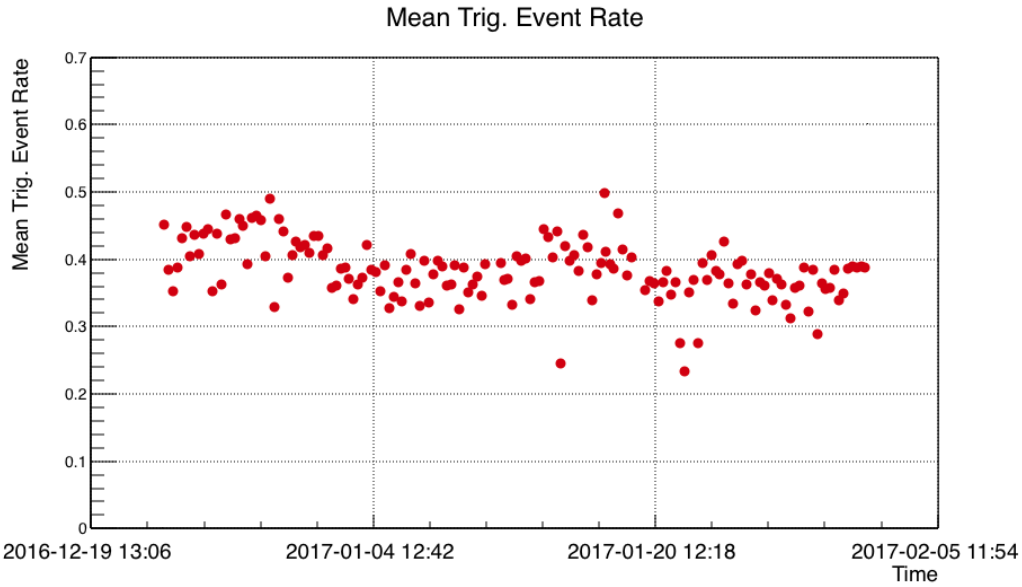

Figure 7.3: Average trigger event rate for the whole detector (ARCA-DU1 and ARCA-DU2) as a function of the time for the physics runs 5009 – 5195.

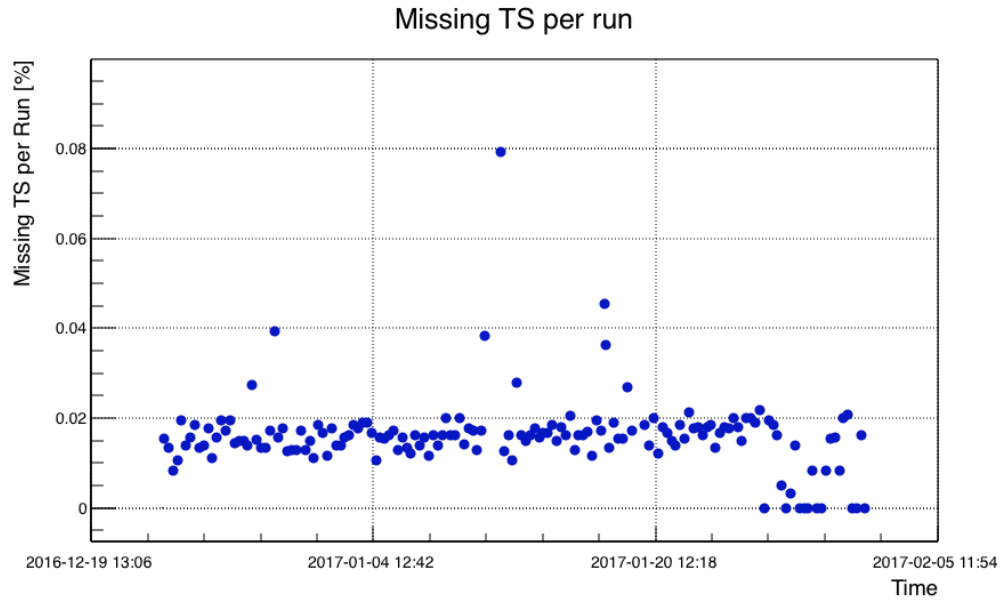

Figure 7.4: Percentage of missing timeslices for the whole detector (ARCA-DU1 and ARCA-DU2) as a function of the time (physics runs 5009 – 5195).

7.3 Results of the raw data analysis

In this section the anomalies discovered during the analysis of the ARCA-DU1 and ARCA-DU2 data, collected between June and September of 2016, are presented. This anomalies were found performing a run-by-run analysis of both L0 and L1 ARCA runs using the GRunAnlyser software.

7.3.1 Time synchronisation issue

In the ARCA data the rate of L0 hits is mainly due to the light emitted by the ^{40}K decay and bioluminescence activity in sea water, resulting in a rate of $\sim$ 6.5 - 7 kHz in each PMT [113] and in a global DOM rate per timeslice of about 210 - 220 kHz. During the analysis of ARCA-DU1 and ARCA-DU2 runs an unexpected enhanced DOM rate was observed in several timeslices distributed over the entire run duration, as reported in Fig. 7.5 for the ARCA run 3545. In the figure the rate of both ARCA-DUs, estimated by summing the rate of active DOMs over a whole DU, is shown as a function of the time. Beside the presence of bursts probably related to the bioluminescence activity in the deep sea water, an enhanced DOM rate of about 200 kHz respect to the expected valued was recorded in both ARCA-DUs.
In order to understand the reason of this anomalous rate, GRunAnalyser was used to perform a detailed investigation of data stored in the timeslices showing the enhanced DOM rate. An example of timeslice showing this issue is given by the timeslice number 670, corresponding to the timestamp 1465174887000 ns, in the ARCA run 3545. In this timeslice an anomalous DOM rate was detected by DU1-DOM17, as reported in Tab. 7.1. The rate of L0 hits detected by every PMT of the same DOM is reported in Tab. 7.2.
The rate measured by DU1-DOM17 suggested an anomalous number of L0 hits in the frame which collects the DU1-DOM17 data. An accurate examination of the L0 run structure led to discover the presence of a doubled sequence of L0 hits in the same frame, as shown in Fig. 7.6. This anomalous DOM rate was due to a not correct increase of the frame timestamp, causing the merging of consecutive frames in the same timeslice. As a consequence of this bug in the data structure, the affected DOM looses its time synchronisation and does not participate in successive muon event triggers. The cause of this bug was found in the random occurrance of the complete filling of a specific memory in the FPGA firmware, that happens when the last UDP packet sent by the CLB was completely full of hits. The release of a new CLB firmware version fixed this issue.

7.3.2 Missing timeslices at the beginning of a run

Since in physics runs the timeslices are not chronologically arranged, a fast way to identify periods of no data taking is to put the timeslices in chronological order and to look for the lack of consecutive timeslices not justified by the ordinary data taking condition. The search for such condition allowed to discover the lack of consecutive timeslices soon after the beginning of almost every run, as shown in Fig. 7.7. The cause of such issues is related with network instabilities and, even if this issues is present in almost every run

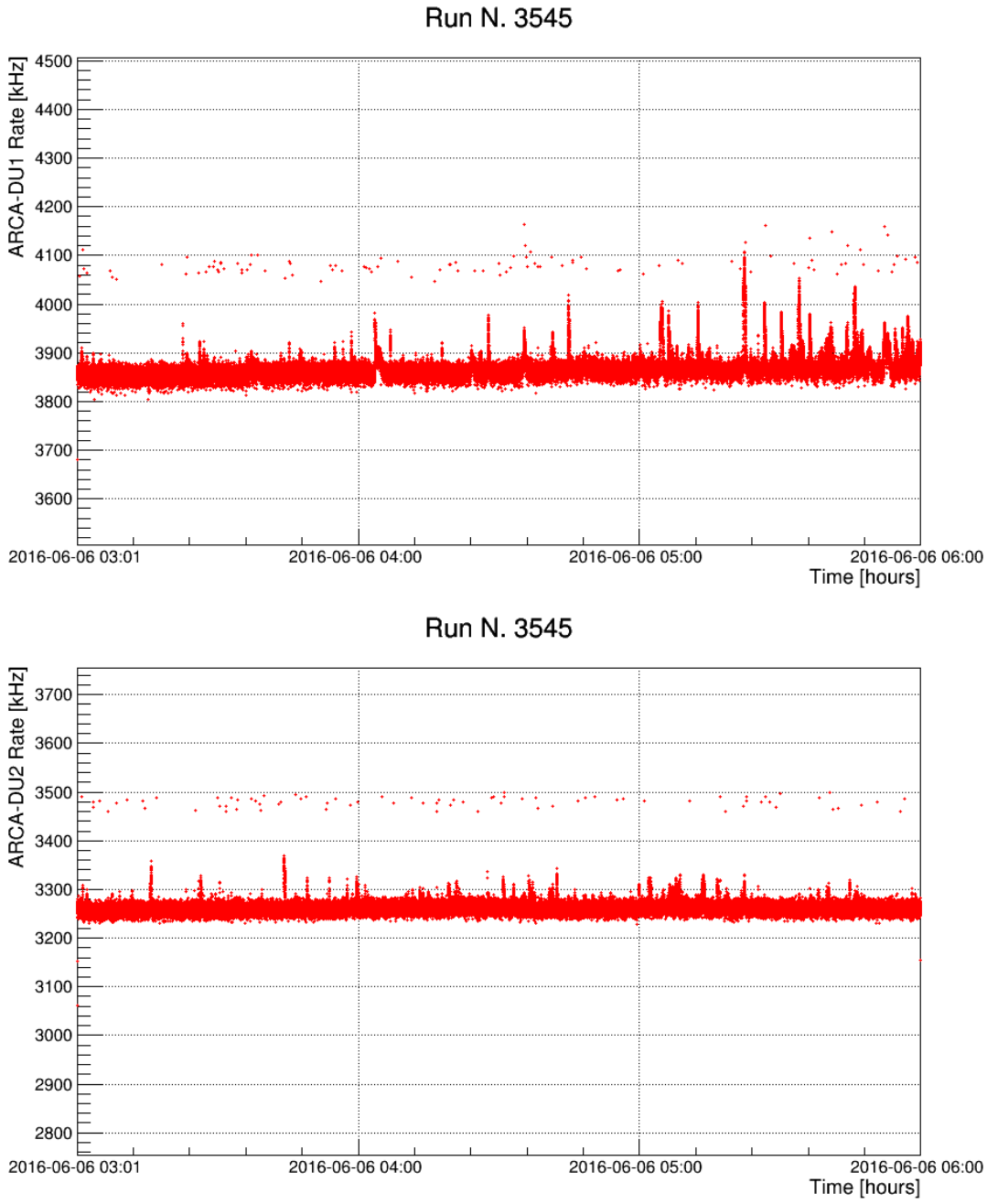

Figure 7.5: In figure the ARCA-DU1 and ARCA-DU2 rate of L0 hits detected during the run 3545 is shown. Beside the presence of bursts related to the bioluminescence activity in deep sea water, an enhanced DOM rate of about 200 kHz (red single point) respect to the expected DU rate (baseline) is present in several timeslices.

	DU1 DOM Rate [kHz]	DU2 DOM Rate [kHz]
DOM 1	206.90	213.12
DOM 2	204.90	216.00
DOM 3	207.48	215.94
DOM 4	220.99	207.92
DOM 5	213.62	223.84
DOM 6	208.98	217.71
DOM 7	215.20	212.83
DOM 8	217.94	210.42
DOM 9	206.37	217.84
DOM 10	212.52	218.11
DOM 11	214.58	0
DOM 12	211.21	0
DOM 13	220.96	219.38
DOM 14	212.54	220.28
DOM 15	223.38	226.13
DOM 16	218.04	220.38
DOM 17	**418.98**	221.97
DOM 18	223.24	0

Table 7.1: DOM rates of detected L0 hits for ARCA-DU1 and ARCA-DU2 in the timeslice number 670, corresponding to the timestamp 1465174887000 ns, of the ARCA run 3545. The rates of DU2-DOM11, DU2-DOM12 and DU2-DOM18 are not reported because they were not active during the data acquisition of the ARCA run 3545.

PMT n.	Rate [kHz]	PMT n.	Rate [kHz]
0	14.06	16	13.32
1	11.32	17	14.85
2	10.44	18	15.25
3	11.02	19	13.69
4	14.06	20	13.69
5	12.62	21	14.45
6	14.06	22	17.95
7	13.69	23	12.97
8	12.62	24	14.85
9	12.62	25	13.32
10	11.02	26	12.62
11	11.32	27	12.97
12	14.45	28	16.55
13	14.06	29	13.32
14	14.06	30	13.32
15	14.45		

Table 7.2: Rate of detected L0 hits for each PMT of ARCA-DU1 DOM 17 in the timeslice number 670, corresponding to the timestamp 1465174887000 ns, of the ARCA run 3545.

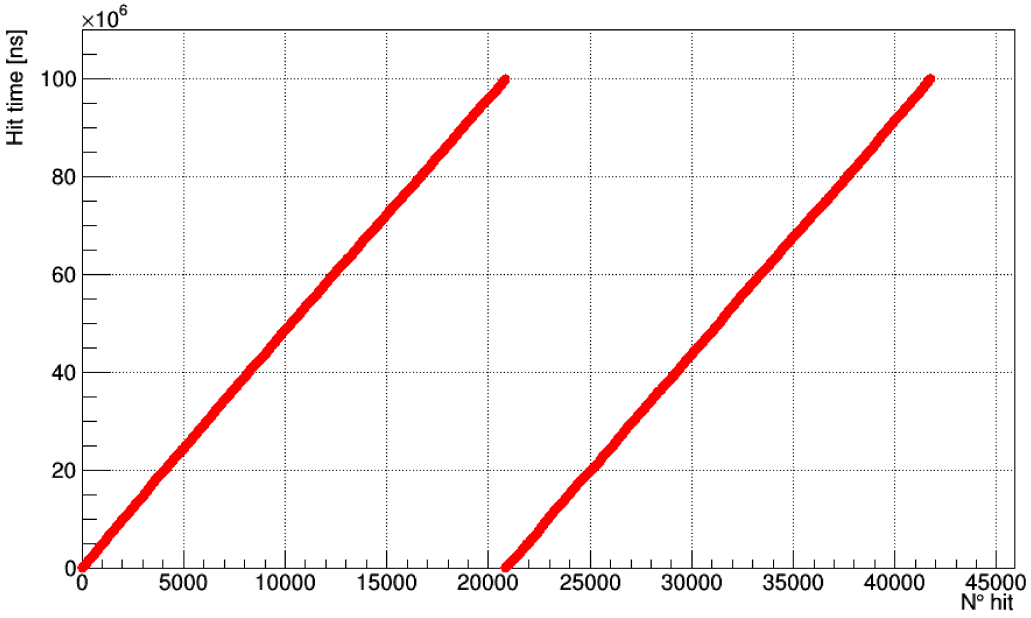

Figure 7.6: Doubled sequence of L0 hits found in the frame which collects the hits detected by DU1-DOM17, corresponding to the timestamp 1465174887000 ns of ARCA L0 run 3545. The hit identifier is reported on the x-axis while the timeslice duration (100 ms) is reported on the y-axis. By looking for the chronological order of detected hits an anomalous doubled sequence of hits was found.

and the percentage of missing timeslice is lower than 1‰, it does not affect the quality of data taking.

7.3.3 Reduced DOM rate per frame

During the analysis of ARCA-DU1 and ARCA-DU2 data the presence of timeslices with a reduced DOM rate was also reported, as shown in Fig. 7.8. In this case, a detailed investigation of the chronological order of detected hits over the frame duration allowed to discover the partially hit detection during the frame. The reason of this interruption of data acquisition is connected with network instabilities. Considering that it was a very rare issues, it did not affect the quality of the data taking.

7.3.4 Presence of timeslices with uncorrected timestamp

An other issues discovered in ARCA data was the presence of timeslices with uncorrected timestamp like 3615999443900 ns, which corresponds to the 13/12/2029 at 21:45:52. Only few runs having timeslices with uncorrected timestamp have been found during the monitoring of the entire period of ARCA-DU1 and ARCA-DU2 data taking, with a percentage of uncorrected timestamp per run of about 0.00046%.

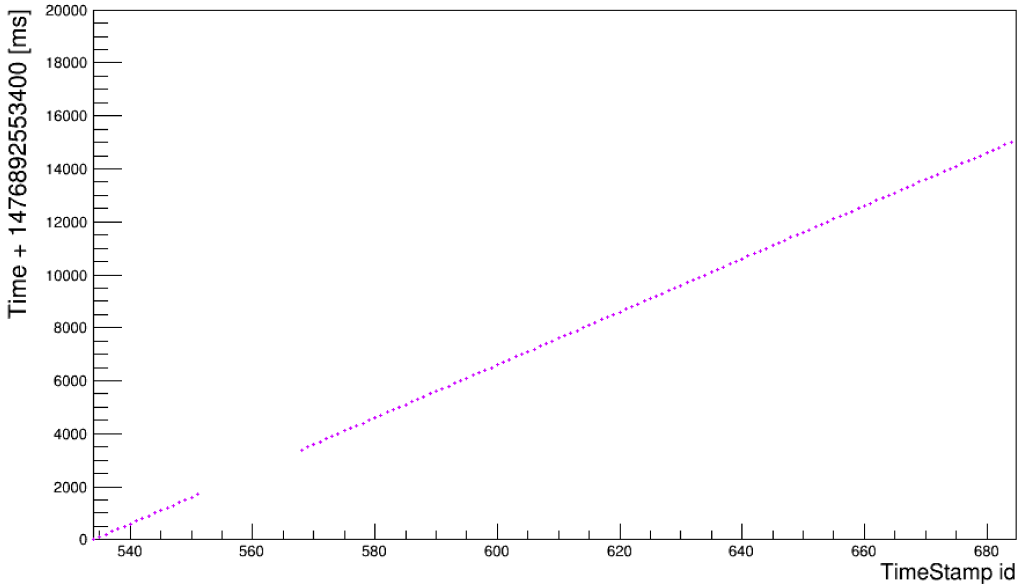

Figure 7.7: In the figure each point refers to a timeslice. The chronological order of the timeslices as a function of the simeslice identifier reveals the presence of the lack of consecutive timeslices at the beginning of the run. In this example the ARCA run 4142 has been considered.

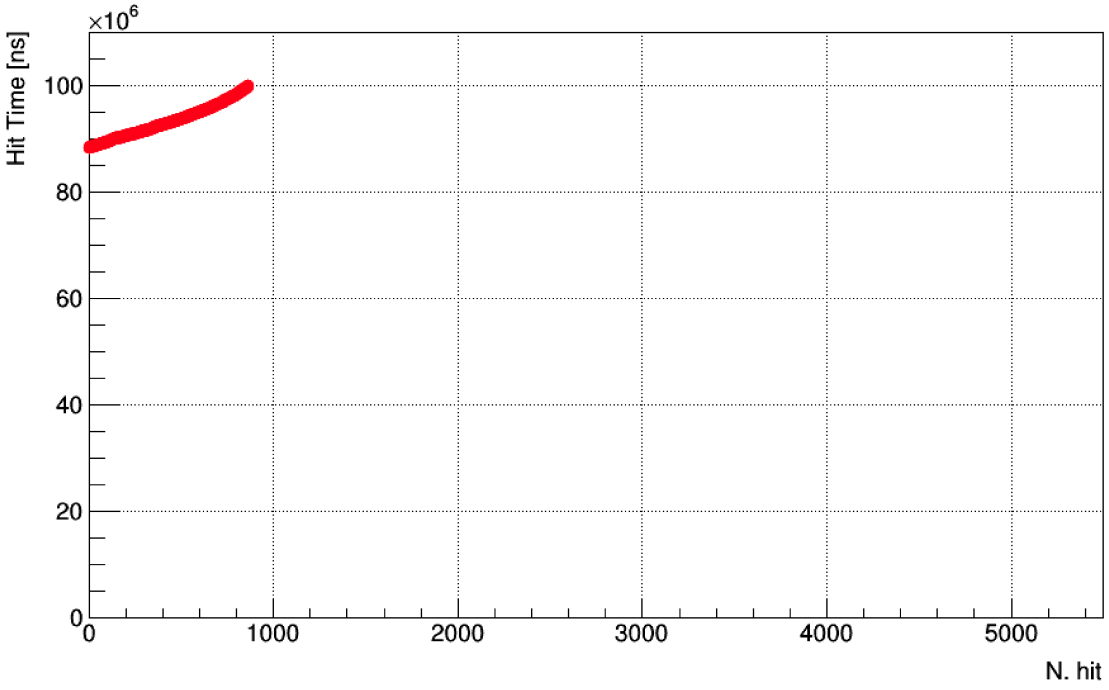

Figure 7.8: Example of frame with interruption of data acquisition due to network instabilities.

7.3.5 Equally spaced peaks in the distribution of the total number of detected L0 hits per frame

By looking for anomalies in L0 runs, the presence of equally spaced peaks in the distribution of the total number of detected L0 hits per frame was found, as shown in Fig. 7.9 for the ARCA L0 run 4145. In order to understand if these features can affect the data taking in a significant way, all the available L0 run were analysed. The presence of equally spaced peaks, separated by a number of hits $\Delta N_{hit} = 1489$, was found in all analysed runs, as reported in Tab. 7.3. Further investigations allowed to discover that the peaks are related to an uncorrected stream of data from the off-shore detector to the shore station, resulting in the loss of UDP packets each one consists of 1489 hits.

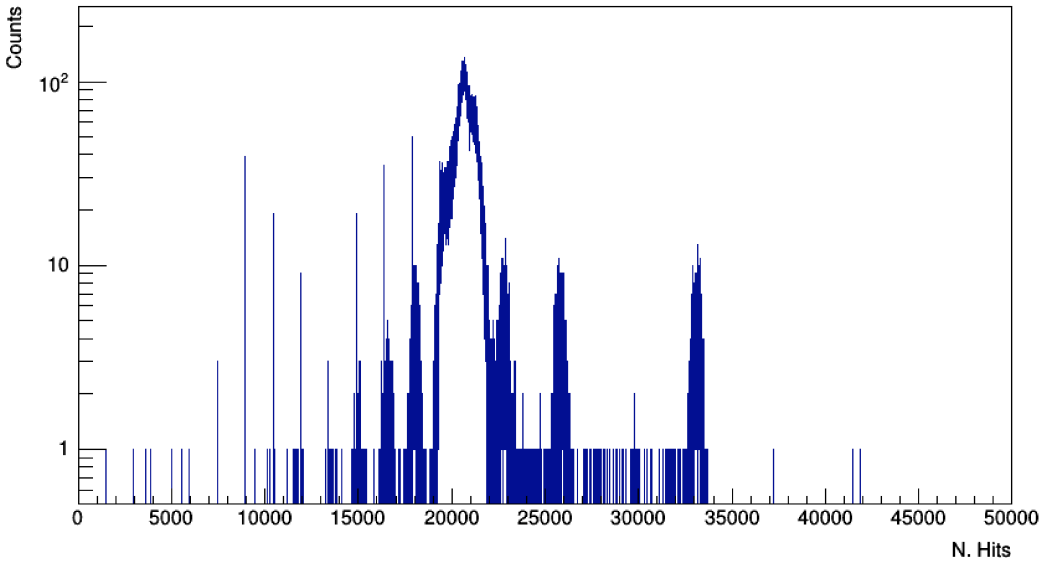

Figure 7.9: Distribution of the total number of detected L0 hits per frame of the ARCA L0 run 4145. In the distribution the equally spaced peaks are related to the loss of UDP packets each one consists of 1489 hits.

RUN 4145	RUN 4147	RUN 4149	RUN 4151
7445	-	-	-
8934	-	-	-
10423	-	-	-
11912	-	-	-
13401	-	-	13401
14890	14890	-	14890
16379	16379	16379	16379
17868	17868	17868	17868
19357	19357	-	-

Table 7.3: Positions of the peaks observed in the distributions of the total number of detected hits per frame for all the analysed L0 runs. The peaks appear always at the same position and separated by a constant number of hits equal to $\Delta N_{hit} = 1489$.

7.4 KM3NeT/ARCA run selection

GRunAnalyser was also used to select a list of “golden run" in order to have a dataset as much uniform as possible to reduce the data/MC differences and keep under control the systematics. The criteria used for the run selection are:

- Run duration longer than 10 min;
- Average rate of triggered events;
- Average number of active DOMs per DU > number of active DOMs per DU – 0.5, which excludes a run if a DOM stops sending data in the first half of run itself.

According to these criteria a total number of 258 golden runs was selected [151], corresponding to a 68.9 days of equivalent livetime.

7.5 First result with the ARCA selected runs

The multi-PMT DOM structure of the ARCA telescope allows for selecting atmospheric muons over the optical background looking for local coincidences between PMTs [113]. Exploiting this DOM feature, a measurement of the depth dependence of the coincidence rates induced by atmospheric muons has been performed using the first two ARCA-DUs [152]. In fact, even if the DU are positioned at a depth of approximately 3500 m and the sea water shields them from the cosmic ray air shower particles, a significant amount of downgoing atmospheric muons reaches the detector. Due to the considerable height of the strings the muon flux is expected to change along the string length.
The depth dependence analysis is based on local coincidences (L1), defined as the sample

of two or more hits detected by the PMTs of the same DOM within a time window of 25 ns. The PMT multiplicity (m) is defined as the number of PMTs in the same DOM with a L1 local coincidence. Most of the local coincidences are due to the optical background from the decay of ^{40}K, which is constant at all times and depth-independent.
In the analysis the background coincidence rates generated by ^{40}K decay has been simulated using OMGsim [153], a Geant4-based simulation of the DOM. Atmospheric muon events were generated with MUPAGE and the subsequent generation and propagation of light, as well as the detector response have been simulated using KM3 and JPP (see chapter 4).
For the depth dependence analysis L1 data taken from December 23 2016 to January 13 2017 have been used, with a total effective live time of 19.5 days. During this period of data acquisition the ARCA-DU1 DOM18 and ARCA-DU2 DOM2, DOM11 and DOM12 were not functional.
Data-MC comparison of the rates of local coincidences in a time window of 25 ns, for the lowest and the highest DOMs of the two ARCA-DUs, is shown in Fig. 7.10. It can be seen that low PMT multiplicities are related to optical background. On the other side, atmospheric muon events produce local coincidences on a great number of PMTs in the same DOM, with a consequent high PMT multiplicity. The data-MC comparison shows that for a multiplicity $m \geq 8$ the coincidences rate due to optical background from ^{40}K decay is negligible. Therefore, cuts on PMT multiplicity allows to select atmospheric muons over the optical background.

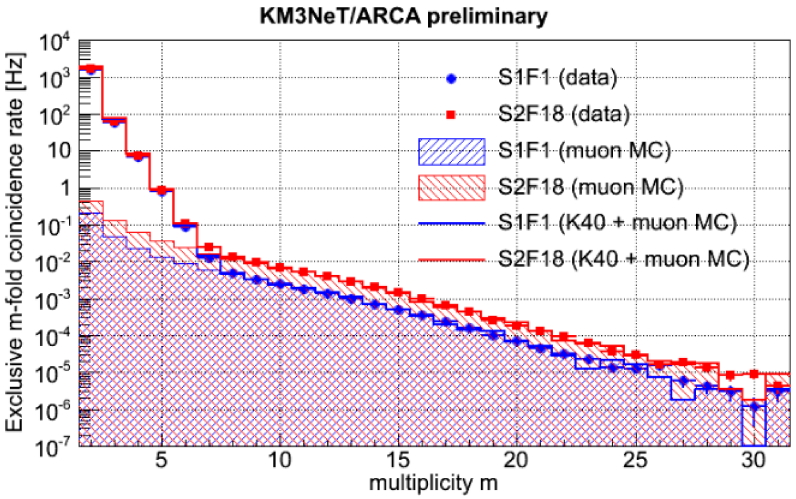

Figure 7.10: Rate of multiple coincidences for the DOM1 of ARCA-DU1 and DOM18 of ARCA-DU2 as a function of PMT multiplicity. Data are reported as blue circles and red squares. The MC simulations of the atmospheric muon background are represented by full areas. The sum of the atmospheric muons and optical background are indicated by full lines. For a multiplicity $m \geq 8$ the coincidences rate due to optical background is negligible [152].

Figure 7.11 shows the rate of $m \geq 8$-fold coincidences as a function of depth. The red dashed line is obtained with a MC simulation of a detector with identical PMTs. How-

ever, in order to correct the data for the different PMT responses, the PMT efficiencies determined using the ^{40}K in-situ calibration [154] were taken into account. A full atmospheric muon MC simulation incorporating these measured PMT efficiencies has been produced and compared to the MC with uniform PMT efficiencies. For each DOM the ratio of the rates observed in these two MC has been then used to correct the data for the MC-simulated effect of the measured PMT efficiencies. These corrected data points are shown in Fig. 7.11 together with the uncorrected data. A better agreement between corrected data and MC with identical PMTs efficiencies was found, showing that the in-situ calibration improves data/MC agreement.

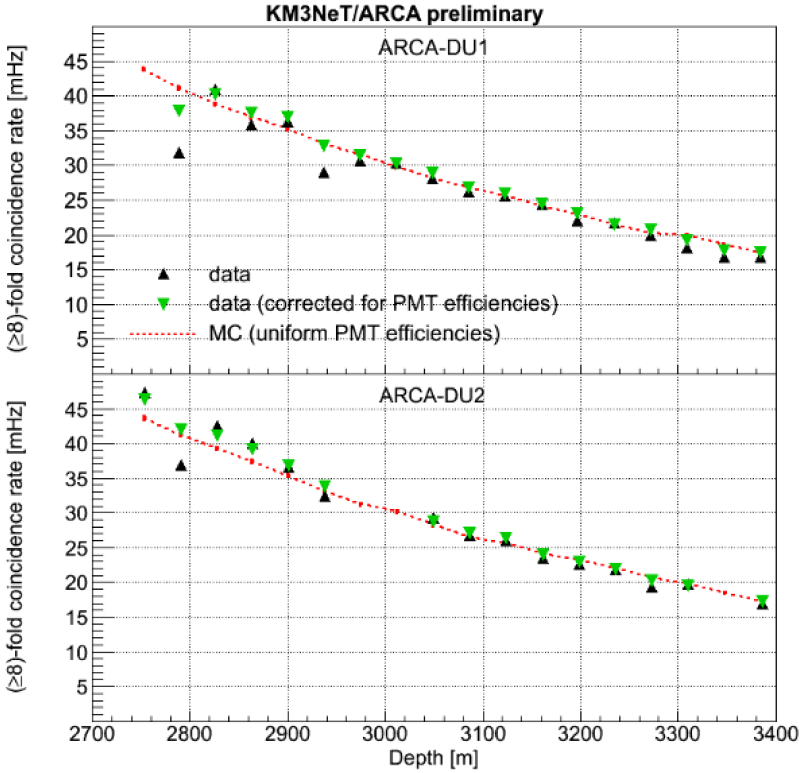

Figure 7.11: Comparison between data (black triangle), MC with uniform PMTs efficiencies (dotted line) and corrected data for relative PMTs efficiencies (green square) of the rates of $m \geq 8$ PMT coincidences in the DOMs as a function of depth for ARCA-DU1 and ARCA-DU2 [152]. DOM1 is the lowermostDOM of ARCA-DU1 (3390 m), DOM18 is the uppermost DOM of ARCA-DU2 (2750 m), see Fig. 7.10.

Conclusions

The ANTARES detector is the largest and more sensitive neutrino telescope in the norther hemisphere in operation since 2007, with the main scientific goal to discover astrophysical neutrino sources in the TeV-PeV energy range. In this thesis the first results of the search for a neutrino counterpart of the HAWC γ-ray sky using the data collected by the ANTARES telescope in the period of time 2007-2017 is presented. In particular the search for a neutrino emission from the point-like sources Markarian 421 and Markarian 501 and from the HAWC γ-ray sky has been performed. At GeV-TeV energies a γ-ray emission due to unresolved sources, resulting from the interaction of cosmic rays with matter and photons, is the dominant component of the γ-ray sky. In consequence of the cosmic ray interactions in our Galaxy, it is also expected that a significant component of the diffuse neutrino flux reaching the Earth has a galactic origin and can be directly related to the observed galactic γ-ray emission. The 2 years HAWC γ-ray source catalogue, recently published by the HAWC collaboration, represents the most sensitive survey of the TeV sky at the present day and it can be used to investigate the origin of the neutrino emission in our Galaxy. In order to search for a neutrino counterpart to the HAWC γ-ray sky, two γ-ray point source sky maps have been considered as reference models to determine a topological and spectral energy distributions of the neutrino flux all over the sky. The sky maps have been provided by the HAWC collaboration in compliance with the memorandum of understanding between the HAWC and the ANTARES collaborations. Even if only a fraction of the observed γ-ray emission can be considered of hadronic origin, in this work a one-to-one correspondence between the γ-ray and neutrino fluxes has been assumed to derive the neutrino counterpart to the HAWC γ-ray sky maps. Even though this assumption is not strictly corrected, it allows to obtain an optimistic limit setting on the corresponding neutrino flux. The sensitivity of the search for point-like neutrino sources has been estimated through MC simulations of $\nu_\mu(\bar{\nu}_\mu)$ and $\nu_e(\bar{\nu}_e)$ (CC and NC interactions). The MC sample has been differently weighted to reproduce the background and signal events. The contribution due to atmospheric muons has been taken into account through the simulation of the extensive air showers produced by the interactions of high energy cosmic rays with the particles present in the Earth's atmosphere. In order to optimise the sensitivity and discovery potential of the search a data/MC comparison has been performed. The background from atmospheric muons has been rejected by selecting upward-going neutrino-induced tracks and applying cuts on the quality parameters of the track reconstruction algorithm, while the estimator of

the reconstructed energy has been used to reject atmospheric neutrinos. The search for a neutrino emission from the point-like sources has been performed using a maximum likelihood method. The search for a neutrino emission from Markarian 421 and Markarian 501 sets a sensitivity two orders of magnitude higher than the predicted neutrino fluxes. The search for an all-sky neutrino emission from the HAWC point source sky map sets an average upper limit which is a factor ~ 7 higher than the brightest source of the list. A less sensitive result of about 20 % has been found respect to previous ANTARES point-like source search. Since the discrepancy between the average upper limits is mainly due to the different MC productions considered in the two analyses, the differences between the MC productions are under investigations. The possibility to improve the sensitivity of the full-sky search through a stacking analysis of the point-like sources of the HAWC γ-ray sky will be investigated in a future extension of this work. A better limit setting on the ANTARES sensitivities can be reached including also the contribution of shower-like events. Finally, a much more realistic neutrino production model will be also taken into account.

To extend the ANTARES performances the KM3NeT collaboration started to build a research infrastructure in the Mediterranean Sea which will host a multi cubic kilometre scale neutrino telescope, the ARCA detector. In this thesis the software developed for the qualification and monitoring of the KM3NeT/ARCA data is presented. The analysis of the ARCA data provided the first measurement of the depth dependence of the coincidence rates induced by atmospheric muons with the two ARCA-DUs, proving the high-performance of the ARCA detector.

Bibliography

[1] M. G. Aartsen et al., Physical Review Letters **113**, 101101 (2014).

[2] M. G. Aartsen et al., Astrophysical Journal **809**, 98 (2015).

[3] The IceCube Observatory, http://icecube.wisc.edu.

[4] The IceCube Collaboration et al., Science **361**, 146 (2018).

[5] The IceCube Collaboration, Science **361**, 147 (2018).

[6] The ANTARES Neutrino telescope, http://antares.in2p3.fr/.

[7] S. Adrián-Martínez et al., Journal of Physics G Nuclear Physics **43**, 084001 (2016).

[8] The HAWC Observatory, https://www.hawc-observatory.org/.

[9] E. Fermi, Physical Review **75**, 1169 (1949).

[10] A. R. Bell, Monthly Notices of the Royal Astronomical Society **182**, 147 (1978).

[11] S. P. Swordy, Space Science Reviews **99**, 85 (2001).

[12] T. Stanev, *High Energy Cosmic Ray*, 2^{nd} ed. (Springer, Chichester, 2004).

[13] P. Abreu et al., The Astrophysical Journal **762**, L13 (2012).

[14] F. Toshihiro et al., Physics Procedia **61**, 418 (2015).

[15] M. Takeda, et al., Physical Review Letters **81**, 1163 (1998).

[16] The Pierre Auger Observatory, https://www.auger.org.

[17] M. S. Longair, *High Energy Astrophysics*, 3^{rd} ed. (Cambridge University Press, Cambridge, 2011).

[18] A. M. Hillas, Ann. Rev. Astron. Astrophys **22**, 425 (1984).

[19] A. A. Abdo et al., Astrophysical Journal **716**, 30 (2010).

[20] F. Aharonian et al., Astronomy and Astrophysics **455**, 461 (2006).

[21] M. Ackermann et al., Science **339**, 807 (2013).

[22] A. López-Oramas, Ph.D. thesis, Barcelona, Autonoma U., 2014.

[23] M. Ajello et al., Astrophysical Journal Supplement **232**, 18 (2017).

[24] A. J. Smith, International Cosmic Ray Conference **10**, 227 (2005).

[25] The ARGO-YBJ Collaboration, arXiv:1311.3376 [astro-ph.HE] (2013).

[26] M. Mostafa for the HAWC Collaboration, arXiv:1310.7237 [astro-ph.HE] (2013).

[27] L. Zhao, S.B. Liu and Q. An, Chinese Physics C **38**, 016101 (2014).

[28] The HESS Observatory, http://www.mpi-hd.mpg.de/hfm/HESS/.

[29] The MAGIC Observatory, https://magic.mpp.mpg.de.

[30] The VERITAS Observatory, http://veritas.sao.arizona.edu.

[31] S. M. Bilenky, European Physical Journal H **38**, 345 (2013).

[32] V. Castellani et al., Physics Reports **281**, 309 (1997).

[33] J. K. Becker, Physics Reports **458**, 173 (2008).

[34] M. Plum, JPS Conf. Proc. **19**, 011011 (2018).

[35] A. Trovato and KM3NeT Collaboration, Journal of Physics: Conference Series **888**, 012108 (2017).

[36] H. Li, Y. Chen, and L. Zhang, Monthly Notices of the Royal Astronomical Society Letters **408**, L80 (2010).

[37] M. G Aartsen and et al., Astrophysical Journal **779**, 132 (2013).

[38] S. Adrían-Martínez et al., the Antares Collaboration, Astrophys. J. 760 (2012), 53., 1988.

[39] Karl Mannheim, Astroparticle Physics **3**, 295 (1995).

[40] F. Halzen and E. Zas, Astrophysical Journal **488**, 669 (1997).

[41] E. Waxman and J. Bahcall, Physical Review Letters **59**, 023002 (1999).

[42] A. Achterberg et al., Physical Review D **76**, 042008 (2007).

[43] Z. Shang et al., Astrophysical Journal **619**, 41 (2005).

[44] S. Bianchi, R. Maiolino, and G. Risaliti, Advances in Astronomy **2012**, 782030 (2012).

[45] T. Piran, Physics Reports **314**, 575 (1999).

[46] R. Abbasi et al., Nature **484**, 351 (2012).

[47] M. A. Markov and I. M. Zheleznykh, Nuclear Physics **27**, 385 (1961).

[48] F. Bernard, Ph.D. thesis, University of Marseille, 2000.

[49] IceCube Collaboration, Science **342**, 1 (2013).

[50] J. A. Formaggio and G. P. Zeller, Reviews of Modern Physics **84**, 1307 (2012).

[51] R. Gandhi, C. Quigg, M. H. Reno, and I. Sarcevic, Physical Review D **58**, 093009 (1998).

[52] C. Carlogeanu, *Muon interactions at high energies*, *ANTARES-Physics*/1998-003 (1998).

[53] M. Ackermann et al., Journal of Geophysical Research: Atmospheres **111**, (2006).

[54] C. D. Mobley, *Light and Water: radiative transfer in natural waters* (Academic Press, San Diego, 1994).

[55] S. Aiello et al., Astroparticle Physics **66**, 1 (2015).

[56] E. V. Bugaev, A. Misaki, V. A. Naumov, T. S. Sinegovskaya, S. I. Sinegovsky, and N. Takahashi, Physical Review D **58**, 054001 (1998).

[57] A. Okada, Astroparticle Physics **2**, 393 (1994).

[58] Vivek Agrawal, T. K. Gaisser, Paolo Lipari, and Todor Stanev, Physical Review D **53**, 1314 (1996).

[59] A. Okada, Astroparticle Physics **2**, 393 (1994).

[60] R. Enberg, M. H. Reno, and I. Sarcevic, Physical Review **78**, 043005 (2008).

[61] C.G.S Costa, Astroparticle Physics **16**, 193 (2001).

[62] M. Honda et al., Physical Review D **75**, 043006 (2007).

[63] M. G. Aartsen et al., Physical Review **D89**, 062007 (2014).

[64] S. Martini et al, Deep Sea Research Part I: Oceanographic Research Papers **116**, 33 (2016).

[65] The NEMO Experiment, http://nemoweb.lns.infn.it/sites/SiteReport/NEMOSiteReport.pdf.

[66] The BAIKAL Observatory, http://www.inr.ru/eng/ebgnt.html.

[67] A.V. Avrorin et al., Instruments and Experimental Techniques **56**, 449 (2013).

[68] A. Achterberg et al., Astroparticle Physics **26**, 155 (2006).

[69] The AMANDA Observatory, http://www.news.wisc.edu/misc/amanda.html.

[70] The IceCube Observatory, https://icecube.wisc.edu/science/stats.

[71] M. G. Aartsen et al., Astrophysical Journal **833**, 3 (2016).

[72] A. Palladino, M. Spurio, and F. Vissani, Journal of Cosmology and Astroparticle Physics **12**, 045 (2016).

[73] Y. T. Tanaka, S. Buson, and D. Kocevski, The Astronomer's Telegram **10791**, (2017).

[74] W. B. Atwood et al., Astrophysical Journal **697**, 1071 (2009).

[75] J. Aleksić et al., Astroparticle Physics **35**, 435 (2012).

[76] R. Mirzoyan, The Astronomer's Telegram **10817**, (2017).

[77] The IceCube Collaboration et al., Science **361**, (2018).

[78] IceCube-Gen2 Collaboration et al., ArXiv e-prints 1412.5106 (2014).

[79] The IceCube-PINGU Collaboration, arXiv:1401.2046 [physics.ins-det] (2014).

[80] S. Adrián-Martínez et al., Journal of Instrumentation **7**, T08002 (2012).

[81] J. A. Aguilar et al., Nuclear Instruments and Methods in Physics Research A **570**, 107 (2007).

[82] A. Albert and the ANTARES Collaboration, Astrophysical Journal **853**, L7 (2018).

[83] G. C. Hill and K. Rawlins, Astroparticle Physics **19**, 393 (2003).

[84] G. J. Feldman and R. D. Cousins, Physical Review D **57**, 3873 (1998).

[85] A. Albert et al. and ANTARES Collaboration, Physical Review D **96**, 062001 (2017).

[86] D. Gaggero et al., Physical Review Letters **119**, 031101 (2017).

[87] W.D. Apel et al, Astroparticle Physics **47**, 54 (2013).

[88] O. Adriani et al., Science **332**, 69 (2011).

[89] M. Aguilar et al., Physical Review Letters **114**, 171103 (2015).

[90] M. Ackermann et al., Astrophysical Journal **750**, 3 (2012).

[91] F. A. Aharonian et al., Nature **439**, 695 (2006).

[92] A. A. Abdo et al., Astrophysical Journal **688**, 1078 (2008).

[93] S. AdriÃąn-MartÃŋnez et al., Physics Letters B **760**, 143 (2016).

[94] A. C. Vincent, S. Palomares-Ruiz, and O. Mena, Physical Review D **94**, 023009 (2016).

[95] A. Albert et al., Physical Review D **96**, 082001 (2017).

[96] M. G. Aartsen et al., Astrophysical Journal **824**, L28 (2016).

[97] S. Adrián-Martínez et al., Physical Review D **93**, 122010 (2016).

[98] B. P. Abbott et al., Physical Review Letters **118**, 221101 (2017).

[99] A. Albert et al., The European Physical Journal **C77**, 911 (2017).

[100] A. Albert et al., Astrophysical Journal **850**, L35 (2017).

[101] B. P. Abbott et al., Astrophysical Journal **848**, L13 (2017).

[102] A. Goldstein et al., Astrophysical Journal **848**, L14 (2017).

[103] V. Savchenko et al., The Astrophysical Journal Letters **848**, L15 (2017).

[104] A. Albert et al., Journal of Cosmology and Astroparticle Physics **4**, 019 (2017).

[105] IceCube Collaboration. 2017, GCN circular 21916.

[106] S. Adrián-Martínez et al., Journal of Cosmology and Astroparticle Physics **2016**, 062 (2016).

[107] S. Adrián-Martínez, et al., Physical Review D **93**, 122010 (2016).

[108] S. Adrián-Martínez, et al., Journal of Cosmology and Astroparticle Physics **014**, (2015).

[109] A. Margiotta, Geoscientific Instrumentation, Methods and Data Systems **2**, 35 (2013).

[110] A. Margiotta, Journal of Instrumentation **9**, C04020 (2014).

[111] G. Riccobene and et al., Astroparticle Physics **27**, 1 (2007).

[112] S. Adrián-Martínez et al., European Physical Journal C **74**, 3056 (2014).

[113] S. Adrián-Martínez and et al., European Physical Journal C **76**, 54 (2016).

[114] S. Viola et al., PoS **ICRC2015**, 1169 (2016).

[115] C. Pellegrino and T. Chiarusi, European Physical Journal Web of Conferences **116**, 05005 (2016).

[116] https://www.ohwr.org/projects/white-rabbit.

[117] JPP Documentation, https://www.nikhef.nl/ mjg/Jpp/html/index.html.

[118] A. Hoecker et al., TMVA-Toolkit for Multivariate Data Analysis, ArXiv Physics e-prints **Pos ACAT**, 040 (2007).

[119] R. Coniglione et al. On Behalf Of The Km3Net, PoS **ICRC2017**, 998 (2018).

[120] D. Gaggero et al., The Astrophysical Journal Letters **815**, L25 (2015).

[121] A. Kappes et al., Astrophysical Journal **656**, 870 (2007).

[122] A. A. Abdo et al., Astrophysical Journal Letters **700**, L127 (2009).

[123] Tin Kam Ho, in *Proceedings of the Third International Conference on Document Analysis and Recognition (Volume 1) - Volume 1*, *ICDAR '95* (IEEE Computer Society, Washington, DC, USA, 1995), p. 278.

[124] S. R. Kelner et al., Physical Review D **74**, 034018 (2006).

[125] A. Trovato, R. Coniglione, P. Sapienza and J. Barrios-Martí, PoS **ICRC2017**, 999 (2018).

[126] M. G. Aartsen et al., The Astrophysical Journal **835**, 151 (2017).

[127] F. C. Brunner, $ANTARES\text{-}Software$/2000-008 (2000).

[128] D. Bailey, Ph.D. thesis, University of Oxford, 2002.

[129] G. Ingelman, A. Edin, and J. Rathsman, Computer Physics Communications **101**, 108 (1997).

[130] G. BARR, Ph.D. thesis, University of Oxford, 1987.

[131] P. Antonioli et al., Astroparticle Physics **7**, 357 (1997).

[132] V. Agrawal et al., Physical Review D **53**, 1314 (1996).

[133] Y. Becherini et al., Astroparticle Physics **25**, 1 (2006).

[134] A. Margiotta, $ANTARES$ *Internal note*, $ANTARES\text{-}Soft$/2004-002 (2004).

[135] "Geasim: User manual", http://antares.in2p3.fr/internal/software/geasim.html.

[136] https://wwwasd.web.cern.ch/wwwasd/geant/.

[137] M. de Jong, $ANTARES$ *Internal note*, $ANTARES\text{-}Soft$/2009-001 (2009).

[138] R. Bormuth, $KM3NeT$ *Internal Note*, $KM3NeT\text{-}SOFT$-201-001 (2015).

[139] S. Adrián-Martínez, et al., The European Physical Journal C **73**, 2606 (2013).

[140] Alberto Saa, Braz. J. Phys. **44**, pp.415 (2014).

[141] T. Michael, Ph.D. thesis, Amsterdam U., 2016.

[142] A. Albert et al., European Physical Journal C **77**, 419 (2017).

[143] A. U. Abeysekara et al., Astrophysical Journal **843**, 40 (2017).

[144] K. M. Górski et al., Astrophysical Journal **622**, 759 (2005).

[145] P. W Young et al. , PoS **ICRC2015**, 948 (2015).

[146] S.S. Wilks, The Annals of Mathematical Statistics **9**, 60 (1938).

[147] J. Neyman, Philosophical Transactions of the Royal Society **A236**, 333 (1937).

[148] R. Abbasi et al., Astrophysical Journal **732**, 18 (2011).

[149] M. Organokov and T. Pradier, 28th International Conference on Neutrino Physics and Astrophysics (Neutrino 2018) Heidelberg, Germany, June 4-9,2018. ARXIV:1809.05777 .

[150] P. Bagley et al., KM3NeT: Technical Design Report (2009).

[151] KM3NeT Internal doc, KM3NeT-OP-WD-2018-001-Arca003-Commented-Runlist.

[152] Martijn Jongen, PoS **ICRC2017**, 1018 (2018).

[153] M. Colomer et al., PoS **ICRC2017**, 983 (2018).

[154] K. Melis, PoS **ICRC2017**, 1059 (2018).